

**Density Matrix
Renormalisation Group Variants
for Spin Systems**

M.S.L. du Croo de Jongh

RIJKSUNIVERSITEIT LEIDEN



1 162 537 8

Density Matrix Renormalisation Group Variants for Spin Systems

Proefschrift

ter verkrijging van de graad van Doctor
aan de Universiteit Leiden,
op gezag van de Rector Magnificus Dr. W. A. Wagenaar,
hoogleraar in de faculteit der Sociale Wetenschappen,
volgens besluit van het College voor Promoties
te verdedigen op woensdag 1 september 1999
te klokke 16:15 uur

door

Maarten Steven Lucas du Croo de Jongh

geboren te Gorssel op 27 november 1970

Promotiecommissie:

| | |
|----------------|--------------------------------|
| Promotoren: | Prof. Dr. J. M. J. van Leeuwen |
| | Prof. dr. Ir. W. van Saarloos |
| Referent: | Prof. dr. H. W. J. Blöte |
| Overige leden: | Dr. P. J. H. Denteneer |
| | Prof. dr. D. Frenkel (AMOLF) |
| | Prof. dr. L. J. de Jongh |
| | Dr. J. Zaanen |

Het onderzoek beschreven in dit proefschrift is uitgevoerd als onderdeel van het wetenschappelijk programma van de Stichting voor Fundamenteel Onderzoek der materie (FOM) en de Nederlandse Organisatie voor Wetenschappelijk Onderzoek (NWO).

The research described in this thesis has been carried out as part of the scientific program of the Foundation for Fundamental Research on Matter (FOM) and the Netherlands Organization for Scientific Research (NWO).

Contents

| | |
|--|----|
| Introduction | 7 |
| 1. Luttinger model on a two-systems field | 11 |
| 1.1 Introduction | 11 |
| 1.2 The Model | 11 |
| 1.3 Connection with the Tomonaga-Luttinger model | 12 |
| 1.4 Fermi excitations for the LTF state | 13 |
| 1.4.1 The normal state | 16 |
| 1.4.2 The super state | 17 |
| 1.5 Fermi-like excitations | 18 |
| 1.5.1 1-dimensional, $W \rightarrow \infty$, $Z \rightarrow \infty$ | 19 |
| 1.5.2 2-dimensional, $W \rightarrow \infty$, $Z \rightarrow \infty$ | 21 |
| 1.5.3 3-dimensional, $Z, W \rightarrow \infty$ with fixed separation Z, W | 23 |
| 1.6 Conclusion | 24 |
| 2. Critical properties of the LTF through DMRG calculations | 25 |
| 2.1 Introduction to the Density Matrix Renormalization Group | 25 |
| 2.2 The Density Matrix | 26 |
| 2.3 Operators and application of the LTF | 30 |
| 2.4 Procedures | 32 |
| 2.5 Cases that work the Renormalization Group | 37 |
| 2.6 Performance | 37 |
| 2.6.1 General comments | 38 |
| 2.6.2 Comparison of both methods | 42 |
| 2.7 Some considerations on the implementation | 43 |
| 2.8 Results for the LTF | 44 |
| 3. Spin stiffness and finite-size scaling of the frustrated Heisenberg Model | 47 |
| 3.1 Introduction | 47 |
| 3.2 The frustrated Heisenberg Model | 48 |
| 3.3 The spin stiffness | 48 |
| 3.3.1 Direct derivation as an approximation | 49 |
| 3.3.2 Subspace-DMRG Method Approximation | 52 |
| 3.3.3 Spin stiffness in 2D MBL | 57 |
| 3.4 Isotropic Scaling | 61 |
| 3.5 Scaling for a highly anisotropic geometry | 65 |
| 3.6 Conclusions | 69 |

...gives 50% of a position will be given off

...gives 50% of a position will be given off

...gives 50% of a position will be given off

...gives 50% of a position will be given off

...gives 50% of a position will be given off

...gives 50% of a position will be given off

...gives 50% of a position will be given off

...gives 50% of a position will be given off

...gives 50% of a position will be given off

Contents

| | |
|--|-----------|
| Introduction | 7 |
| 1 Ising model in a Transverse field | 11 |
| 1.1 Introduction | 11 |
| 1.2 The Model | 11 |
| 1.3 Connection with the 3-dimensional Ising model | 13 |
| 1.4 Exact solutions for the ITF chain | 15 |
| 1.4.1 The periodic chain | 16 |
| 1.4.2 The open chain | 17 |
| 1.5 Finite-size scaling | 18 |
| 1.5.1 1-Dimensional, W fixed, $L \rightarrow \infty$ | 19 |
| 1.5.2 2-Dimensional, $W \rightarrow \infty$, $L = \infty$ | 22 |
| 1.5.3 2-Dimensional, $L, W \rightarrow \infty$ with fixed aspect ratio L/W | 23 |
| 1.6 Conclusion | 24 |
| 2 Critical properties of the ITF through DMRG calculations | 25 |
| 2.1 Introduction in the Density Matrix Renormalisation Group | 25 |
| 2.2 The Density Matrix | 26 |
| 2.3 Geometry and symmetries of the ITF | 30 |
| 2.4 Procedures | 32 |
| 2.5 Connection with the Renormalisation Group | 37 |
| 2.6 Performance | 37 |
| 2.6.1 General limitations | 38 |
| 2.6.2 Comparison of both methods | 42 |
| 2.7 Some considerations on the implementation | 43 |
| 2.8 Results for the ITF | 45 |
| 3 Spin stiffness and finite-size scaling of the frustrated Heisenberg Model | 47 |
| 3.1 Introduction | 47 |
| 3.2 The frustrated Heisenberg Model | 48 |
| 3.3 The spin stiffness | 48 |
| 3.3.1 Direct derivation at zero temperature | 49 |
| 3.4 Schwinger-Boson Mean Field Approximation | 52 |
| 3.5 Spin stiffness in SBMF | 57 |
| 3.6 Isotropic Scaling | 61 |
| 3.7 Scaling for a highly anisotropic geometry | 65 |
| 3.8 Conclusions | 69 |

| | |
|--|------------|
| 4 Density Matrix Renormalisation Group approach to the stiffness | 71 |
| 4.1 Expressions for ρ_s | 71 |
| 4.2 Calculating wave functions | 73 |
| 4.3 Geometry | 74 |
| 4.4 Scaling | 75 |
| 4.5 Results | 76 |
| 4.5.1 Scaling to $L = \infty$ | 77 |
| 4.5.2 Scaling to $W = \infty$ | 77 |
| 4.6 Other Indicators | 81 |
| 4.7 Discussion | 86 |
| 5 Combination of DMRG and Fixed-Node Monte Carlo | 89 |
| 5.1 Introduction | 89 |
| 5.2 Green Function Monte Carlo | 91 |
| 5.3 Fixed-Node Monte Carlo | 97 |
| 5.4 Stochastic Reconfiguration | 98 |
| 5.5 A guiding wave function from the DMRG | 98 |
| 5.6 Continuum imaginary time limit | 102 |
| 5.7 Implementation issues | 105 |
| 5.8 Results | 105 |
| 5.9 Discussion and Conclusion | 108 |
| Appendices | 111 |
| A SBMF Approximation for $U^\dagger(\mathbf{q})\mathcal{H}U(\mathbf{q})$ | 111 |
| B Transforming the DMRG state to the density matrix basis | 113 |
| List of Publications | 119 |
| Samenvatting | 121 |
| Curriculum Vitae | 125 |

Introduction

Quite a few physical problems give rise to quantum lattice models. Among these are descriptions of high- T_c superconducting materials, metals, insulators and magnets. A quantum lattice model is characterised by quantum objects —spins, fermions or bosons— nicely positioned on a regular lattice. We will restrict ourselves to spins. These are located at the lattice points. The low temperature behaviour of such a model is strongly influenced by quantum zero point fluctuations. These usually suppress the classical order. Sometimes the classical order is even destroyed giving room for other, non-classical types of ordering.

In this thesis insight in the low temperature behaviour will be obtained by a numerical study of the ground state at zero temperature. Two schemes are possible for this purpose and both will be employed.

The first scheme makes a direct estimate of the ground state wave function. An approximate ground state is built and the properties are analysed afterwards. The most successful member of this class is the Density Matrix Renormalisation Group (DMRG). It consists of a systematic, iterative procedure. At every iteration step the energy is minimised in a given subspace of the configurational Hilbert space. This gives a variational approximation to the ground state. Afterwards, a part of the subspace is enlarged and another part is truncated. This transformation is tuned to keep an optimal fraction of the approximation within the altered subspace. To preview one of the comparisons with the second scheme, the DMRG does not suffer from the 'sign-problem' that hampers many other approaches. Below the sign-problem will be explained.

White introduced the DMRG in 1992 [51] and it has proven to be extremely successful for one-dimensional quantum models [19, 33, 53] and two-dimensional classical models [7, 10]. Applications to higher dimensional quantum models are relatively rare [15, 28, 54, 55, 57]. In this thesis we investigate what can be achieved in two dimensions and find that the method has substantial more difficulty with the two-dimensional geometry. We will try to explain this limitation.

The second scheme does not attempt to approximate the ground state but aims at a direct sampling of the properties instead. From this class we will employ the Green Function Monte Carlo simulation (GFMC) [11, 37, 48, 40]. Dimensionality does not play such an important role here as it does in the DMRG method. The essential assumption of the Green Function Monte Carlo simulation, like that of any Monte Carlo simulation, is that the properties of a system can be obtained by measuring them in many representative configurations. Every measurement X_α is accompanied by a weight M_α to express its importance and the average over these measurements, $\sum_\alpha X_\alpha M_\alpha / \sum_\alpha M_\alpha$, will yield the properties. Green Function Monte Carlo simulations suffer from two important shortcomings. The most important one is that quantum mechanical models that contain either frustration or fermions require an extension of these weights M to negative values and the average $\sum_\alpha X_\alpha M_\alpha / \sum_\alpha M_\alpha$ becomes prone to noise as the individual, positive and neg-

ative weights M_α are exponentially larger than their sum. This complication is called the sign-problem. The second limitation is that a priori a good estimate of the ground state has to exist to help the simulation distinguish relevant configurations from less relevant ones. With the introduction of the Fixed Node Monte Carlo (FNMC) the sign-problem can also be cured by incorporating a very good approximation to the ground state in the simulation. The extension of the Fixed Node Monte Carlo to the Green Function Monte Carlo with Stochastic Reconfiguration (GFMC SR) [46] makes the end result less dependent on the quality of the approximation. Still a good approximation remains vital for the method.

The objective of this thesis is two-fold. First, we study the DMRG method to understand its capabilities and limitations in two dimensions. Second, the DMRG will be integrated with a Green Function Monte Carlo simulation. DMRG provides a systematic approximation to the ground state based on the energy. The correlation functions are biased by the implementation of the method. This shortcoming can be overcome by a Green Function Monte Carlo simulation using the DMRG wave function as a guiding wave function. This thesis introduces this new and promising combination of the DMRG and a Green Function Monte Carlo simulation for the first time.

To achieve these objectives, we will first study a well-known model, the *Ising model* in a Transverse Field (ITF) to analyse the DMRG method. Afterwards the DMRG is applied to an unsolved problem, the two-dimensional, antiferromagnetic, frustrated Heisenberg model. Although this model has been attacked by a variety of methods [14, 16, 17, 26, 41, 44, 45, 46, 58] no definite results exist so far for the quantum phase diagram of this model as Monte Carlo simulations are hampered by a fundamental problem called the sign-problem. Strong indications for the existence of a phase without classical ordering are found by DMRG calculations and the combined effort of the DMRG and the Green Function Monte Carlo with Stochastic Reconfiguration. The next paragraphs describe this brief outline in more detail.

The first two chapters focus on the method itself. Chapter one introduces the two-dimensional Ising model in a Transverse Field. It has a direct and clear mapping to a highly anisotropic three-dimensional Ising model, making it almost a blue-print for a model with a quantum phase transition. It does not suffer from the sign-problem and cluster Monte Carlo simulations have yielded high quality numerical results [6] to which we can compare our results. DMRG can only handle relatively small systems and finite-size scaling techniques are necessary to extend the results to larger system sizes. A large fraction of the first chapter is devoted to developing these finite-size scaling techniques. Thanks to the power of the DMRG combined with these scaling relations we can numerically establish the critical field of the two-dimensional Ising model in a Transverse Field upto three significant figures.

The main subject of chapter two is the DMRG technique. A new variant of the method is introduced and afterwards the general properties are described. It seems that DMRG will need amendments or modifications for larger two-dimensional systems. In combination with scaling relations we can however establish the two-dimensional behaviour.

In the following two chapters the DMRG technique is applied to the frustrated Heisenberg model. The frustration in that model appears by competition of nearest-neighbour and next nearest-neighbour interactions. The consequences for the phase diagram are

unclear. The essential question is whether a phase with no classical equivalent exists for intermediate range of frustration. Chapter three is dedicated to the description of the model and the introduction of the spin stiffness ρ_s . The spin stiffness is an excellent indicator of long-range order and should reveal whether an intermediate phase exists. It is studied using a mean field approximation in the Schwinger-boson representation. The reason to resort to a relatively complex mean field approximation is that the ground state of the frustrated Heisenberg model is rotationally invariant. The mean fields can thus not be simply the spin expectation values ($\langle \vec{S} \rangle = 0$). The Schwinger-Boson Mean Field approximation (SBMF) inserts the mean fields in the interactions of neighbouring spins, $\vec{S}_i \cdot \vec{S}_j$. This not only overcomes the complication of the rotational invariance, but it also extends the mean fields to local correlations. It yields a rotationally invariant ground state but the spin length $\frac{1}{2}$ cannot be strictly conserved.

The spin stiffness in this approximation does not reveal an intermediate phase, but it serves very well for an analysis of the finite-size scaling behaviour. This helps us to extend the numerical results of the next chapter to an infinitely large system.

Chapter four outlines the numerical calculation including the technique to obtain the spin stiffness, guided by the results of chapter three. Like many other methods, The DMRG do not give a definitive answer on the existence of an intermediate phase, but it provides clear information on infinitely long strips of widths upto eight sites.

The final chapter combines the DMRG and the Green Function Monte Carlo with Stochastic Reconfiguration. The frustrated Heisenberg model belongs to the class where Monte Carlo simulations suffer from the sign-problem. As mentioned above a good guidance is essential for the Green Function Monte Carlo with Stochastic Reconfiguration. For a long time finding an proper approximation to the ground state has been the bottleneck of all Green Function Monte Carlo variants as a large amount of research time had to be spent on designing it. The DMRG can provide such an approximate ground state for many different models, including the frustrated Heisenberg model. In this chapter it is outlined how to combine both methods and the phase diagram of a 10×10 system is studied. This combination of the DMRG and a Green Function Monte Carlo simulation is new and promising. Further extensions, along the lines of forward-walking schemes [8], may even be able to obtain accurate values for the spin-spin correlations.

This thesis will hopefully provide a good understanding of the intricacies of the DMRG method. The last chapter resolves a long standing problem of the Green Function Monte Carlo and the last three chapters give indications of the intermediate phase of the frustrated Heisenberg model although no definite statements can be made.

Acknowledgement

Although this thesis only bears the name of one author, there are many people I had the pleasure of sharing ideas with. Let me mention prof. dr. Steve White, who I visited at University of California in Irvine, and prof. dr. Daniel Aalberts, who invited me to Williams College in Massachusetts. Jeroen Doumen performed some of the computations described in the first chapter.

1 Ising model in a Transverse field

1.1 Introduction

Since the beginning of the 1960s, the Ising model in a Transverse field (ITF) has been studied. In first instance, this quantum mechanical model was employed to describe the order-disorder transition in some double-well ferroelectric systems like KH_2PO_4 crystals. This interest has survived to the present day, but the scope has widened.

A decade later the renormalisation group and with it the notion of universality was introduced. The Ising model often served as a test ground and consequently it was scrutinised. The d dimensional ITF can be mapped onto a $d + 1$ dimensional Ising model. This relation makes it an excellent vehicle to introduce the concepts of phase transitions in the realm of quantum mechanics.

Sachdev, Read and others [42, 13] have used the ITF for the same role as the Ising model has played in the context of classical critical phenomena: a blue-print of phase transitions and universality. Maybe the most important difference lies in the fact that it is not the temperature T that induces a phase transition, but a coupling constant H that can drastically alter the properties of the system. With the disappearance of the temperature, $T = 0$, it is the ground state that exhibits this quantum phase transition.

On the outset our intention is to investigate the density matrix renormalisation group (DMRG). The ITF is chosen as a 'toy-model' both because of its rich behaviour and its simple description.

In this chapter, the model will be explained. The exact results in one dimension (a chain) will be reviewed and subsequently a large effort is made to uncover the finite-size scaling behaviour for the two-dimensional case. Given the restriction of the DMRG, which will be discussed in the next chapter, it is worthwhile to scale the length of the system to infinity first, after which the finite width can be scaled away. The results, table 1-3, clearly support such a two-stage process.

A good review of the ITF has been published by Chakrabarti et al. [13], relieving us of the duty to go into great detail. The numerical treatment is left to the next chapter.

1.2 The Model

Consider a two dimensional square lattice with length L and width W . The lattice is periodic in both directions and each lattice site contains a spin- $\frac{1}{2}$. The Hamiltonian is given by

$$\mathcal{H}_{ITF} = \sum_{l=1}^L \sum_{w=1}^W \left\{ -4S_{l,w}^x (S_{l+1,w}^x + S_{l,w+1}^x) + 2HS_{l,w}^z \right\} \quad (1.2.1)$$

where the $S_{l,w}^\alpha$ are the usual spin- $\frac{1}{2}$ matrices satisfying the commutation relations

$$[S_{l,w}^\alpha, S_{l',w'}^\beta] = i\delta_{l,l'}\delta_{w,w'}\epsilon_{\alpha\beta\gamma}S_{l,w}^\gamma, \quad \alpha, \beta, \gamma = x, y, z \quad (1.2.2)$$

Clearly the energy scale of this Hamiltonian is set to unity. We have chosen the convention of spin- $\frac{1}{2}$, in contrast with the Pauli-matrices frequently used in this field. The factor of 4 and 2 are inserted in the definition (1.2.1) to make our results directly comparable to the main part of the literature.

Let us summarise the main symmetry properties of this model. The Hamiltonian with field H can be transformed into one with $-H$ by a spin rotation round the S^x -axis over 180 degrees. This is a unitary transformation so we have the freedom to choose $H > 0$. The model is translation and reflection symmetric in both directions.

An important symmetry that will be extensively used, is the spin-reversal operator S . It is associated with a rotation over 180 degrees round the S^z axis;

$$S^\dagger S^x S = -S^x, \quad S^\dagger S^y S = -S^y, \quad S^\dagger S^z S = S^z.$$

and can be expressed as

$$S = \exp \left[i\pi \left(\sum_{l,w} S_{l,w}^z + \frac{LW}{2} \right) \right]. \quad (1.2.3)$$

The offset of $LW/2$ allows us to associate the quantum number $S = 1$ with the ground state $|\psi_0\rangle$ for different system sizes. (In short: $S|\psi_0\rangle = |\psi_0\rangle$). One can state that the spin reversal operator samples the number of up-spins and returns whether it is even, $S = 1$, or odd, $S = -1$.

If $H \rightarrow 0$, we end up with a simple, classical, two-dimensional Ising model. The ground state is degenerate; all spins point forwards or backwards in the S^x -direction. The associated phase is named the classically ordered phase. The two classical solutions, forward and backward pointing spins, can be superposed in a quantum mechanical sense. In this manner states can be obtained that are either even ($S = +1$) in spin-reversal or odd ($S = -1$). The statement made before about the ground state, $S|\psi_0\rangle = |\psi_0\rangle$ still holds for one of them, but the other ground state $|\psi_1\rangle$ lies in the odd subspace, $S|\psi_1\rangle = -|\psi_1\rangle$.

In the other extreme, $H \rightarrow \infty$, the degeneracy is lifted. The model essentially describes free spins in an external field. The ground state is unique and has all spins pointing down in the S^z -direction. This is the reference state for the quantum disordered phase and again has the quantum number $S = +1$. The lowest excitation differs from the ground state by the reversal of one spin. So it belongs to the class $S = -1$. We will extensively study the energy gap Δ between the lowest excitation (in $S = -1$) and the ground state (in $S = +1$). $\Delta = E_1 - E_0$.

There is a phase transition between the classically ordered and the quantum disordered state. A clear signature of this phase transition is the appearance of the gap Δ , which occurs for a critical value $H = H_c$. In figure 1-1 all these properties are summarised in a graphical representation. As we will show later the relation between the gap Δ and the field can be made more explicit by

$$\Delta \sim |H - H_c|^\nu. \quad (1.2.4)$$

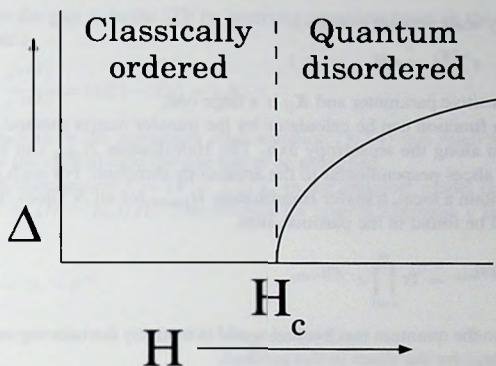


Figure 1-1. The phase diagram for the ITF and the energy gap Δ associated with it. At the critical field H_c a phase transition occurs and the gap Δ opens up. Further explanation is given in the text.

for $H > H_c$. Below the critical field, $H < H_c$, the ground state becomes degenerate. The gap Δ should then be defined as the energy difference between the ground state and the first excitation *within* the even subspace for equation (1.2.4) to hold. In the rest of the chapter we will not redefine the gap but only consider $H > H_c$.

It will take another section to prove that the critical exponent ν is identical to the critical exponent of the three-dimensional classical Ising model. After that we focus on extracting both the critical field H_c and the critical exponent ν for the two-dimensional ITF.

1.3 Connection with the 3-dimensional Ising model

The ITF has an intimate connection with a highly anisotropic Ising model in one dimension higher. Although we will only show this explicitly for the 2-dimensional ITF, the argument holds in general.

As starting point we take a highly anisotropic, ferromagnetic Ising model in three dimensions. The classical spins $s^z = \pm 1$ interact according to the Hamiltonian

$$-\beta \mathcal{H}_{\text{clas}} = K_{\perp} \sum_{(ij)} s_i^z s_j^z + K_{\parallel} \sum_{(ij)} s_i^x s_j^x, \quad (1.3.1)$$

on a cubic lattice at an inverse temperature β . The first term contains the interactions between nearest neighbours (denoted by (ij)) in the plane perpendicular to the anisotropy axis. The second term contains those along the anisotropy direction. The coupling constants K_{\perp} and K_{\parallel} give rise to this anisotropy. We link them to the field in equation (1.2.1)

where the energy scale was set to unity,

$$K_{\perp} = \varepsilon, \quad e^{-2K_{\parallel}} = \varepsilon H, \quad \varepsilon \ll 1, \quad (1.3.2)$$

K_{\perp} is a small, positive parameter and K_{\parallel} is a large one.

The partition function can be calculated by the transfer matrix method. We choose the transfer direction along the anisotropy axis. The Hamiltonian \mathcal{H}_{clas} can be split in interactions between slices perpendicular to the anisotropy direction. For each pair of adjacent slices we then obtain a local, transfer Hamiltonian \mathcal{H}_{trans} for all N slices. The connections with the ITF will be found in the partition sum,

$$Z = \text{Tr} e^{-\beta \mathcal{H}_{clas}} = \text{Tr} \prod_{n=1}^N e^{-\beta \mathcal{H}_{trans}}.$$

The connection to the quantum mechanical world is made by introducing summation over complete bases $|\alpha_n\rangle$ for the slices in this product;

$$Z = \sum_{\{\alpha_n\}} \prod_{n=1}^N \langle \alpha_n | e^{-\beta \mathcal{H}_{trans}} | \alpha_{n+1} \rangle,$$

with periodic boundary conditions, $|\alpha_{N+1}\rangle = |\alpha_1\rangle$. The parameters K_{\perp} and K_{\parallel} were chosen so anisotropic that we may approximate the exponentials;

$$\begin{aligned} \langle \alpha_n | \exp \left(K_{\parallel} \sum_{(i,j)} S_i^z S_j^z \right) | \alpha_{n+1} \rangle &= e^{K_{\parallel}} \langle \alpha_n | 1 + 2e^{-2K_{\parallel}} \sum_{l,w} S_{l,w}^x | \alpha_{n+1} \rangle, \\ \langle \alpha_n | \exp \left(K_{\perp} \sum_{(i,j)} S_i^z S_j^z \right) | \alpha_{n+1} \rangle &= \langle \alpha_n | 1 + 4K_{\perp} \sum_{l,w} S_{l,w}^z (S_{l+1,w}^z + S_{l,w+1}^z) | \alpha_{n+1} \rangle \end{aligned}$$

All of the above is combined in the resulting partition function

$$Z e^{-N K_{\parallel}} = \text{Tr} \prod_{n=1}^N \left\{ 1 + \varepsilon \left[\sum_{l=1}^L \sum_{w=1}^W (4 S_{l,w}^z (S_{l+1,w}^z + S_{l,w+1}^z) + 2 H S_{l,w}^x) \right] \right\}$$

The right side of the equation can easily be mapped onto the definition of the ITF in equation (1.2.1) by some simple, unitary transformations: we exchange the S^z - and S^x -direction and afterwards rotate the spins over π round the S^z axis (using the unitary operator $\exp(i\pi \sum_j S_j^z)$). The trace is invariant under these unitary transformation, so the outcome is

$$Z e^{-N K_{\parallel}} = \text{Tr} e^{-N \varepsilon \mathcal{H}_{ITF}}. \quad (1.3.3)$$

Careful analysis reveals that this relation holds up to order $\mathcal{O}(\varepsilon^2)$. Along with this connection come quite a few others; the correlation function ξ , formally defined by the covariance of Ising spins located at location $(l, w, 1)$ and (l, w, n) ;

$$\langle S_{l,w,1}^z S_{l,w,n}^z \rangle - \langle S_{l,w,1}^z \rangle \langle S_{l,w,n}^z \rangle \sim e^{-n/\xi},$$

can be related to the gap Δ in the ITF by inserting complete bases in the same fashion as above. The result is

$$\xi^{-1} = \ln \frac{e^{-\varepsilon E_1}}{e^{-\varepsilon E_0}} = \varepsilon(E_1 - E_0) = \varepsilon \Delta. \quad (1.3.4)$$

As mentioned before in the paragraph after equation (1.2.4) this relation only holds for $H > H_c$. Below the critical field the gap has to be redefined.

The reduced temperature $t = (T - T_c)/T_c$ in the classical model is replaced by the reduced field $h = (H - H_c)/H_c$. The relation for critical exponent ν thus also finds its equivalent;

$$\frac{1}{\xi} \sim t^{2\nu} \rightarrow \Delta \sim h^{2\nu}.$$

In the expression we use that for the 3D Ising model $z = 1$

1.4 Exact solutions for the ITF chain

The properties of the two-dimensional system can only be obtained by use of finite-size scaling. In doing so, the results for the open ITF chain will provide a crucial reference. Here we briefly review those. The reason not to follow Pfeuty [38] is that he considers an infinitely long chain, whereas here it is essential that the chain is both finite and open. Given the beauty of exact solutions, we can not resist in presenting also the results for the finite periodic chain.

The essential ingredient to the exact solution of the ITF chain is a Jordan-Wigner transformation [38] to spin-less fermions c_j ,

$$S_i^+ = \prod_{j=1}^{i-1} e^{ic_j^\dagger c_j} c_j.$$

In terms of these operators the Hamiltonian reads

$$\mathcal{H} = -HL + 2H \sum_{j=1}^L c_j^\dagger c_j - J \sum_{j=1}^{L-1} (c_j^\dagger - c_j)(c_{j+1}^\dagger + c_{j+1}) + \mathcal{H}_{per}. \quad (1.4.1)$$

The term \mathcal{H}_{per} governs the interactions between the first and the last site. If the chain is open, these do not exist, $\mathcal{H}_{per} = 0$. For a periodic chain

$$\mathcal{H}_{per} = J (c_L^\dagger - c_L)(c_0^\dagger + c_0) S. \quad (1.4.2)$$

This equation reintroduces another observable, the spin-reversal operator S , defined as

$$S = \exp i\pi \sum_{j=1}^L c_j^\dagger c_j.$$

The current definition is identical to the original one in equation (1.2.3). It is a conserved quantity as the only change in the number of fermions occurs in the second term of the Hamiltonian (1.4.1) by pair creation or annihilation. As an empty chain corresponds to all spins pointing downwards, the ground state has to be in the even, $S = 1$, subspace. Moreover these pairs of operators in the Hamiltonian \mathcal{H} make it already clear that it can be diagonalised via a Bogoliubov transformation. For the periodic chain we can go even further and derive exact expressions for the excitation spectrum. The open-chain properties require the numerical diagonalisation of a $L \times L$ matrix to get all energy levels and eigenstates.

1.4.1 The periodic chain

We want to Fourier transform the particle creation and annihilation operators in the usual manner

$$c_k = \sum_{l=1}^L e^{ikl} c_l.$$

The allowed k -values depend on the number of fermions present on the chain; for an odd number, $S = -1$, the boundary term \mathcal{H}_{per} , equation (1.4.2), has the same sign as all other interactions. The Hamiltonian \mathcal{H} becomes translational invariant and we can take the regular k -values;

$$k = \frac{2\pi l}{L}, \quad 0 \leq l < L. \quad (1.4.3)$$

For even number of fermions, $S = 1$, the boundary conditions are antiperiodic and the set of k -values has to be adjusted accordingly;

$$k = \frac{(2l+1)\pi}{L}, \quad 0 \leq l < L. \quad (1.4.4)$$

The Hamiltonian \mathcal{H} is now converted to the momentum space representation and to represent it compactly we define $p(k) = -2H + 2J \cos(k)$ and $q(k) = 2J \sin(k)$. It reads

$$\begin{aligned} \mathcal{H} = & -HN - \sum_{0 < k < \pi} p(k) \left(c_k^\dagger c_k + c_{-k}^\dagger c_{-k} \right) \\ & + i \sum_{0 < k < \pi} q(k) \left(c_k^\dagger c_{-k}^\dagger + c_k c_{-k} \right) + \mathcal{H}_{0,\pi}, \end{aligned}$$

where the allowed k -values are defined in (1.4.3) and (1.4.4). The wave vector $k = 0$ and $k = \pi$ —treated in $\mathcal{H}_{0,\pi}$ — are not always allowed. If they are, see table 1-1, they play a special role in that they already appear in a diagonal form;

$$\mathcal{H}_{0,\pi} = \delta_0 \text{ allowed } p(0) c_0^\dagger c_0 + \delta_\pi \text{ allowed } p(\pi) c_\pi^\dagger c_\pi.$$

| Length | S=-1 | S=1 |
|--------|-----------|--------------|
| even | - | $k = 0, \pi$ |
| odd | $k = \pi$ | $k = 0$ |

Table 1-1. The $k = 0$ and $k = \pi$ values will only occur for certain length and number of fermions.

Apart from these, all the terms have to undergo a Bogoliubov transformation. Next we provide the main formulas to diagonalise those: define the canonical transformation

$$c_k = u(k)\eta_k - i v(k)\eta_{-k}^\dagger,$$

with

$$\begin{aligned} u(k) &= \cos \theta_k, & v(k) &= \sin \theta_k, \\ \cos 2\theta_k &= \frac{p(k)}{\lambda(k)}, & \lambda(k) &= \sqrt{p^2(k) + q^2(k)}. \end{aligned}$$

The exact expression for the Hamiltonian now is

$$\mathcal{H} = E_{\text{off}} + \sum_{0 < k < \pi} \lambda(k) \left(\eta_k^\dagger \eta_k + \eta_{-k}^\dagger \eta_{-k} \right) + \mathcal{H}_{0,\pi},$$

with

$$E_{\text{off}} = -\frac{1}{2} \sum_k \lambda(k).$$

It is important to stress that the form of the Hamiltonian \mathcal{H} depends on the number of fermions present. Creating one excitation by creating a single fermion will change the parity of the number of particles; the only allowed excitations within the subspace are built from pairs of fermions, i. e. $\eta_i^\dagger \eta_j^\dagger |\psi_0\rangle$. To obtain an excitation in the other subspace, we have to start with the lowest energy state *within* that subspace and create pairs of excitations on that.

1.4.2 The open chain

In the case of the periodic chain we are fortunate that the translational invariance allows a Fourier transformation. The modes become almost decoupled afterwards and an exact expression can be derived by a Bogoliubov transformation.

The open chain is not translation invariant and no further analytical steps can be taken. The numerical procedure remains straightforward. Van Hemmen [24] describes in detail how to derive both the energy spectrum and all eigenstates of a fermionic system for a general pair-wise interaction. Applying the relevant transformations leads again to a diagonal Hamiltonian containing excitation occupation numbers offsetted by the ground state energy E_0 .

In figure 1-2 the scaled gap $L\Delta$, on which we will focus from now on, is depicted for both the open and the closed chain. They show similar behaviour, although in the vicinity of the phase transition their ratio becomes quite large.

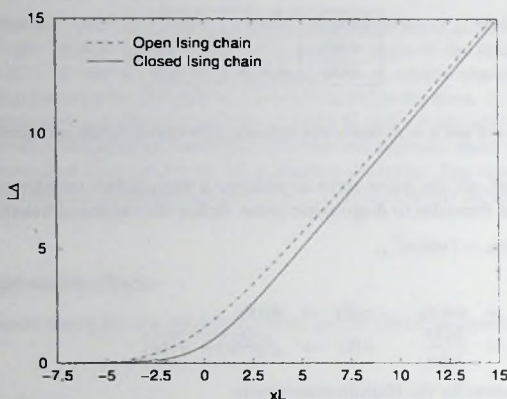


Figure 1-2. The behaviour of the energy gap Δ as function of the combination of $x = H/J$ and the length L of the system. The only difference between the lines is the boundary condition.

1.5 Finite-size scaling

We want to establish properties of the 2D ITF through numerical means. In general it is not possible to obtain direct quantitative information on an infinitely large system. A widely used indirect route is to calculate the desired quantities for a set of finite systems and extract their values for the infinite-size limit by investigating their dependencies on the systems size. This method is called finite-size scaling. Anticipating that for our numerical method, the density matrix renormalisation group, the length of the system imposes less restrictions than the width, we will first develop the scaling relations to scale the length $L \rightarrow \infty$. Afterwards we derive the relations for $W \rightarrow \infty$. A final subsection is spent on studying the scaling behaviour for fixed aspect ratio L/W and $L \rightarrow \infty$. The properties of the 2D system are independent of the route taken to derive them, therefore both approaches should yield the same results in the limit of infinite system size.

Although the Density Matrix Renormalisation Group (DMRG) will not be introduced until the next chapter, the results are incorporated in the following scaling analysis. DMRG calculations were performed to obtain the lowest energies in the even and odd subspace. The difference is the energy gap Δ . The parameters of the calculations were $H = 3.00, \dots, 3.10$ in steps of 0.01 and $L/W = 2, \dots, 5$ in steps of 0.5. For widths $W = 7, 8$ the largest ratio was $L/W = 4$.

1.5.1 1-Dimensional, W fixed, $L \rightarrow \infty$

There are two reasons to scale the length L to infinity first. The first one has to do with the open boundary conditions. As we will discuss in the next chapter, closing the boundaries in the length direction and making the system translation invariant will severely hamper the accuracy of the calculation. Open systems give rise to complex finite-size effects by their lack of translational invariance. These effects will disappear if we scale the length $L \rightarrow \infty$ where open and periodic systems become indistinguishable.

The second reason is of a more practical nature. The fact that DMRG functions so extremely well for quantum chains [51], indicates that varying the length L of the system will not have a large impact on the accuracy. Unfortunately this does not hold for the width W of the system. In the next chapter, section (2.6.1), we will show that in order to maintain the accuracy, the size of the calculation grows exponentially with the width W of the system. With a large range of lengths and only a few widths that we can handle, it seems wise to remove all the dependence on the length first. We will thereby obtain fairly accurate results for infinitely long strips.

Let us now outline the procedure: once the length L has become sufficiently large, a system of dimensions $L \times W$, with fixed width W , will start to behave as a one-dimensional system. Such a system will by arguments of universality resemble an open chain, so we expect for fixed width W , that

$$L\Delta(x, W, L) = A(W) \left\{ f_0(B(W)xL) + \frac{1}{L} f_1(B(W)xL) + \dots \right\}. \quad (1.5.1)$$

This scaling relation contains quite some new elements that deserve either an introduction or an explanation:

- $L\Delta$. Given the connection to the Ising model, Δ has to correspond to an inverse length. Rescaling the length will thus automatically lead to the appearance of the combination $L\Delta$.
- $f_0(\dots)$ and $f_1(\dots)/L$. These are respectively the leading order and the first correction of the finite-size behaviour of the open ITF chains. We obtained these functions numerically. Knowing that the correction arises from a surface contribution (the chain is open), the factor $1/L$ in $f_1(\dots)/L$ is obvious.
- xL . Universal behaviour concerns the system properties in the vicinity of the phase transition. Every width has its own critical field $H_c(W)$, so $x = H - H_c(W)$. One dimensional critical behaviour is accompanied by the critical exponent $\nu = 1$. The combination thus has to be $xL^\nu = xL$.
- $A(W)$ and $B(W)$. The theory of universality makes predictions on the exponents near a phase transition, not on the overall scales. These can vary for the different width strips.

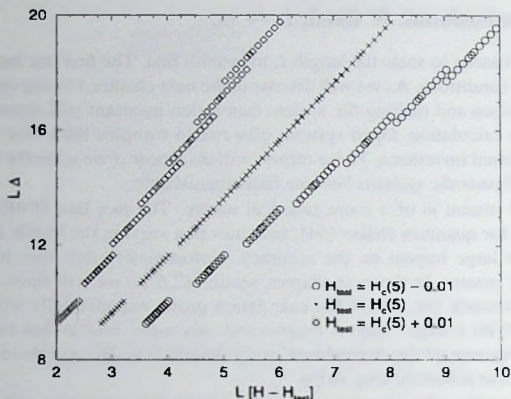


Figure 1-3. The critical field $H_c(W)$ can be obtained by 'smoothing' the curve of $L\Delta$ versus xL . Depicted is the case for $W = 5$ and $H_c(W) = 2.867$.

It has to be stressed that only the form of the leading term, $f_0(B(W)xL)$, is fixed by universality. The form of the correction term, $f_1(B(W)xL)/L$, is an assumption. We just take the simplest form that also suits the open chain.

The scales $A(W)$, $B(W)$ and the critical fields $H_c(W)$ can be considered fitting parameters to make relation (1.5.1) agree with the data. In the following we will describe how we obtained these parameters and what the outcome is.

The standard fitting procedure is to adjust the parameters such that all data points are fitted best according to a least-square functional. The critical field $H_c(W)$ can also be derived independently through another, simpler route. In practice this approach is taken. If the right $H_c(W)$ is chosen, plotting $L\Delta$ versus xL must give a smooth curve for large enough L . From this feature we will extract $H_c(W)$. An example of this procedure is given in figure 1-3.

With $H_c(W)$ already found, only $A(W)$ and $B(W)$ have to be obtained from data collapse. We can fit the data x, L, Δ to the formula (1.5.1), as both f_0 and f_1 can be obtained from the open ITF chain. Figure 1-4 reveals that indeed the data shows nice, universal behaviour with the calculated f_0 . The corrections due to f_1 are removed from this figure. They are relatively small. Table 1-2 lists the results.

The general expression for the gap Δ at infinite system length $L = \infty$ can be found by examining the behaviour of $f_0(y)$ and $f_1(y)$ at large argument y more closely: for large argument y (or field) the ITF Hamiltonian describes free spins in an external magnetic field

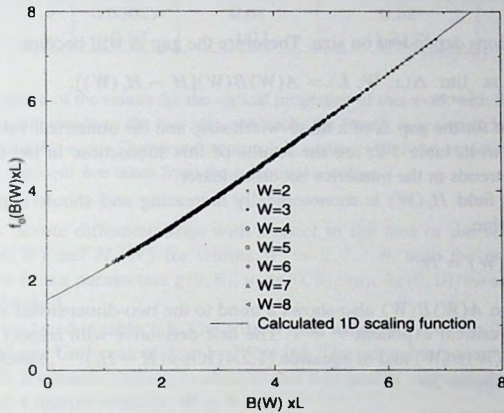


Figure 1-4. The data obtained by DMRG calculations is fitted to scaling relation (1.5.1). The figure shows scaling collapse nicely.

| W | $H_c(W)$ | $A(W)$ | $B(W)$ | $A(W)B(W)$ |
|-----|----------|--------|--------|------------|
| 2 | 2.296 | 2.601 | 0.853 | 2.219 |
| 3 | 2.646 | 3.096 | 0.829 | 2.567 |
| 4 | 2.792 | 3.343 | 0.874 | 2.922 |
| 5 | 2.867 | 3.492 | 0.834 | 3.262 |
| 6 | 2.912 | 3.586 | 0.998 | 3.579 |
| 7 | 2.941 | 3.695 | 1.055 | 3.898 |
| 8 | 2.961 | 3.754 | 1.118 | 4.197 |

Table 1-2. From the one-dimensional scaling procedure these values can be extracted. The expression of the gap for the infinite long periodic strip is given in equation (1.5.2).

with strength y . An excitation can be made by flipping one spin upwards, thus

$$\lim_{y \rightarrow \infty} \frac{f_0(y)}{y} = 1,$$

with no corrections dependent on size. Therefore the gap Δ will become

$$\Delta(x, W) \equiv \lim_{L \rightarrow \infty} \Delta(x, W, L) = A(W)B(W)[H - H_c(W)]. \quad (1.5.2)$$

This relation for the gap Δ of a finite-width strip and the numerical value of the quantities appearing in it, table 1-2, are the results of this subsection. In the light of the gap expression, the trends in the numerics become clearer:

The critical field $H_c(W)$ is monotonically increasing and should approach the two-dimensional value,

$$\lim_{W \rightarrow \infty} H_c(W) = H_c.$$

The combination $A(W)B(W)$ also shows a trend to the two-dimensional situation. In two dimensions the critical exponent $\nu < 1$. The first derivative with respect to the field H , which is here $A(W)B(W)$ and in equation (1.2.4) it is $\nu(H - H_c)^{\nu-1}$, should diverge at the phase transition point. So

$$\lim_{W \rightarrow \infty} A(W)B(W) = \infty.$$

The trend is in the data but $W = 8$ is far too small for this combination to grow excessively.

1.5.2 2-Dimensional, $W \rightarrow \infty$, $L = \infty$.

Standard scaling methods as described in [9], can be implemented now:

$$\Delta(h, W) = \frac{1}{W} g(h W^{1/\nu}, u_i W^{y_i}). \quad (1.5.3)$$

The reduced field h is given by $h = H - H_c$ (remember $H_c \equiv H_c(\infty)$); true two-dimensional scaling behaviour is considered, in contrast with equation (1.5.1). The finite-size corrections are anticipated by the inclusion of the irrelevant field u_i and exponent y_i . In the previous subsection also an expression for the gap Δ was given in equation (1.5.2). As both, this one and the scaling relation above must hold, they have to be identical:

$$A(W)B(W)[h + H_c - H_c(W)] = \frac{1}{W} g(h W^{1/\nu}, u_i W^{y_i}).$$

The left side of this identity is linear in h . The right part also contains higher order terms, which we will neglect. Expanding both sides up to linear order yields:

$$\begin{aligned} A(W)B(W)W[H_c - H_c(W)] &= g(0, 0) + W^{y_i} u_i \frac{\partial g}{\partial u_i}(0, 0), \\ A(W)B(W)W &= W^{1/\nu} \frac{\partial g}{\partial h}(0, 0) + W^{1/\nu + y_i} u_i \frac{\partial^2 g}{\partial u_i \partial h}(0, 0). \end{aligned}$$

| | Literature | first $L \rightarrow \infty$ then $W \rightarrow \infty$ | $L = QW \rightarrow \infty$ |
|-------|------------|---|-----------------------------|
| H_c | 3.0444 | 3.0449 | 3.0439 |
| ν | 0.63029 | 0.61 | 0.62 |
| y_i | -0.83 | -1.21 | -1.21 ^(*) |

Table 1-3. Comparison of the results for the critical properties of this work with those by Blöte [6]. The first result corresponds to the two step approach: the length is scaled to infinity, $L \rightarrow \infty$, afterwards the width $W \rightarrow \infty$. The second approach is scaling with fixed aspect ratio. ^(*) the value for the irrelevant exponent was taken from the anisotropic scaling.

The derivatives denote differentiations with respect to the first or the second argument. (Deriv. $A(W)$, $B(W)$ and $H_c(W)$ for widths $W = 2, \dots, 8$, both the critical properties H_c , ν and the fitting parameters $g(0, 0)$, $u_i \partial g(0, 0)/\partial u_i$, $\partial g(0, 0)/\partial h$ and $u_i \partial^2 g(0, 0)/\partial u_i \partial h$ can be obtained.

The results are listed in table 1-3. The critical field we obtain is of similar quality as obtained by cluster Monte Carlo calculation by Blöte [6]. The critical exponent is of substantial less quality. Still, it remains striking to observe that this quality can already be achieved by considering such a narrow systems, $W \leq 8$!

1.5.3 2-Dimensional, $L, W \rightarrow \infty$ with fixed aspect ratio L/W .

The aspect ratio $Q = L/W$ is fixed and the second step (1.5.3) in the previous approach can be implemented immediately;

$$\Delta(h, W, L) = \frac{1}{L} f(hL^{1/\nu}, u_i L^{y_i}, Q).$$

As we consider fields close to the critical field, $|h| \ll 1$, and the corrections to scaling are expected to be relatively small, this is expanded up to linear order:

$$\begin{aligned} L\Delta &= f(0, 0, Q) + L^{y_i} u_i \frac{\partial f}{\partial u_i}(0, 0, Q) \\ &+ hL^{1/\nu} \left(\frac{\partial f}{\partial h}(0, 0, Q) + L^{y_i} u_i \frac{\partial^2 f}{\partial u_i \partial h}(0, 0, Q) \right). \end{aligned} \quad (1.5.4)$$

The critical properties H_c , ν and y_i are not dependent on the aspect ratio Q . All others, $f(0, 0, Q)$, $u_i \partial f(0, 0, Q)/\partial u_i$, $\partial f(0, 0, Q)/\partial h$ and $u_i \partial^2 f(0, 0, Q)/\partial u_i \partial h$, do. The parameters were extracted by a least square fit to all of the data available. The systems considered had a range of properties; widths $4 \leq W \leq 8$, $Q = 2, 2.5, 3, 3.5, 4, 4.5, 5$ (the fractional aspect ratio's were only considered with even width W) and fields $3.00 \leq H \leq 3.10$. In total 471 points were fitted to this behaviour. An optimal fit can be made for a large range

of parameters. We therefore had to fix $y_i = -1.21$; the value found in the anisotropic scaling. If the least square fit is made unrestricted, unreasonable critical exponents will result. The outcome is listed in table 1-3.

1.6 Conclusion

In this chapter we derived the critical field H_c and exponent ν of the two-dimensional ITF. Two routes were taken: one was to scale the length of the system to infinity and afterwards the width. The other route followed the usual path of scaling; the linear dimension was rescaling in both directions.

The two-step scaling approach was prompted by the strengths and weaknesses of the DMRG. Table 1-3 clearly indicates that this makes sense; the accuracy of the critical field H_c may be considered unexpected in view of narrow systems considered. The critical exponents are not too impressive.

Although the essential ingredient in these calculations is the DMRG, no time was spent on the procedure or the properties. The next chapter contains that half of the research. The complication that was mentioned, strong limitations on the width of the system, is a very general feature of the method. Later on, in chapter 4 where the frustrated Heisenberg is investigated, the same problem will reappear.

Apart from two constants, H_c and ν , this chapter has given us an excellent playground to test the DMRG and a first taste of finite-size scaling in quantum magnetism. This will be of use for the frustrated Heisenberg model.

2 Critical properties of the ITF through DMRG calculations

2.1 Introduction in the Density Matrix Renormalisation Group

In this chapter the density matrix renormalisation group (DMRG) is introduced and studied. This method was originally proposed by White [51] in 1992 to resolve some of the problems that the real space renormalisation group (RSRG) suffers from; in contrast with the successful treatment of the Kondo problem, the RSRG gives—relatively—poor results for strongly interacting quantum chains.

It is well established by now, that the DMRG can handle this class of lattice problems extremely well, making it the method of choice for one-dimensional quantum lattice systems. Already in the initial papers [51] the promise became apparent. The treatment of the spin-1 Heisenberg chain [53] demonstrated the capabilities of the method. The accuracy was unprecedented.

The method is variational and systematic. If the computation is scaled up sufficiently, the approximation the ground state that is made, has to be accurate. The surprise lies in the fact that this situation can easily be achieved with a minor computational effort. Some theoretical investigation on the grounds for this tremendous accuracy has been made [35], but no clear understanding exists at the present. At the same time the applications have started to diversify. Three main trends can be observed.

The first one is usage of the method in two-dimensional classical problems. Bursill et al. [7] followed the standard route of a transfer matrix description to transform a two-dimensional classical model into a one-dimensional quantum system. Carlon and Drzewiński [10] build on this extension to settle some of the outstanding issues in that field.

The second diversification is in the direction of chemical molecules. Historically, physicists and chemists alike have tried to develop simple models of chemical compounds that allowed a theoretical treatment. A good example is the Su-Schrieffer-Heeger Hamiltonian to model the valance electrons in a polymer. It simplifies the individual atoms to lattice points, whereby a one-dimensional quantum lattice model is formed. For a proper treatment the Coulomb interaction has to remain long ranged and should not be restricted to individual sites. Despite this long-range interaction, it seems that the DMRG can still achieve good accuracy although the issue is not completely decided yet [5].

The other direction, upgrading the method to deal with more realistic molecular models, has also been tried. White and Martin [56] have applied the DMRG to the orbital description of water. They concluded that the accuracy compares favourably with many other numerical methods.

The third extension is also our main interest, the application to wider systems. Noack et

al. [34] focused on the two-leg Hubbard ladder, while White and Scalapino [55] investigate the t-J model on a 16×8 lattice. We [15] were specifically interested in the limitations of the DMRG on wide systems. It seems that DMRG is not well suited to handle two-dimensional quantum systems, although with tricks and brute-force computer power reasonable results can be achieved. In this chapter we explain what the difficulties are.

As a testing ground we use the ITF. The ITF constitutes of a well understood and simple case of a two dimensional model with a quantum phase transition. The performance of the DMRG is expected to decrease in the vicinity of a phase transition, making the ITF our model of choice. Moreover cluster Monte Carlo calculations [6] have resulted in accurate numerical values for its critical properties to which we can relate.

The aim of the method is to find an approximation to the ground state wave function. This is done by 'bootstrapping'; the approximation to the ground state is improved iteratively. To represent the ground state a basis in the Hilbert space is necessary. This basis is systematically improved by the DMRG. Typically, the route taken is to start with a basis for one site and iterative enlarge the Hilbert space by adding sites. Without further ado the size of the basis would then grow exponential like the Hilbert space at each addition. To avoid this, the most relevant basis states are selected and all others are removed.

The route we follow in this chapter is first to introduce and discuss the density matrix which is the key ingredient of the method. Next the geometrical properties of the systems we study are listed. Of the two procedures we implemented, one has extensively been described in the literature [51, 19]. The other one was introduced by us [15] and will be reviewed here. With the method in place, a link with the RSRG is made. After that, the performance and the flexibility of the two procedures is compared. The original proposal by White is the more flexible of the two whereas our implementation has the potential to be the fastest.

The remainder contains two less related sections, one on the actual results for the ITF model and one on implementation issues.

2.2 The Density Matrix

Suppose we have a state $|\phi_0\rangle$. This can be the ground state, but for the moment we leave that open. In the DMRG we want to find a basis to represent this $|\phi_0\rangle$ as well as possible. For the entire system, this statement is trivial; the only required basis vector is the state itself. If on the other hand the system is divided in a part A and B , both containing a number of sites, as depicted in figure 2-1, we can find the most relevant fraction of the basis in part A . Our aim is to truncate the basis to this relevant part and remove the rest of the basis. A restriction to these basis states should allow an optimal representation $|\tilde{\phi}_0\rangle$ of the ground state $|\phi_0\rangle$. By optimal we mean that the truncation error P ,

$$P = \left| |\phi_0\rangle - |\tilde{\phi}_0\rangle \right|^2,$$

is minimal. We have to select those m basis states in A that minimise the truncation error P .

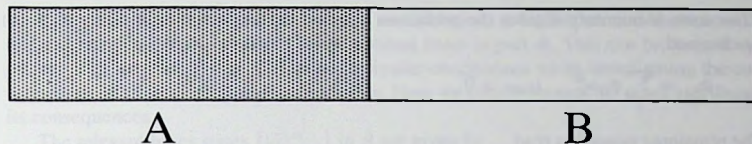


Figure 2-1. The system is divided in a left part A and a right part B , both containing a number of sites. With both these parts an incomplete basis is associated. In the future, a generalisation will often be used; the system is split in three or four parts by treating either one or both of the intermediate sites (last site of A and first site of B) separately.

Now that the aim is conceptually clear, we will perform the algebra and obtain the expression for $|\phi_0\rangle$. We have a basis $\{|i\rangle\}$ in A and $\{|j\rangle\}$ in B to represent $|\phi_0\rangle$. Note that these bases are not necessarily complete. The only requirement is that the space contains $|\phi_0\rangle$,

$$|\phi_0\rangle = \sum_{ij} \phi_{ij} |i\rangle |j\rangle.$$

We want to select the m most relevant basis states $\{|\alpha\rangle\}_{\alpha=1}^m$ from part A . They are contained in the basis $\{|i\rangle\}$ and orthonormal, thus

$$|\alpha\rangle = \sum_i u_i^\alpha |i\rangle, \quad \langle\alpha|\alpha'\rangle = \sum_i u_i^{\alpha*} u_i^{\alpha'} = \delta_{\alpha,\alpha'}. \quad (2.2.1)$$

The best approximation $|\bar{\phi}_0\rangle$ can be expressed in these states,

$$|\bar{\phi}_0\rangle = \sum_{\alpha j} \bar{\phi}_{\alpha j} |\alpha\rangle |j\rangle$$

and the truncation error P , which we want to minimise, is a function of all these parameters,

$$P = \left| |\phi_0\rangle - |\bar{\phi}_0\rangle \right|^2 = \sum_{ij} \left(\phi_{ij} - \sum_{\alpha} \bar{\phi}_{\alpha j} u_i^{\alpha} \right)^2. \quad (2.2.2)$$

The truncation error has to be minimised over the parameters, whilst the orthonormality condition (2.2.1) is fulfilled. Lagrange multipliers $\mu_{\alpha\alpha'}$ are introduced for this purpose. The optimum satisfies

$$\frac{\partial P}{\partial u_i^{\alpha}} = \frac{\partial P}{\partial \bar{\phi}_{\alpha j}} = \frac{\partial P}{\partial \mu_{\alpha\alpha'}} = 0.$$

We introduce the density matrix $\rho_{ii'}$ of A ,

$$\rho_{ii'} = \sum_j \phi_{ij}^* \phi_{i'j}.$$

After some elementary algebra the prefactors $\tilde{\phi}_{\alpha j}$ and the Lagrange multipliers $\mu_{\alpha\alpha'}$ can be obtained,

$$\tilde{\phi}_{\alpha j} = \sum_i \phi_{ij} u_i^\alpha, \quad \mu_{\alpha\alpha'} = 0.$$

The remaining equations read

$$\sum_{i'} \rho_{ii'} u_i^\alpha - \sum_{i''\alpha'} u_i^{\alpha'} u_{i''}^{\alpha''} \rho_{i''i''\alpha''} u_i^\alpha = 0.$$

This equation becomes more transparent when we switch to vector notation,

$$\left[1 - \sum_{\alpha'} \mathbf{u}^{\alpha'} (\mathbf{u}^{\alpha'})^\dagger \right] \cdot \vec{\rho} \cdot \mathbf{u}^\alpha = 0.$$

This equation can be interpreted as a projector acting on the vector $\vec{\rho} \cdot \mathbf{u}^\alpha$. This removes all components of the vector along one of the vectors $\mathbf{u}^{\alpha''}$ as

$$\left[1 - \sum_{\alpha'} \mathbf{u}^{\alpha'} (\mathbf{u}^{\alpha'})^\dagger \right] \cdot \mathbf{u}^{\alpha''} = 0.$$

The basis spanned by $\{\mathbf{u}^\alpha\}$ has to contain all vectors $\left\{ \vec{\rho} \cdot \mathbf{u}^\alpha \right\}$. A set of eigenvectors of $\vec{\rho}$ clearly satisfies this condition. Set $\{\mathbf{u}^\alpha\}$ to be eigenvectors of $\vec{\rho}$ with eigenvalues λ_α so $\vec{\rho} \cdot \mathbf{u}^\alpha = \lambda_\alpha \mathbf{u}^\alpha$. We know that

$$\lambda_\alpha = \mathbf{u}^{\alpha\dagger} \cdot \vec{\rho} \cdot \mathbf{u}^\alpha = \sum_{ii'} u_i^{\alpha\dagger} \phi_{i'j}^* \phi_{ij} u_i^\alpha = \sum_j \left| \sum_i \phi_{ij} u_i^\alpha \right|^2 \geq 0.$$

The complete set of eigenvectors \mathbf{u}^α is orthonormal, so

$$\begin{aligned} \sum_\alpha \lambda_\alpha &= \sum_{ii'j\alpha} u_i^{\alpha\dagger} \phi_{i'j}^* \phi_{ij} u_i^\alpha = \sum_{ii'j} \phi_{i'j}^* \phi_{ij} \delta_{ii'} \\ &= \sum_i \rho_{ii} = \sum_{ij} \phi_{ij}^2 = 1. \end{aligned} \quad (2.2.3)$$

To decide which eigenvectors to select, we note that if m vectors are selected with eigenvalues λ_α , then

$$P = 1 - \sum_{\alpha=1}^m \lambda_\alpha. \quad (2.2.4)$$

This relation can be derived by inserting u_i^α and $\tilde{\phi}_{\alpha j}$ in the definition of the truncation error (2.2.2).

Given (2.2.4) it is immediately evident that the eigenvectors \mathbf{u}^α of $\vec{\rho}$ corresponding to the m largest eigenvalues λ_α have to be selected to build the basis $(|\alpha\rangle)_{\alpha=1}^m$.

It is worth to continue these algebraic manipulations a bit further and show how the optimal basis in part A is related to the optimal basis in part B . This can be derived step by step. For instance White [51] came to similar conclusions when investigating the consequences of a singular value decomposition. Here we simply present the result and discuss its consequences.

The relevant bases states $\{|\tilde{\alpha}\rangle_{\alpha=1}^m\}$ in B are given by

$$|\tilde{\alpha}\rangle = \sum_j v_j^\alpha |j\rangle,$$

where the vector \mathbf{v}^α is related to the vector \mathbf{u}^α through the relations

$$v_j^\alpha = \frac{1}{\sqrt{\lambda_\alpha}} \sum_i \phi_{ij}^* u_i^{\alpha*} \iff u_i^\alpha = \frac{1}{\sqrt{\lambda_\alpha}} \sum_j \phi_{ij} v_j^\alpha.$$

These basis states are orthonormal and they are indeed the largest eigenvectors of the density matrix $\xi_{jj'} = \sum_i \phi_{ij}^* \phi_{ij'}$ as can be seen by insertion;

$$\sum_{i,i'} \xi_{jj'} v_{j'}^\alpha = \frac{1}{\sqrt{\lambda_\alpha}} \sum_{i,i'} \phi_{ij}^* \phi_{ij'} \phi_{i'j'}^* u_{i'}^{\alpha*} = \sqrt{\lambda_\alpha} \sum_i \phi_{ij}^* u_i^{\alpha*} = \lambda_\alpha v_j^\alpha.$$

The ground state obtains a very elegant form in these bases,

$$|\phi_0\rangle = \sum_{ij} \phi_{ij} |i\rangle |j\rangle = \sum_{\alpha=1}^{\bar{m}} \sqrt{\lambda_\alpha} |\alpha\rangle |\tilde{\alpha}\rangle. \quad (2.2.5)$$

To every basis state $|\alpha\rangle$ in part A there corresponds exactly one $|\tilde{\alpha}\rangle$ in part B . The set size \bar{m} is the minimal number of states available in either part A or B . This equation (2.2.5) makes (2.2.4) trivial; the approximation $|\phi_0\rangle$ is simply be given by $|\phi_0\rangle = \sum_{\alpha=1}^{\bar{m}} \sqrt{\lambda_\alpha} |\alpha\rangle |\tilde{\alpha}\rangle$.

Let us elaborate on the equation (2.2.5), as there are a few important consequences of it. If there are as many states in B as we wish to select in A , two further assessments can be made.

First, the truncation error vanishes, $P = 0$; there is no approximation made in transforming $|\phi_0\rangle$ to $|\tilde{\phi}_0\rangle$, $|\tilde{\phi}_0\rangle = |\phi_0\rangle$. All properties of the wave function in the truncated basis are identical to those in the full basis.

Second, if to every element of the basis in B a set of quantum numbers can be assigned, then the distribution of the quantum numbers in part A , contained in the set $\{|\alpha\rangle\}$, is fixed. Every element has the correct quantum numbers to pair up with the quantum numbers of his partner in B to form the required quantum numbers of the wave function $|\phi_0\rangle$.

In the past few paragraphs we developed a method to distinguish important states in a part of the system by the density matrix. This selection criterion can be generalised to incorporate several wave functions $|\phi_\beta\rangle$. This is not a hypothetical situation since we will actually target several states in chapter 4. A weight w_β is introduced to differentiate these states $|\phi_\beta\rangle$ in importance. We now minimise

$$P = \sum_\beta w_\beta \left| |\phi_\beta\rangle - |\tilde{\phi}_\beta\rangle \right|^2.$$

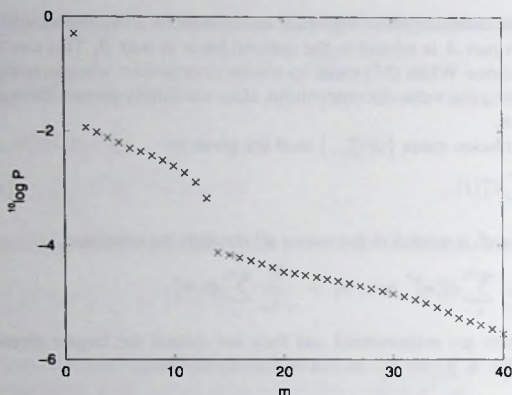


Figure 2-2. The truncation error P as function of the number of states kept m . The system is the ITF with periodic boundaries in both directions and $L \times W = 6 \times 3$. Part A contains the left $3 \times 3 = 9$ sites. $H = 3.0$.

The underlying framework of minimising P remains linear algebra and therefore the density matrix becomes the linear superposition of density matrices for each β ;

$$\rho_{ii'} = \sum_{\beta} w_{\beta} \rho_{ii'}^{\beta}.$$

An approximation scheme based on the density matrix would be useless if this truncated basis $\{|\alpha\rangle\}_{\alpha=1}^m$ does not represent $|\phi_0\rangle$ properly. Clearly the indicator to study is the truncation error P . Figure (2-2) shows that the density matrix can indeed be an excellent selection criterion as the truncation error P falls off exponentially with the number of states kept m . In this case only $m = 13$ states need to be kept of the $2^9 = 512$ to obtain an accuracy of $P \sim 10^{-4}$ in the wave function.

In the following procedure we will make approximations to the ground state and select the optimal bases to represent them. As these approximations are not identical to the ground state, some caution is needed in using the truncation error P as a measure of the accuracy; As stated before, the truncation error will vanish, $P = 0$, if the environment contains as many states as we want to select. This does *not* mean that $|\tilde{\phi}_0\rangle$ is a perfect representation to the ground state. Instead it means that $|\tilde{\phi}_0\rangle = |\phi_0\rangle$.

2.3 Geometry and symmetries of the ITF

As a last stop before commencing the description of procedures to implement the density matrix principle, we have to define the system geometry and investigate the consequences

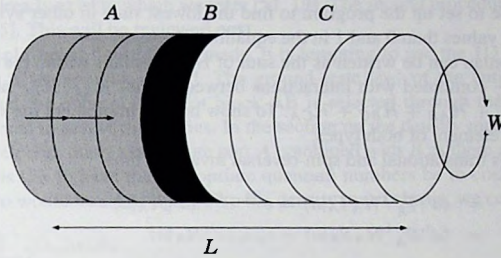


Figure 2-1. The systems we consider are of dimensions $L \times W$. The system contains three parts: a left-hand part A (shaded), an intermediate band B (black) and a right-hand part C (white). At every single loop part A and B are contracted.

on the symmetries of the ITF. As is depicted in figure 2-3 we consider systems of sizes $L \times W$. The length L is in general larger than the width W . The system is periodic in the width direction and open in the length direction. It will be split in a left-hand part A and a right-hand part C, both containing m states. A intermediate band B, containing the complete basis of 2^W states, separates them.

The Hamiltonian of such a system contains many symmetries that we can incorporate in our calculation. The general form of the included symmetry operators is that they are the direct product of three components. Each component acts on one part of the system only. For example, consider the translation operator T in the width-direction. This operator is the direct product of three translations in the individual parts; $T = T_A T_B T_C$. The same holds for the reflection R in the same direction, $R = R_A R_B R_C$, and the spin-reversal operator $S = \exp(i\pi \sum_{i,j} S_{i,j}^z + LW/2) = S_A S_B S_C$.

The ground state $|\psi_0\rangle$ of the system is translational, reflection and spin-reversal invariant; $T|\psi_0\rangle = R|\psi_0\rangle = S|\psi_0\rangle = |\psi_0\rangle$. For systems of infinite size in the classical ordered region ($L, W \rightarrow \infty$ and $H \ll 1$), it will become degenerate with a state that is spin-reversal anti-symmetric. In order to take advantage of the symmetries, the bases of part A, B and C are chosen to be eigenvectors of the symmetry operators T and S . R is used later on. So if $\{|a\rangle\}$, $\{|b\rangle\}$, $\{|c\rangle\}$ are the bases of the individual parts then

$$T_A|a\rangle = e^{ik_a}|a\rangle, \quad S_A|a\rangle = s_a|a\rangle. \quad (2.3.1)$$

Similar relations hold for the other two sets. Thus

$$|\phi_0\rangle = \sum_{abc} \phi_{abc}|a\rangle|b\rangle|c\rangle$$

and application of the symmetry operations together with (2.3.1) yields:

$$k_a + k_b + k_c = 0 \bmod 2\pi, \quad s_a s_b s_c = 1.$$

It is also possible to set up the program to find the lowest state in other symmetry classes by forcing other values than 0 and 1 in the equations above.

The Hamiltonian can be written as the sum of Hamiltonians within the separate parts: \mathcal{H}_A , \mathcal{H}_B and \mathcal{H}_C combined with interactions between parts: \mathcal{H}_{AB} , \mathcal{H}_{BC} and \mathcal{H}_{CA} ; $\mathcal{H} = \mathcal{H}_A + \mathcal{H}_B + \mathcal{H}_C + \mathcal{H}_{AB} + \mathcal{H}_{BC} + \mathcal{H}_{CA}$. To show how to implement the symmetries, we will discuss one element of both types.

First \mathcal{H}_A : it is translational and spin-reversal invariant, thus

$$\begin{aligned}\langle a' | \mathcal{H}_A | a \rangle &= \langle a' | \mathcal{T}_A^{-1} \mathcal{H}_A \mathcal{T}_A | a \rangle = e^{i(k_a - k_{a'})} \langle a' | \mathcal{H}_A | a \rangle \\ &= \langle a' | \mathcal{S}_A^{-1} \mathcal{H}_A \mathcal{S}_A | a \rangle = s_{a'} s_a \langle a' | \mathcal{H}_A | a \rangle\end{aligned}$$

These relations lead to the appearance of delta-functions,

$$\langle a' | \mathcal{H}_A | a \rangle = \langle a' | \mathcal{H}_A | a \rangle \delta_{s_{a'}, s_a} \delta_{k_{a'}, k_a}.$$

It only contains elements within symmetry classes, as one would expect.

Second \mathcal{H}_{AB} : once again, it is translational and spin-reversal invariant. Moreover it can be written as

$$\begin{aligned}\mathcal{H}_{AB} &= -4 \sum_{n=1}^W \mathcal{S}_{l,n}^x \mathcal{S}_{l+1,n}^x \\ &= -4 \sum_{n=1}^W (\mathcal{T}_A \mathcal{T}_B)^{-n+1} \mathcal{S}_{l,1}^x \mathcal{S}_{l+1,1}^x (\mathcal{T}_A \mathcal{T}_B)^{n-1}\end{aligned}\quad (2.3.2)$$

where l is the length of part A . $\mathcal{S}_{i,j}^x$ flips a spin, so $\mathcal{S}_{i,j}^x \mathcal{S} + \mathcal{S} \mathcal{S}_{i,j}^x = 0$. Inserting this and (2.3.1) in (2.3.2) gives

$$\begin{aligned}\langle a' | \langle b' | \mathcal{H}_{AB} | a \rangle | b \rangle &= -4W \langle a' | \mathcal{S}_{l,1}^x | a \rangle \langle b' | \mathcal{S}_{l+1,1}^x | b \rangle \cdot \\ &\quad \delta_{k_{a'} + k_{b'}, k_a + k_b} \cdot \delta_{s_{a'}, -s_a} \delta_{s_{b'}, -s_b}.\end{aligned}$$

This substantially reduces the computational effort. Finally: the reflection operator \mathcal{R} is used to make matrix elements like $\langle a' | \mathcal{S}_{l,1}^x | a \rangle$ real. In fact we could have used this last symmetry \mathcal{R} more, but it only reduces the effort by a factor of 4 while making the program far more complex.

2.4 Procedures

In the section on the density matrix, a selection criterion was developed. Now this criterion will be incorporated in a procedure. We have employed two distinct procedures: the first one was originally proposed by White [51], and trivially extended to two dimensions by Liang and Pang [28]. In this scheme, part A , figure 2-1, is enlarged iteratively at the expense of part B . Each step one site is moved from part B to part A . The basis on part A will thus incorporate more and more sites, while the total system size remains the same. Excellent

introductions already exist to which we refer [51, 19]. The second procedure we introduced ourselves in [15]. This will be reviewed next.

When the split-up of figure 2-3 is made, it is tempting to use the 1D DMRG method directly: a site is replaced by a band. The ground state $|\phi_0\rangle$ of the entire system ABC is calculated and the optimal basis for block AB is selected through the density matrix. However, one runs in severe difficulties. In the section on the density matrix it was shown that when we select as many states from part A combined with B as there are in part C, the outgoing basis has to have the appropriate quantum numbers be to combined with part C. So if we also would transform part C in the density matrix basis, we can write

$$|\phi_0\rangle = \sum_{\alpha} \sqrt{\lambda_{\alpha}} |\alpha\rangle |\tilde{\alpha}\rangle.$$

We know that $T|\phi_0\rangle = S|\phi_0\rangle = |\phi_0\rangle$, thus

$$T|\alpha\rangle = e^{ik_{\alpha}} |\tilde{\alpha}\rangle, \quad S_C|\tilde{\alpha}\rangle = s_{\tilde{\alpha}} |\tilde{\alpha}\rangle.$$

That immediately dictate the quantum number of the newly built $|\alpha\rangle$:

$$T_A T_B |\alpha\rangle = e^{-ik_{\alpha}} |\tilde{\alpha}\rangle, \quad S_A S_B |\tilde{\alpha}\rangle = s_{\tilde{\alpha}} |\tilde{\alpha}\rangle.$$

Thus $s_{\alpha} = s_{\tilde{\alpha}}$ and $k_{\alpha} = -k_{\tilde{\alpha}}$. The distribution over the symmetry classes in part C forces the selected states in block AB to be in “conjugate”-classes. To overcome this problem, we need to increase the number of states in part C. In that case we can really make a selection and it allows us to change between symmetry classes.

In the 1D procedure the solution is to add one extra site to the environment. The number of states in the environment is then doubled. In our set-up this would correspond to adding an extra band between B and C. This is computational far too expensive.

We now introduce variants on White’s infinite-size and finite-size algorithms [51] that increase the number of states in the part C.

First we consider our infinite size approach. We only have to describe one step in the process as it is an inductive method. We have a basis of m states for a system of length l . We then proceed as follows:

- We construct the combined system as depicted in figure 2-4-a by taking this basis in part A and C together with the complete basis in the intermediate band B. ($L = 2l + 1$)
- We calculate the ground state $|\phi_0\rangle$ and obtain m basis states for a system of length $l + 1$ by orthonormalising $\{|\beta_c\rangle\}$,

$$|\beta_c\rangle = \sum_{a,b} \phi_{abc} |a\rangle |b\rangle,$$

and span the space we previously denoted by $\{|\alpha\rangle\}_{\alpha=1}^m$.

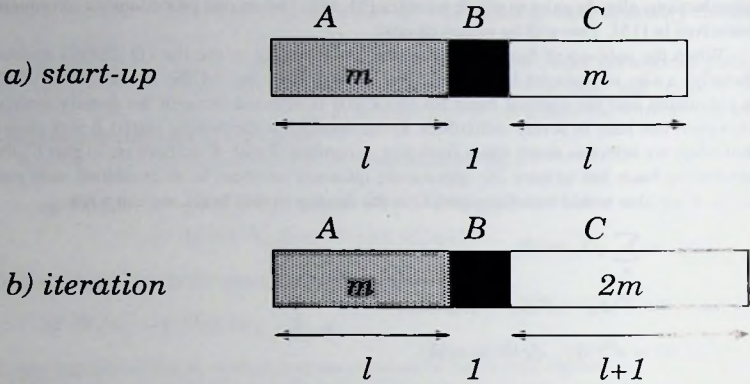


Figure 2-4. A inductive step in the infinite-size procedure consists of a start-up to obtain an initial approximation for states in a system of length $l + 1$ and iterative calculations to make the basis converge. The numbers in the rectangle are the number of states in the parts. The intermediate band B always contains the complete basis of 2^w states.

- Suppose that block AB has f symmetry classes. To every symmetry class we add m/f basis states constructed randomly from the $m2^w$ states in A and B . We end up with $m + f \cdot m/f = 2m$ basis states for a system of length $l + 1$.
- In part A we now take the m basis states for a system of length l and in part C we take the newly constructed $2m$ states for length $l + 1$. ($L = 2l + 2$) This yields the configuration in figure 2-4-b.
- We calculate the ground state $|\phi_0\rangle$ and obtain $2m$ basis states for length $l + 1$ by orthonormalising $\{|\beta_i\rangle\}$. We replace the basis of part C by this basis and repeat this step a couple of times (~ 3).
- We select from the $2m$ basis states for length $l + 1$ m states on basis of the density matrix.

Now we have returned to the original situation with the exception that l has increased by one. The new ingredient is thus to add m random states to the basis and iterate until the result has converged.

In the same line our finite size approach lies. Suppose we have basis sets of m states for lengths $l, L - l - 1$ and $L - l - 2$, where L is now fixed and independent of l . The iteration step consists of the following actions:

- We take the basis for l in part A , the basis for $L - l - 1$ in part C and the complete basis of the band in part B . See figure 2-5-a.
- We calculate the ground state $|\phi_0\rangle$ and obtain a basis for length $l + 1$ by orthonormalising $\{|\beta_c\rangle\}$.
- In the same way as in the infinite-size algorithm we add m randomly chosen states to this basis.
- In part C we take the $2m$ basis states for length $l + 1$ and in part A the m states for length $L - l - 2$. This is depicted in the first of the two pictures in figure 2-5-b.
- We calculate the ground state $|\phi_0\rangle$ and obtain $2m$ basis states for $L - l - 1$.
- In part C we take the $2m$ basis states for length $L - l - 1$ and in part A the m states for length l ; see the second picture in figure 2-5-b.
- We calculate the ground state $|\phi_0\rangle$ and obtain $2m$ basis states for $l + 1$. These last three steps are repeated a couple of times (~ 3)
- We select from the $2m$ basis states for length $l + 1$ m states on basis of the density matrix.

Once again we have returned to our starting position while increasing the length l by one. By sweeping through the system we can therefore systematically improve the basis. This method converges at a similar speed as the 1D approach; after 3 sweeps through the system the final result is achieved.

The approximation scheme to the ground state is both variational and systematic. The energy of each state in the selected subspace is higher than the one of the ground state. As this includes the state we select by minimisation of the energy, our estimate to the ground state energy is variational. In section (4.2) we will meet other examples of variational principles that can be used within the DMRG scheme.

The systematics come in from the iterations. When a state is selected, it is truncated and transformed along with the basis. The next iteration it is used as a starting point for the minimisation routine. If the density matrix eigenvalues drop off fast enough and the truncation thus does not severely alter the state, the energy of the starting point will be almost the same as the outcome of the last iteration and the during the minimisation this estimate can improve further.

After several sweeps through the system, the energy will start to oscillate. This effect is small, but the cause of it gives ground for further improvement. Suppose we have found a state $|\phi_0\rangle$ at the previous iteration. This state is truncated to $|\tilde{\phi}_0\rangle$. In the truncation a part of the state is lost, so $|\tilde{\phi}_0\rangle \neq |\phi_0\rangle$. The truncated space of $|\tilde{\phi}_0\rangle$ lies in the subspace of $|\phi_0\rangle$ though. We know that $|\phi_0\rangle$ corresponds to the lowest energy in that subspace, thus

$$\frac{\langle \phi_0 | \mathcal{H} | \phi_0 \rangle}{\langle \phi_0 | \phi_0 \rangle} \leq \frac{\langle \tilde{\phi}_0 | \mathcal{H} | \tilde{\phi}_0 \rangle}{\langle \tilde{\phi}_0 | \tilde{\phi}_0 \rangle}.$$

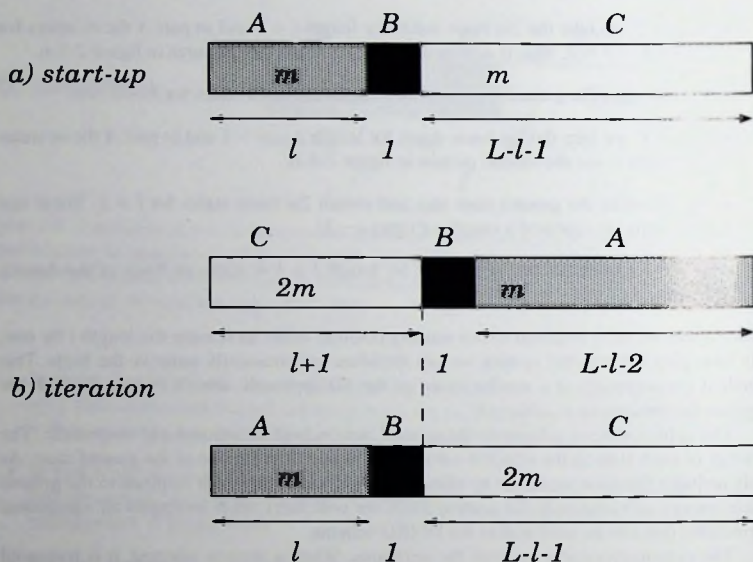


Figure 2-5. A inductive step in the finite-size procedure also consists of a start-up to obtain an initial approximation for states in a system of length $l + 1$. Afterwards we move back and forth between lengths l and $l + 1$ to make this converge.

$|\bar{\phi}_0\rangle$ is transformed and thereby embedded in an other subspace. It is used as a starting point for the next minimisation. The next estimate $|\bar{\phi}_0\rangle$ will thus have a lower energy,

$$\frac{\langle \bar{\phi}_0 | \mathcal{H} | \bar{\phi}_0 \rangle}{\langle \bar{\phi}_0 | \bar{\phi}_0 \rangle} \geq \frac{\langle \bar{\phi}_0 | \mathcal{H} | \bar{\phi}_0 \rangle}{\langle \bar{\phi}_0 | \bar{\phi}_0 \rangle}.$$

No strict statement can be made on the relation between the energies of $|\phi_0\rangle$ and $|\bar{\phi}_0\rangle$. The energy does not need to decrease monotonically and will start to oscillate.

Once this happens, we can assume that the basis states we use, lie in the most relevant symmetry classes and it is no longer necessary to increase at every location in the system the number of states in part C from m to $2m$. Leaving out the iterations to increase the number of states in part C, the previous estimate $|\phi_0\rangle$ can still be represented exactly after the basis truncation, $|\bar{\phi}_0\rangle = |\phi_0\rangle$. This is explained in the paragraph after equation (2.2.5). The ground state $|\bar{\phi}_0\rangle$ of the next step satisfies

$$\frac{\langle \bar{\phi}_0 | \mathcal{H} | \bar{\phi}_0 \rangle}{\langle \bar{\phi}_0 | \bar{\phi}_0 \rangle} = \frac{\langle \bar{\phi}_0 | \mathcal{H} | \bar{\phi}_0 \rangle}{\langle \bar{\phi}_0 | \bar{\phi}_0 \rangle} \geq \frac{\langle \bar{\phi}_0 | \mathcal{H} | \bar{\phi}_0 \rangle}{\langle \bar{\phi}_0 | \bar{\phi}_0 \rangle}.$$

The energy will now decrease monotonically.

2.5 Connection with the Renormalisation Group

The name DMRG has led many people to believe that it is another implementation of Wilson's renormalisation group. This is incorrect in at least two respects. First, this method does not contain a semigroup operation; where in the renormalisation group the Hamiltonian is mapped onto itself with different parameters, here we change —read truncate—the Hamiltonian all together. The name group is unfortunate and misleading, but it is well established and to avoid further confusion, we will stick to the name DMRG.

The second distinction lies in the fundamental difference of basis selection. The DMRG first calculates the approximate ground state of the entire system and afterwards makes a selection via the density matrix of this state. The renormalisation group, on the other hand, does not consider the properties of the entire system. The basis states are solely selected on merit of the energy within their own part of the system.

The well-known example [52, 33] of a particle in a box with impenetrable walls illustrates this selection criterion clearly. By its graphical simplicity figure 2-6 demonstrates that in the DMRG one basis state suffices whereas the renormalisation group needs many to represent the wave function properly.

2.6 Performance

In this section a discussion is given on the accuracy that can be achieved by the DMRG procedures. First we consider issues that affect both methods, afterwards a comparison between the two methods is made.

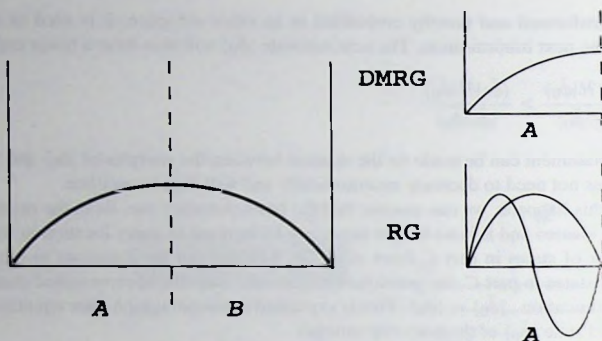


Figure 2-6. On the left the wave function of a particle in a box is depicted. At current accuracy this version of the DMRG does not exist, so one should consider the location in the box a very fine grid of discrete points. On the right we see the selections of the DMRG, one state suffices, and of the ordinary renormalisation group (RG) where many states are needed.

2.6.1 General limitations.

The most striking limitation is that only systems of small width can be handled. As the width W increases, the number of states m kept in the procedure has to increase exponentially to maintain the accuracy [28]. In figure 2-7 this is exemplified for the ITF. To get a flavour of the background to this behaviour, we will discuss a pathological example where this statement can be proven exactly.

Consider a system containing a set of chains as depicted in figure 2-8. For each chain a DMRG calculation can be performed and it is found that m_0 states are required to obtain a given accuracy. To achieve the same accuracy for this system of width $W = 4$, for each chain m_0 states have to be preserved as there is no interaction between the chains. The basis of the entire part A is a product of bases for the individual chain pieces. Therefore there are $m = m_0^W$ states necessary for the same accuracy; a clear proof of the exponential growth of the number of states m with increasing width W .

In the study of the ITF we are fortunate enough to go somewhat further than this rough-and-ready argument. Far from the phase transition ($H \ll 1$ or $H \gg 1$) a connection can be made with perturbation theory.

Consider the quantum disordered phase on a periodic system. Split the Hamiltonian into an unperturbed part $H_0 = 2H \sum_{i,j} S_{i,j}^z$ and a perturbation $V = -4 \sum_{i,j} S_{i,j}^x (S_{i+1,j}^x + S_{i,j+1}^x)$. We split the periodic, rectangular system of size $L \times W$ again in two parts; A and B of sizes $l \times W$ and $(L-l) \times W$ where l is an arbitrary length smaller than L . They both contain $2W$ spins that border the other part. The unperturbed ground state $|0\rangle$ has all spins pointing down in the S^z -direction. It is the direct product of two equivalent states restricted

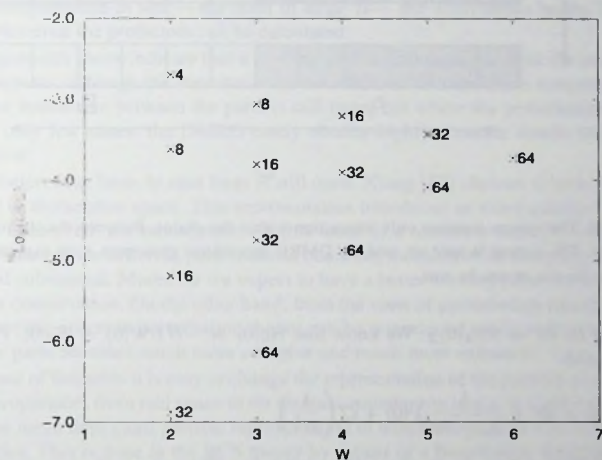


Figure 2-7. The accuracy of the DMRG method for given number of states m (numbers in graph) as function of the width W . $H = 3$ and $L = 20$. The system is periodic in both directions. The reference value is taken from a DMRG calculation with $m = 128$.

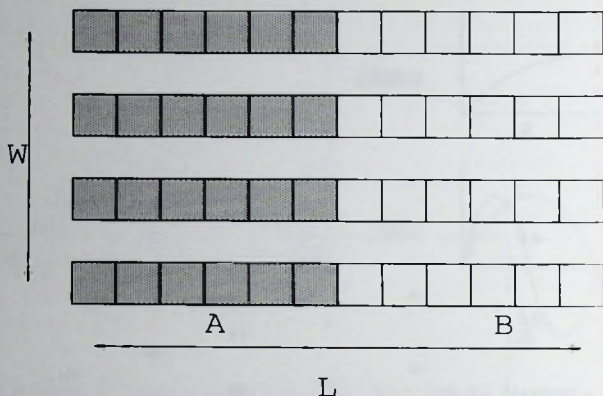


Figure 2-8. The system contains only interaction within the chains. Between the chains no interaction exists. The system is split up, and the DMRG procedures grow part A on expense of part B. Either site by site or row by row.

to A and B; $|0\rangle = |0\rangle_A |0\rangle_B$. We know that $\mathcal{H}_0|0\rangle = -HLW|0\rangle = E_0|0\rangle$. Perturbation theory yields

$$|\phi_0\rangle = |0\rangle + \frac{1}{E_0 - \mathcal{H}_0} \mathcal{V}|0\rangle + \mathcal{O}\left(\frac{1}{H^2}\right) \quad (2.6.1)$$

The perturbation flips a pair of neighbouring spins. This pair can be in a single part or it can cross the border between both parts. In the latter case the spins are adjacent across the boundary between part A and B. Define $\{|a\rangle_A\}$ to be the set of states with the flipped pair in part A. Analogous for $\{|b\rangle_B\}$. Moreover let $\{|n\rangle_A\}$ be the set with one spin flipped on the n th boundary site with B and define in an equivalent manner $\{|n\rangle_B\}$. The perturbation expansion can now be rewritten

$$\begin{aligned} |\phi_0\rangle &= |0\rangle_A |0\rangle_B + \frac{1}{2H} \left(\sum_a |a\rangle_A |0\rangle_B + \sum_b |0\rangle_A |b\rangle_B + \sum_n |n\rangle_A |n\rangle_B \right) \\ &\quad + \mathcal{O}\left(\frac{1}{H^2}\right) \\ &= \left(|0\rangle_A + \frac{1}{2H} \sum_a |a\rangle_A \right) \left(|0\rangle_B + \frac{1}{2H} \sum_b |b\rangle_B \right) + \frac{1}{2H} \sum_n |n\rangle_A |n\rangle_B \\ &\quad + \mathcal{O}\left(\frac{1}{H^2}\right). \end{aligned} \quad (2.6.2)$$

As $H \gg 1$, it is necessary to reproduce *all* these terms for an accuracy which is equivalent to the first order perturbation theory. The minimal number of states needed in part A is therefore 1 for the first term in (2.6.2) plus $2W$ for all the boundary terms. We have confirmed this prediction explicitly in both the small and large H limit ($H = 1/50, 50$).

The same line of reasoning also holds for the second and higher order perturbation terms. We expect for an error comparable to the n th order perturbation theory that $m \sim W^n$, $\delta E \sim (1/H)^n$. This is always an upper bound for number of states m needed, $m < W^n$ for a given accuracy $\delta E \sim (1/H)^n$. Only when the different orders in perturbation theory become distinguishable in size —the limit of large H — the equivalence holds. Through combinatorics even the prefactors can be calculated.

Both arguments above indicate that it is of the utmost importance to limit the interaction between the parts, although the statements are not identical. If there exists a representation in which the interaction between the parts is still large, but where the perturbation expansion needs only few states, the DMRG easily obtains highly accurate results within that representation.

The question what basis to start from is still open. Xiang [57] chooses to treat the Hubbard model in momentum space. This representation introduces an extra quantum number that can be conserved: the momentum. As this leads to a relatively strong restriction on those basis states of the different parts that can combine, the number of states kept m could be increased substantial. Moreover we expect to have a better starting point for the ground state by this conservation. On the other hand, from the view of perturbation theory it is unclear whether the orders in perturbation theory can be reproduced easily as the interaction between the parts becomes much more complex and much more extended.

In the case of fermions it is easy to change the representation of the particle creation and annihilation operators from real space to for instance momentum space. It is also possible to switch to the mean field quasi particle representation in which the ground state contains no quasi particles. This is done in the BCS theory by means of a Bogoliubov transformation. For a DMRG calculation such a representation may also be not ideal despite the fact that the mean field ground state can be represented by exactly one basis vector (with no quasi particles present). It could be a source of bias in the final result.

Other attempts have been made to avoid the issue of limited width all together by smoothing the boundary conditions and thereby reducing the boundary effects [49].

Another restriction is related to phase transitions. A clear indication of the vicinity of a phase transition is divergence of the correlation length. At the phase transition algebraic behaviour of the correlation functions is expected. This is conflicting with the manner in which the ground state is built by DMRG. Successive basis rotations and truncations where at every step a new site is included in the basis clearly favour exponentially decaying correlation functions [35]. For the ITF the accuracy of the DMRG at the phase transition indeed decreases although it remains unclear whether this is a general feature of phase transitions. Figure 2-9 illustrates this.

Several basis rotations and truncations applied to operators cause them to deteriorate. For the intermediate band or site the basis is complete and the representation of the operators on these sites is perfect, but for sites further away from the part boundaries, some basis

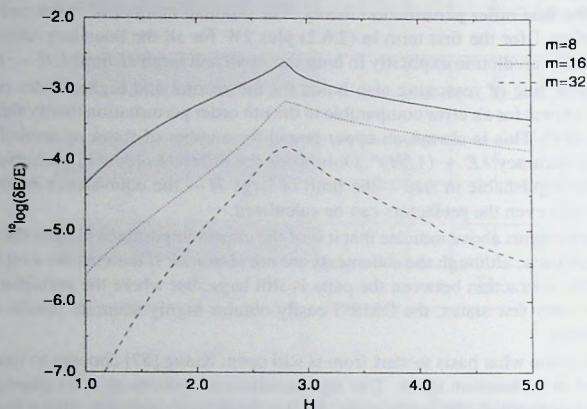


Figure 2-9. The accuracy of the DMRG method for different number of states m (numbers in graph) as function of the field H . The system is periodic in both directions with dimensions $W = 4$ and $L = 20$. The reference value is taken from a DMRG calculation with $m = 64$. The critical field of the two-dimensional system is $H_c = 3.044$

truncation have been applied and the representation of the operators has lost the connection with the states truncated from the basis. A consequence of this is that the correlation functions for sites that are simultaneously or successively included in a part by the procedure are of higher quality than those between sites that lie further apart.

2.6.2 Comparison of both methods.

In section 2.4 a version of the DMRG was introduced that added bands to a part. White's original proposal was to add sites to a part. These two procedures, site and band, can be compared on two grounds:

- Computational effort with given accuracy.
- Flexibility of the procedure.

Let us address these criteria in the same order.

A straightforward comparison of the two computer programs favours the site method heavily. Unfortunately this says more about the software than about the quality of the

method. A fair approach contains two steps: first the accuracy as function of the number of states kept m is related. Afterwards the computational effort of both procedures as function of the number of states m is estimated. We have done both for the ITF.

Figure 2-10 depicts the first step. The band method clearly needs fewer states for the same accuracy.

The bottle neck in the computational effort is finding the ground state $|\phi_0\rangle$ in a given subspace. This is done by applying the Hamiltonian in the order of 5 times to the wave vector. In the site procedure this costs $m^3 \cdot W/2^2$ operators per projection. The factor $1/2^2$ follows from: conservation of the spin reversal operator S . To sweep through the system there are thus $t_{\text{site}} = 5 \cdot m^3 \cdot L \cdot W^2/2^2$ operations needed. The band method has a far larger space in part B but it is possible to use translational invariance in the width direction and fewer steps have to be taken to sweep through the system. Per step it costs $m^3 \cdot 2^W/W$ operations ($W \geq 2^W$). With the moving back and forward at one location (3 successive diagonalizations), we get $t_{\text{band}} = 3 \cdot 5 \cdot m^3 \cdot L \cdot 2^W/W$ operations for one complete sweep. Up to $W \approx 3$ these two estimates are similar,

$$\frac{t_{\text{site}}}{t_{\text{band}}} = \frac{5m^3 L W^2/2^2}{15m^3 L 2^W/W} = \frac{1}{3} \frac{W^3}{2^{W+2}},$$

with the band method achieving higher accuracy with the same number of states m . After that the site method clearly becomes faster.

To summarise the comparison of the computational performance: as long as the systems do not become too wide ($W \leq 8$), both methods are comparable in efficiency. The band procedure is slightly preferential as it could be faster and the ground state is more symmetric. The difference in calculation time we observed is mainly the result of the quality of the software and specifically the use of the BLAS [3] routines. The difference in calculative performance is not conclusive.

Next we compare the flexibility. The computational performance is in practical situations irrelevant as a large fraction of the effort spent in research is dedicated to probing properties of models by changing parameters and such. This requires a degree of flexibility in the procedure. By this criterion the site procedure is clearly preferential as both the geometry and interactions can easily be changed. The band procedure obtains its better calculative performance from the translation invariance of the ground state. This fixes both the geometry and the interactions to support translational invariance. The only advantage of the band method in the terms of flexibility is that by strictly conserving the translational symmetry, also states with difference momentum can be targeted.

The overall conclusion is that if one wants to test a model the site procedure is preferable, whereas if maximum accuracy is required the band procedure should be used.

2.7 Some considerations on the implementation

Choosing the right software language and tools is very much dependent on both the hardware and software available. As the progress in these is rather swift, remarks in this section will be relatively soon outdated. Still it can be of tremendous use having an idea of what

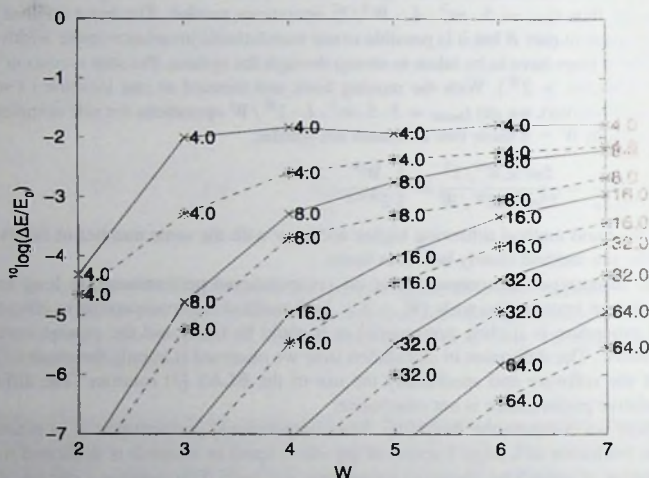


Figure 2-10. The accuracy of the site-procedure (asterisk '*') is compared to that of the band-procedure (cross 'x') for various system widths W and number of states m (numbers in the graph). The transverse field $H = 3$ and the system length $L = 20$. The geometry of a cylinder is used; Periodic boundary conditions in the short width-direction and open ones in the long length-direction.

the implementation could look like. We state our comments going from more conceptual to language specific ones.

In implementing the Hamiltonian, operators of the form $S_1 \cdot S_2$ have to be applied to a wave function $|\phi\rangle$. It is recommended to apply the members of this pair successively, $S_1 \cdot (S_2|\phi\rangle)$, not simultaneously, $(S_1 \cdot S_2)|\phi\rangle$. Algebraically these two multiplications are identical, but computational the second one is far more expensive than the first.

Many sophisticated matrix manipulation libraries exist and these can be used. For that purpose the intermediate sites have to be merged with the larger parts; in the site procedure, the left intermediate site can be merged with the left part and the right intermediate site with the right part. In this fashion we obtain two bases, one for the left part, $\{|i\rangle\}$, and one for the right part, $\{|j\rangle\}$. Now a wave function $|\phi\rangle$ can be expressed by a matrix Φ ,

$$|\phi\rangle = \sum_{i,j} \Phi_{i,j} |i\rangle |j\rangle.$$

The act of this representation touched immediately at another implementation matter; applying operators to this wave function now transforms into matrix multiplications. There are quite a few libraries available that are highly optimised to perform this task of matrix multiplication, most notably BLAS [3].

To end our list of remarks, the programming language that we used is C++. There are two reasons to do this:

- At current, it is one of the most widely used languages. This ensures the availability of tools, libraries and sophisticated compilers.
- C++ allows object oriented programming. This requires a different way of analysing a problem than the well-establish procedural approach, but it makes the code more transparent and reusable. Especially in combination with packages like STL¹ this provides a powerful programming environment.

Naturally C++ is not unique in either of these properties. FORTRAN90 also fits at least the second argument, but is less widely used.

Object oriented code in C++ is slower than FORTRAN or FORTRAN90, but in a DMRG implementation by far the most time is spend on finding the ground state. As this is code-wise only a fraction of the entire program, this can easily be implemented in a procedural fashion using fast libraries (BLAS).

2.8 Results for the ITF

The scaling analysis of the previous chapter is based on DMRG calculations. The ground state of the ITF model lies in the space with spin reversal quantum number $S = 1$. The first excitation appears when one spin is flipped, so $S = -1$ for that state. We calculate in both spaces the ground state energy $E_0^{S=\pm 1}$ and the gap Δ is given by

$$\Delta = E_0^{S=-1} - E_0^{S=1}.$$

¹ standard template library, part of the C++ library

The gap is thus the difference between two large numbers. This causes the relative error to increase by two orders of magnitude and the highest achievable accuracy is needed.

Experimentally it has been observed [54] that the truncation error P becomes proportional to the error in the energy. This is not surprising as the truncation error P is a direct indicator of quality of the basis truncation. The estimate of the energy is improved by extrapolating to zero truncation error, $P = 0$.

As we mentioned earlier in section (2.6.1), the accuracy is highly dependent on the length of the boundary between the different parts. In a periodic system, each part is coupled on both sides to the rest of the system, so then the boundary is twice as long as in an open system. With the accuracy already so much under pressure, we cannot afford to double the length of the boundary.

Unfortunately it is not possible to study system of larger width than $W = 8$ with the DMRG. This means that the DMRG method has strong competition from cluster Monte Carlo algorithms [6]. It has to be stressed though, that in cases where the Monte Carlo methods fail as a consequence of the sign-problem, DMRG can provide an excellent replacement.

3 Spin stiffness and finite-size scaling of the frustrated Heisenberg Model

3.1 Introduction

The interest in the frustrated Heisenberg model arose with the discovery of high T_c -superconductors. The ground state of the undoped compound shows long-range antiferromagnetic order which can be well described by the Heisenberg model. However introduction of a small number of holes destroys the long range order and triggers superconductivity. In a way doping and frustration have similar effects on the long range magnetic order. The underlying similarity is not really understood but efforts are made to connect them, see for instance the book by Auerbach [2]. To improve the understanding of these effects, it is of interest to study a frustrated Heisenberg model.

In more recent years it has become a research topic of its own. It may serve as an example of a system exhibiting a quantum phase transition going from Néel order to collinear order with increasing frustration. Hopes are that new and so far unknown phases will be discovered in the intermediate regime.

A link can be made between this frustrated Heisenberg model and the material CaV_4O_9 . If the spins are positioned on a rectangular lattice with every fifth site unoccupied, the model may describe CaV_4O_9 [47].

Our intention here is to employ the spin stiffness as a means of measuring the order present in the system. In this chapter, the spin stiffness will be calculated in the Schwinger-Boson Mean Field (SBMF) theory [2, 17, 31]. This mean field theory introduces the mean fields in the interactions between spins and allows for the ground state to be rotationally invariant. Afterwards the spin length is no longer conserved to be $\frac{1}{2}$ and we will discuss the consequences in some detail at the end of section 3.4.

The spin stiffness in the SBFM serves as a guideline for the effects of finite-size scaling, which is an indispensable tool for the numerical calculations using the DMRG method. The next chapters contain the numerical parts of our investigations; in chapter 4 the DMRG method is combined with finite-size scaling to obtain the spin stiffness of the two-dimensional system. In chapter 5 the correlation function are studied by a combination of the DMRG and Green Function Monte Carlo simulations.

3.2 The frustrated Heisenberg Model

This model describes interacting quantum spins on distinct lattice sites. The spins \vec{S}_j have length $\frac{1}{2}$. Hence $|\vec{S}_j|^2 = \frac{3}{4}$. The Hamiltonian is given by

$$\mathcal{H} = J_1 \sum_{\langle ij \rangle} \vec{S}_i \cdot \vec{S}_j + J_2 \sum_{[ij]} \vec{S}_i \cdot \vec{S}_j.$$

It incorporates interactions between nearest-neighbour pairs $\langle ij \rangle$ with strength J_1 and next-nearest-neighbour pairs $[ij]$ with strength J_2 . We will focus on a square lattice in two dimensions with $L \times W = N$ sites. At the end of this chapter we will consider systems where $L \neq W$. The next-nearest-neighbouring sites are connected through the diagonals of the lattice. The lattice is bipartite; it can be split into equivalent sublattices A and B. If site j is in sublattice A then all its nearest-neighbours are in sublattice B. The function $(-1)^j$ will therefore be 1 if $j \in A$ and -1 if $j \in B$.

Both J_1 and J_2 are taken to be non-negative. If J_2/J_1 is small the dominating term describes the usual antiferromagnetic interaction and the ground state will be Néel ordered. For instance spin-up on sublattice A and spin-down on sublattice B or $(-1)^j \langle S_j^z \rangle = m$. For the opposite case, J_2/J_1 large, the system decomposes in two Néel ordered sublattices which, however, have the same quantisation axis. This is the so-called collinear ordering. In this ordering alternating strips of up and down-spins will occur. Suppose the strips are oriented along the x -axis, then $(-1)^y \langle S_j^z \rangle = m$, where the j -th spin is on the y -th row.

Clearly these couplings frustrate each other on a square lattice when they are comparable in size. It is beforehand unclear what will happen then. Whether a different phase exists in the region between the Néel ordering and the collinear ordering remains uncertain. In the literature there have been speculations ranging from dimer - to disordered phases [16, 44, 58, 41]. In all of these cases it is conjectured that the intermediate phase has no long-range order. The correlation length thus becomes finite and a gap in the energy spectrum opens up. This energy gap is a good indicator for the existence of an intermediate phase. Unfortunately, it is very hard to achieve high enough accuracy in the numerics as it involves the subtraction of two $\mathcal{O}(N)$ numbers (the ground state energy is subtracted from the energy of the first excitation) to yield a $\mathcal{O}(1)$ number, the gap.

Another indicator for long-range order is the spin stiffness. This quantity potentially allows for higher numerical accuracy. In the current chapter the spin stiffness of both the Néel and the collinear phase will be derived in the Schwinger-boson mean field approximation. Part of the material in the chapter is published in [14].

3.3 The spin stiffness

To investigate the phase diagram, one could look for order parameters. However, if the frustration increases, a new and different ordering might appear with an unknown order parameter. So, many different order parameters would have to be examined. There exists a far more general approach. It is known that when a continuous symmetry is broken, a Goldstone mode appears. This is a 'symmetry-restoring' excitation. For this kind of spin

model, these are called spin waves, as they are wave-like fluctuation in the spin orientations. In [23] it was shown that for both types of order considered here (Néel and collinear) the dispersion relation is linear ($\omega = c|\mathbf{q}|$) for low energies. The velocity c of this mode satisfies

$$c = \sqrt{\frac{\rho_s}{\chi_\perp}}. \quad (3.3.1)$$

Here ρ_s stands for the spin stiffness and χ_\perp is the magnetic susceptibility of the system perpendicular to the orientation of the ordering. A positive spin stiffness ($\rho_s > 0$) is an indication that a broken-symmetry is present, although the actual order parameter might be unknown! Therefore it is an excellent measure of magnetic order that arises from a broken symmetry. For the Heisenberg model an order related to a local organisation of spins in the intermediate range of frustration has been suggested [16, 44, 58, 41]. The global rotational invariance is not broken, therefore the spin stiffness should be zero, $\rho_s = 0$. In short: the spin stiffness is an excellent indicator to distinguish between a broken symmetry ground state (e.g. Néel) and other ground states ($\rho_s = 0$).

3.3.1 Static derivation at zero temperature

Fisher, Barber and Jasnow [18] showed that the spin stiffness ρ_s , that is related to the dynamics of the system, can be obtained by a static twist in the order parameter. They imposed boundary conditions to achieve this twist. Instead of following them in detail, we will directly focus on the order parameter. In [27] this route has also been followed and we could reduce the formula there to zero temperature, but the transition from finite temperature to zero temperature is subtle and we will instead make an explicit derivation of ρ_s . In this way the concepts involved can be made more transparent and subtleties concerning the necessity of periodic boundaries can be addressed more directly. The resulting expression for the stiffness appears in several places in the literature, e.g. [16].

We consider the case of Néel order as an example. Afterwards it will be shown that the expression we found holds in more general cases. Before we start let us mention that a two-dimensional system exhibiting long-range order at zero temperature is not conflicting with the Mermin-Wagner theorem [30]. The theorem only forbids long-range order at finite temperature.

The ground state of an antiferromagnet satisfies

$$\begin{aligned} \langle 0 | \mathcal{H} | 0 \rangle &= E_0, \\ \langle 0 | S_j^x | 0 \rangle &= (-1)^j m_s. \end{aligned} \quad (3.3.2)$$

It is invariant under translations over lattice vectors respecting the bipartite breakup of the lattice. Later on we will come back to this feature. The search for the spin stiffness ρ_s can be formulated as finding an excitation $|\tilde{\mathbf{q}}\rangle$ such that

$$\begin{aligned} \langle \tilde{\mathbf{q}} | \mathcal{H} | \tilde{\mathbf{q}} \rangle &= E_0 + \frac{1}{2} N \rho_s |\mathbf{q}|^2 + \dots, \\ \langle \tilde{\mathbf{q}} | S_j^x | \tilde{\mathbf{q}} \rangle &= (-1)^j m_s \cos(\mathbf{q} \cdot \mathbf{r}_j), \\ \langle \tilde{\mathbf{q}} | S_j^y | \tilde{\mathbf{q}} \rangle &= (-1)^j m_s \sin(\mathbf{q} \cdot \mathbf{r}_j). \end{aligned}$$

The implementation of a twisted orientation like this is a hard task. It can be avoided by a similarity transformation. Define the unitary operator $\mathcal{U}(\mathbf{q})$ by

$$\mathcal{U}(\mathbf{q}) = \exp \left(i \mathbf{q} \cdot \sum_j \mathbf{r}_j S_j^z \right). \quad (3.3.3)$$

It corresponds to a rotation about the S^z -axis. It is easy to derive that

$$\mathcal{U}(\mathbf{q}) S_j^+ \mathcal{U}^\dagger(\mathbf{q}) = S_j^+ e^{i \mathbf{q} \cdot \mathbf{r}_j}, \quad \mathcal{U}(\mathbf{q}) S_j^- \mathcal{U}^\dagger(\mathbf{q}) = S_j^- e^{-i \mathbf{q} \cdot \mathbf{r}_j}.$$

We will now transfer the twist from the order parameter to the Hamiltonian with this operator $\mathcal{U}(\mathbf{q})$. Define

$$\begin{aligned} \mathcal{H}(\mathbf{q}) &= \mathcal{U}(\mathbf{q}) \mathcal{H} \mathcal{U}^\dagger(\mathbf{q}) \\ &= \frac{J_1}{2} \sum_{\langle ij \rangle} e^{i \mathbf{q} \cdot (\mathbf{r}_j - \mathbf{r}_i)} S_j^+ S_i^- + e^{-i \mathbf{q} \cdot (\mathbf{r}_j - \mathbf{r}_i)} S_j^- S_i^+ + 2 S_j^z S_i^z \\ &\quad + \frac{J_2}{2} \sum_{[ij]} e^{i \mathbf{q} \cdot (\mathbf{r}_j - \mathbf{r}_i)} S_j^+ S_i^- + e^{-i \mathbf{q} \cdot (\mathbf{r}_j - \mathbf{r}_i)} S_j^- S_i^+ + 2 S_j^z S_i^z \end{aligned} \quad (3.3.4)$$

and $|\mathbf{q}\rangle = \mathcal{U}(\mathbf{q}) |\bar{\mathbf{q}}\rangle$. Combining the expressions for $|\bar{\mathbf{q}}\rangle$ and $\mathcal{H}(\mathbf{q})$ it is trivial to deduce that this new state $|\mathbf{q}\rangle$ satisfies

$$\begin{aligned} \langle \mathbf{q} | \mathcal{H}(\mathbf{q}) | \mathbf{q} \rangle &= E_0 + \frac{1}{2} N \rho_s |\mathbf{q}|^2 + \dots, \\ \langle \mathbf{q} | S_j^x | \mathbf{q} \rangle &= (-1)^j m_s. \end{aligned} \quad (3.3.5)$$

$|\mathbf{q}\rangle$ clearly is an excitation of $\mathcal{H}(\mathbf{q})$ as the ground state is trivially given by $\mathcal{U}(\mathbf{q})|0\rangle$. We know that

$$\lim_{\mathbf{q} \rightarrow 0} |\mathbf{q}\rangle = |0\rangle,$$

which can be read as an invitation to apply perturbation theory. Still there is a quite subtle issue that must not be overlooked. If we would apply perturbation theory without further ado, the resulting wave function would be $\mathcal{U}(\mathbf{q})|0\rangle$. The order parameter would also be twisted and consequently it would not satisfy (3.3.5);

$$\begin{aligned} \langle 0 | \mathcal{U}^\dagger(\mathbf{q}) S_j^x \mathcal{U}(\mathbf{q}) | 0 \rangle &= (-1)^j m_s \cos(\mathbf{q} \cdot \mathbf{r}_j), \\ \langle 0 | \mathcal{U}^\dagger(\mathbf{q}) S_j^y \mathcal{U}(\mathbf{q}) | 0 \rangle &= -(-1)^j m_s \sin(\mathbf{q} \cdot \mathbf{r}_j). \end{aligned}$$

The underlying physical idea is that if we apply a twist with wave vector \mathbf{q} by slowly turning up this \mathbf{q} , the system and the order parameter will follow adiabatically and no energy increase will occur. This is not what we set out to achieve. We are considering the case where an integer twist over the entire system exists. The wave vectors \mathbf{q} that are allowed then fit the lattice; all terms $\exp(i \mathbf{q} \cdot (\mathbf{r}_i - \mathbf{r}_j))$ can be simplified to $\exp(i \mathbf{q} \cdot \mathbf{r}_s)$ where \mathbf{r}_s is the smallest connecting lattice vector. Even when \mathbf{r}_i and \mathbf{r}_j are adjacent across the periodic boundary of the system this replacement can be done as $\mathbf{q} \cdot (\mathbf{r}_i - \mathbf{r}_j) \equiv \mathbf{q} \cdot$

$\mathbf{r}_i \bmod 2\pi$. To summarise, we seek the homogeneous state $|\mathbf{q}\rangle$ given an integer twist over the lattice. Respecting this subtlety, $|\mathbf{q}\rangle$ can be derived.

Define

$$\begin{aligned}\bar{j} &= \frac{d}{d\mathbf{q}} \mathcal{H}(\mathbf{q}) \Big|_{\mathbf{q}=0} = \frac{iJ_1}{2} \sum_{\langle ij \rangle} (\mathbf{r}_j - \mathbf{r}_i) (\mathcal{S}_j^+ \mathcal{S}_i^- - \mathcal{S}_j^- \mathcal{S}_i^+) \\ &\quad + \frac{iJ_2}{2} \sum_{[ij]} (\mathbf{r}_j - \mathbf{r}_i) (\mathcal{S}_j^+ \mathcal{S}_i^- - \mathcal{S}_j^- \mathcal{S}_i^+), \\ \bar{t} &= - \frac{d^2}{d\mathbf{q}^2} \mathcal{H}(\mathbf{q}) \Big|_{\mathbf{q}=0} = \frac{J_1}{2} \sum_{\langle ij \rangle} (\mathbf{r}_j - \mathbf{r}_i) (\mathbf{r}_j - \mathbf{r}_i) (\mathcal{S}_j^+ \mathcal{S}_i^- + \mathcal{S}_j^- \mathcal{S}_i^+) \\ &\quad + \frac{J_2}{2} \sum_{[ij]} (\mathbf{r}_j - \mathbf{r}_i) (\mathbf{r}_j - \mathbf{r}_i) (\mathcal{S}_j^+ \mathcal{S}_i^- + \mathcal{S}_j^- \mathcal{S}_i^+).\end{aligned}$$

A part of the terms $\mathbf{r}_i - \mathbf{r}_j$ is in place here. The factors $\exp(i\mathbf{q} \cdot (\mathbf{r}_i - \mathbf{r}_j))$ as appearing in $\mathcal{H}(\mathbf{q})$ are periodic in the difference $\mathbf{r}_i - \mathbf{r}_j$. Adding or subtracting a vector (nL, mW) leaves this term invariant. When taking the derivative it is therefore necessary to insert the smallest possible argument for $\mathbf{r}_i - \mathbf{r}_j$. So when \mathbf{r}_i and \mathbf{r}_j are on opposite sides of the periodic boundary we have to replace them by \mathbf{r}_δ , the connecting elementary lattice vector.

The state $|\mathbf{q}\rangle$ is now given in first order perturbation theory by

$$|\mathbf{q}\rangle = \left(1 + i\mathbf{q} \cdot \frac{1}{E_0 - \mathcal{H}} \bar{j} + \dots \right) |0\rangle.$$

This state clearly satisfies the condition on the order parameter (3.3.5) as both the current-current correlation j and the kinetic term t are translational invariant. The expression for the stiffness ρ_s can now readily be obtained;

$$\begin{aligned}\bar{\rho}_s &= -\frac{1}{N} \langle 0 | \bar{t} | 0 \rangle + \frac{1}{N} \langle 0 | \bar{j} \frac{1}{E_0 - \mathcal{H}} \bar{j} | 0 \rangle \\ &\equiv \bar{T} + \bar{J}.\end{aligned}\tag{3.3.6}$$

The spin stiffness $\bar{\rho}_s$ is a tensor and only when the system has quadratic symmetry it can be denoted by a scalar.

The ground state $|0\rangle$ is reflection symmetric whereas the current \bar{j} is not. Therefore $\langle 0 | \bar{j} | 0 \rangle = 0$ and we can safely write the current-current correlation as

$$\bar{J} = \frac{1}{N} \langle 0 | \bar{j} \frac{1}{E_0 - \mathcal{H}} \bar{j} | 0 \rangle = \frac{1}{N} \sum_a \frac{\langle 0 | \bar{j} | a \rangle \langle a | \bar{j} | 0 \rangle}{E_0 - E_a}.\tag{3.3.7}$$

For expression (3.3.6) to hold, it is essential that the system is translational invariant in the direction of the twist \mathbf{q} . Recapturing the subtlety in the derivation, it can be readily seen that open boundary condition will not lead to the correct result. In that geometry we will

find $|\mathbf{q}\rangle = \mathcal{U}(\mathbf{q})|0\rangle$. We can borrow a physical argument from the realm of superfluidity to put this in a broader context.

Periodic boundary conditions can easily be achieved for a bucket of helium by bending this bucket round a massive cylinder and connecting both ends together on the other side of the cylinder. The twist we apply corresponds to a steady rotation of this cylinder with the bucket around it. The superfluid will not respond to this twist whereas the normal component of the helium will start to rotate along. In the frame of the cylinder it is the superfluid that flows, whereas the normal helium remains inert. Consequently, the kinetic energy increases by the superfluid current.

Open boundaries correspond to helium in a closed bucket. The walls of a closed bucket prevent a current from running and a zero increase in energy will be the result. It is worthwhile mentioning that Pollock and Ceperley [37] have implemented this idea directly in a Green Function Monte Carlo calculation. They follow a particle winding around a periodic cell. If it winds faster round a periodic cell than expected by Brownian motion, superfluidity exists.

The formula (3.3.6) is applicable to systems exhibiting all kinds of long-range magnetic order. If another type of ordering was twisted with an order parameter which was also defined locally, the same route would have led to this general result. The assumption of antiferromagnetic order can therefore be dropped and we end up with a fairly general expression for $\tilde{\rho}_s$ at zero temperature. The only restriction is naturally that the order must break the symmetry; otherwise Goldstone modes or spin waves will not appear and no twist is possible. Equation (3.3.6) is completely equivalent with the expression found in [12] and [16].

3.4 Schwinger-Boson Mean Field Approximation

The behaviour of the spin stiffness in a two-dimensional system can be obtained by finite-size scaling analysis of relatively small systems. It is then necessary to establish the size dependence of the properties and in the current and following sections we will derive these in the SBMF approximation.

The Schwinger-boson representation is in itself a mere reformulation of the problem. The only extra condition that has to be imposed is that the number of bosons per site has to be fixed to 1. Any operator correctly transformed into the language of Schwinger-bosons will conserve this property.

Standard mean field theory is based on the assumption that there are only small fluctuations in the orientation of the spins. In our case that is a poor approximation; quantum fluctuations play a major role. In the unfrustrated case, $J_2 = 0$, Monte Carlo calculations [48, 43] have shown that the staggered magnetisation is about 60% of the classical value.

A possible improvement of the mean field is to incorporate correlations between neighbouring spins. The Schwinger-boson mean field approximation is a first step in this direction. It was originally introduced by Arovas and Auerbach [2] Here we will apply this approximation and derive expressions for the energies and wave functions of all states of

the frustrated Heisenberg model. This will be done both for Néel and collinear ordered ground state.

The first step in this method is to represent every spin by two bosons;

$$\begin{aligned} S^+ &= a^\dagger b, \\ S^- &= ab^\dagger, \\ S^z &= \frac{1}{2}(a^\dagger a - b^\dagger b). \end{aligned} \quad (3.4.1)$$

We restrict ourselves to the subspace in which $a^\dagger a + b^\dagger b = 2S$, where S is the total length of the spin. In this case $S = \frac{1}{2}$. Two observations can be made:

- The combinations of bosons in (3.4.1) satisfy all commutation relations of the original operators.
- None of the operators S^+ , S^- and S^z will connect this subspace to subspaces of other total spin since they all commute with $a^\dagger a + b^\dagger b$. Therefore the Hamiltonian will only map states in this subspace onto other states in the same subspace.

The Schwinger-Boson representation is therefore just a reformulation of the problem. The transformation in (3.4.1) does not favour any specific orientation of the magnetic order and the mean field approximation for these bosons will also preserve this symmetry.

Now the mean field approximation can be developed. Many authors have done this before [2] and we follow the route taken by Mila et al. [31] for this particular problem. As stated before we will consider two types of ordering: Néel and collinear.

We begin with the Néel ordering. This is expected to be the preferred ordering when $J_2 \ll J_1$.

A first step towards the mean field approximation is to rotate the spins over π around the S^z -axis on one of the two sublattices;

$$\begin{aligned} S_i^+ &\rightarrow (-1)^i S_i^+, \\ S_i^- &\rightarrow (-1)^i S_i^-, \\ S_i^z &\rightarrow S_i^z. \end{aligned} \quad (3.4.2)$$

This transformation is inspired by the Marshall sign rule [29], which states that in this new basis the ground state of the unfrustrated antiferromagnet has only positive definite coefficients. It is of course not strictly necessary, but it avoids the need of complex numbers which otherwise would appear.

For the mean fields only those combinations of creation and annihilation operators can be taken that are invariant under rotation round the S^z -axis. Define

$$\mathcal{D}_{ij} = a_i a_j^\dagger + b_i b_j^\dagger, \quad (3.4.3)$$

$$\mathcal{B}_{ij} = a_i b_j + b_i a_j. \quad (3.4.4)$$

The Hamiltonian becomes

$$\mathcal{H} = -\frac{J_1}{2} \sum_{\langle ij \rangle} (\mathcal{B}_{ij}^\dagger \mathcal{B}_{ij} - \frac{1}{2}) + \frac{J_2}{2} \sum_{[ij]} (\mathcal{D}_{ij}^\dagger \mathcal{D}_{ij} - \frac{3}{2}).$$

where we have inserted (3.4.3) for the ferromagnetic oriented pairs of spins and (3.4.4) for the antiferromagnetic ones. This expression is related to the fact that if two spins are aligned, $B_{ij}|\uparrow\uparrow\rangle = 0$. Likewise for singlet combinations, it holds that $\mathcal{D}_{ij}(|\uparrow\downarrow\rangle - |\downarrow\uparrow\rangle) = 0$. Still, the equivalent of \mathcal{D}_{ij} could in principle appear on the nearest neighbour bonds. Rotating the spins on one sublattice yields

$$\mathcal{D}_{ij}^\dagger \mathcal{D}_{ij} \rightarrow (a_i^\dagger a_j - b_i^\dagger b_j)(a_i a_j^\dagger - b_i b_j^\dagger).$$

The optimal mean field solution—self consistent with lowest energy—turns out to satisfy $\langle (a_i a_j^\dagger - b_i b_j^\dagger) \rangle = 0$ for nearest neighbours. The same holds for the equivalent of B_{ij} on next-nearest neighbour bonds. Therefore we will neglect these terms.

The final step is to replace the products of these two operators \mathcal{D}_{ij} and B_{ij} by their mean field approximations. Set $\gamma_{ij} = \frac{1}{2}\langle B_{ij} \rangle$ for nearest-neighbour bonds and $\kappa_{ij} = \frac{1}{2}\langle \mathcal{D}_{ij} \rangle$ for the next-nearest neighbour bonds. In the regime of Néel ordering, we only consider the translationally invariant solutions, so $\gamma_{ij} \rightarrow \gamma$, $\kappa_{ij} \rightarrow \kappa$. In figure 3-1 these mean fields are represented. When the decoupling is made, the detailed constraint $a^\dagger a + b^\dagger b = 1$ is no longer satisfied as the Hamiltonian will now also map out of this subspace. Paradoxically, if the constraint were conserved in detail, the mean fields γ and κ would become identical to zero as both alter the number of particles on individual sites. The constraint $a^\dagger a + b^\dagger b = 1$ will be relaxed to only hold on average, $\langle a^\dagger a + b^\dagger b \rangle = 1$. Given the translational invariance of the system, this can be replaced by a global version and enforced by a Lagrange multiplier, i.e.

$$\mathcal{H} \rightarrow \mathcal{H}_{\text{MF}} + \lambda \sum_i (a_i^\dagger a_i + b_i^\dagger b_i - 1). \quad (3.4.5)$$

Introducing the quantities h_p and Δ_p

$$h_p = 4J_2\kappa \cos p_x \cos p_y, \quad (3.4.6)$$

$$\Delta_p = 2J_1\gamma(\cos p_x + \cos p_y), \quad (3.4.7)$$

the Fourier-transformed Hamiltonian reads

$$\mathcal{H} = E_c + \sum_p (h_p + \lambda)(a_p^\dagger a_p + b_p^\dagger b_p) - \Delta_p(a_p^\dagger b_{-p}^\dagger + a_p b_{-p}), \quad (3.4.8)$$

with

$$E_c = 2N \left[J_1 \left(\frac{1}{4} + 2\gamma^2 \right) - J_2 \left(\frac{3}{4} + 2\kappa^2 \right) - \lambda \right].$$

A solution to this Hamiltonian can be found through the Bogoliubov transformation from (a_p, b_p) to (α_p, β_p) :

$$\begin{aligned} a_p &= \alpha_p \cosh \theta_p + \beta_p^\dagger \sinh \theta_p, \\ b_{-p}^\dagger &= \alpha_p \sinh \theta_p + \beta_p^\dagger \cosh \theta_p, \\ \tanh 2\theta_p &= \frac{\Delta_p}{h_p + \lambda}. \end{aligned} \quad (3.4.9)$$

If we define the excitation energies $\omega_{\mathbf{p}}$ by

$$\omega_{\mathbf{p}} = \sqrt{(h_{\mathbf{p}} + \lambda)^2 - \Delta_{\mathbf{p}}^2}, \quad (3.4.10)$$

the Hamiltonian becomes

$$\mathcal{H} = E_c + \sum_{\mathbf{p}} \omega_{\mathbf{p}} (\alpha_{\mathbf{p}}^\dagger \alpha_{\mathbf{p}} + \beta_{\mathbf{p}} \beta_{\mathbf{p}}^\dagger). \quad (3.4.11)$$

As in all mean field theories the energy has to be stationary with respect to κ , γ and λ . This yields the equations

$$\frac{\partial \mathcal{H}}{\partial \lambda} = \frac{h_0 + \lambda}{2\omega_0} \cos p_x \cos p_y, \quad (3.4.12)$$

$$\frac{\partial \mathcal{H}}{\partial \gamma} = \frac{\Delta_0}{2\omega_0} (\cos p_x + \cos p_y), \quad (3.4.13)$$

$$\frac{\partial \mathcal{H}}{\partial \kappa} = \frac{h_0 + \lambda}{2\omega_0}. \quad (3.4.14)$$

As only cosines appears in these equations either as single terms or in the right combinations, the $\mathbf{p} = (0, 0)$ and the $\mathbf{p} = (\pi, \pi)$ terms are completely equivalent. For future applications it is also useful to define what will turn out to be the 'condensate' m_s

$$m_s = \frac{h_0 + \lambda}{N\omega_0}. \quad (3.4.15)$$

This is the sum of the contributions of the $\mathbf{p} = 0$ and the $\mathbf{p} = (\pi, \pi)$ terms in the summations (3.4.12) and (3.4.14). As these are identical, it is twice the ' $\mathbf{p} = 0$ '-term. If the system size N becomes infinite, $N \rightarrow \infty$, m_s equals twice the ' $\mathbf{p} = 0$ '-term in (3.4.13). It is no coincidence that m_s also appears as the size of the order parameter in equation (3.3.2). By inserting a symmetry breaking term $\eta \sum_j (-1)^j S_j^x$ in the Hamiltonian, it can be shown through a short but subtle calculation that the equation (3.3.2) —without the staggering $(-1)^j$ — will hold for the ground state of the SBMF Hamiltonian with infinitely small symmetry breaking field $\eta = \mathcal{O}(1/N)$. The staggering $(-1)^j$ has disappeared from the formulae by the transformation (3.4.2).

As long as there is Néel order the condensate m_s will naturally be positive. It will obtain a limit value in the case of an infinite system size N ; $\lim_{N \rightarrow \infty} m_s = \text{const} > 0$. This finishes the discussion of the Néel ordered ground state.

Next we consider the collinear order. The route to follow is quite similar to the one just finished. We can therefore be brief about it. Introduce the transformation

$$\begin{aligned} S_{(x,y)}^+ &\rightarrow (-1)^y S_{(x,y)}^+, \\ S_{(x,y)}^- &\rightarrow (-1)^y S_{(x,y)}^-, \\ S_{(x,y)}^z &\rightarrow S_{(x,y)}^z. \end{aligned}$$

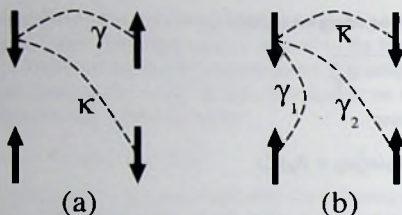


Figure 3-1. The mean fields for the Néel (a) and the collinear order (b).

Again we perform a rotation over π around the S^z -axis, however this time not on one of the sublattices but on every other row. Define the mean fields $\bar{\kappa} = \frac{1}{2}\langle D_{i,i+\hat{x}} \rangle$ over nearest-neighbour bonds in the x -direction, $\gamma_1 = \frac{1}{2}\langle B_{i,i+\hat{y}} \rangle$ over the nearest-neighbour bonds in the y -direction and $\gamma_2 = \frac{1}{2}\langle B_{i,i\pm\hat{x}\pm\hat{y}} \rangle$ over the next-nearest-neighbour bonds. The quantities \bar{h}_p and $\bar{\Delta}_p$ are now given by

$$\begin{aligned}\bar{h}_p &= 2J_1\bar{\kappa}\cos p_x, \\ \bar{\Delta}_p &= 2J_1\gamma_1\cos p_y + 4J_2\gamma_2\cos p_x\cos p_y.\end{aligned}\quad (3.4.16)$$

After a Fourier and a Bogoliubov transformation, similar to (3.4.8) and (3.4.9), we obtain

$$\mathcal{H} = \bar{E}_c + \sum_p \bar{\omega}_p (\bar{\alpha}_p^\dagger \bar{\alpha}_p + \bar{\beta}_p \bar{\beta}_p^\dagger).$$

This is equivalent to (3.4.11) where $\bar{\omega}$ and \bar{E}_c are now given by

$$\begin{aligned}\bar{\omega}_p &= \sqrt{(\bar{h}_p + \bar{\lambda})^2 - \bar{\Delta}_p^2}, \\ \bar{E}_c &= 2N \left(J_1(\gamma_1^2 - \bar{\kappa}^2 - \frac{1}{4}) + J_2(\frac{1}{4} + 2\gamma_2^2) - \bar{\lambda} \right).\end{aligned}\quad (3.4.17)$$

The consistency equations for these parameters are

$$\bar{\kappa} = \frac{1}{N} \sum_p \frac{\bar{h}_p + \bar{\lambda}}{2\bar{\omega}_p} \cos p_x, \quad (3.4.18)$$

$$\gamma_1 = \frac{1}{N} \sum_p \frac{\bar{\Delta}_p}{2\bar{\omega}_p} \cos p_y, \quad (3.4.19)$$

$$\gamma_2 = \frac{1}{N} \sum_p \frac{\bar{\Delta}_p}{2\bar{\omega}_p} \cos p_x \cos p_y, \quad (3.4.20)$$

$$1 = \frac{1}{N} \sum_p \frac{\bar{h}_p + \bar{\lambda}}{2\bar{\omega}_p}. \quad (3.4.21)$$

The 'condensate' \bar{m}_s is defined in a similar manner as before in (3.4.15), that is

$$\bar{m}_s = \frac{\bar{h}_0 + \bar{\lambda}}{N\bar{\omega}_0}. \quad (3.4.22)$$

The symmetry of the collinear order differs from that of the Néel order. This condensate contains the contribution of the $\mathbf{p} = 0$ and $\mathbf{p} = (0, \pi)$ terms in the summations (3.4.18) and (3.4.21). These are identical and once again the condensate \bar{m}_s is twice the ' $\mathbf{p} = 0$ '-term. If the system size $N \rightarrow \infty$ it also becomes twice the ' $\mathbf{p} = 0$ '-term of (3.4.19) and (3.4.20).

The main weakness of the SBMF approach lies in the handling of the particle constraint $a^\dagger a + b^\dagger b = 1$. It is only conserved on average by use of a Lagrange multiplier, equation (3.4.5). The ground state will have non-zero weight in configurations that have either too many or too few bosons on a specific site. This space is different from the original spin space and no direct correspondence to the ground state of the frustrated Heisenberg model exists.

A connection with the original, frustrated Heisenberg model can be made that involves a restriction of the state and a transformation of the basis; first the ground state of the SBMF Hamiltonian has to be restricted to the subspace where the condition $a^\dagger a + b^\dagger b = 1$ holds in detail. Afterwards, pairs of bosons ($a^\dagger a$ etc.) have to be replaced by spin operators. The restricted wave function now lies in the correct space and can serve as an approximation to the true ground state of the frustrated Heisenberg model. Wei and Tao [50] make this connection for the unfrustrated case, $J_2 = 0$. The properties that they extract from this approximate ground state agree surprisingly well with the numerical results for the true ground state from various Monte Carlo calculations.

In this chapter we will not follow their route back to the spin problem, but remain in the larger, bosonic space. The properties we obtain should thus be appreciated as such; they are related to those of the ground state of the frustrated Heisenberg model and should be seen as indications of the behaviour of the frustrated Heisenberg model.

The mean field approximation has provided the energies and wave functions of all states of the Hamiltonian and we can proceed to the calculation of the spin stiffness ρ_s .

3.5 Spin stiffness in SBMF

How can ρ_s be defined properly in the mean field Hamiltonian? This question might seem trivial, but a closer investigation reveals that there are two approaches:

- Start with the original Heisenberg Hamiltonian \mathcal{H} . Induce a twist with wavelength \mathbf{q} (just like has been done in section 3.3) and afterwards apply the appropriate mean field approximation. ρ_s is related to the ground state energy of this mean field Hamiltonians, i.e.

$$\mathcal{H} \rightarrow \mathcal{H}(\mathbf{q}) \rightarrow \mathcal{H}_{\text{MF}}(\mathbf{q}), \quad \bar{\rho}_s = \frac{1}{N} \frac{d^2 \langle \mathcal{H}_{\text{MF}}(\mathbf{q}) \rangle}{d\mathbf{q}^2}.$$

- Swapping the first two steps of the previous approach; first apply mean field and then twist, i.e.

$$\mathcal{H} \rightarrow \mathcal{H}_{\text{MF}} \rightarrow \tilde{\mathcal{H}}_{\text{MF}}(\mathbf{q}) \quad , \quad \bar{\rho}_s = \frac{1}{N} \frac{d^2 \langle \tilde{\mathcal{H}}_{\text{MF}}(\mathbf{q}) \rangle}{d\mathbf{q}^2}.$$

In the mean field approximation we use here, these two approaches give the same result. Still, the correct approach is the first one, as there the energy increase of the original Hamiltonian due to the twist is approximated. The second approach replaces the original Hamiltonian by a mean field one and starts to investigate the response of the mean field Hamiltonian to a twist.

The calculation of the energy $\langle \mathcal{H}(\mathbf{q}) \rangle$ is a simple repetition of the approach for $\mathbf{q} = 0$. This allows a fairly direct derivation of the spin stiffness avoiding second order perturbation theory. Still, the aim of this chapter is to obtain the finite-size scaling relations for the kinetic term \bar{T} and the current-current correlation \bar{J} independently. These relations will then be used to extrapolate the data of the DMRG calculations to infinitely large system sizes. We will therefore follow the -general- route of second order perturbation theory.

We can use the formulae derived earlier in (3.3.6), but simply taking the mean field ground state to replace the true ground state in this expression will not suffice; the second term contains an inversion which we cannot handle in this form. It is necessary to insert the mean field Hamiltonian \mathcal{H}_{MF} . In doing so we extend our SBMF approximations to the entire spectrum.

The SBMF approximation thus has to be performed on the twisted Hamiltonian, $\mathcal{H}(\mathbf{q})$, and the first and second derivative are needed to calculate the stiffness ρ_s in second order perturbation theory. This in itself is very similar to the description above for the untwisted situation and left to appendix A. The expressions for the current and kinetic operators are

$$\begin{aligned} \bar{J} &= \sum_F J_{ij} \kappa_{ij} (\tilde{\mathcal{F}}_{ij}^\dagger + \tilde{\mathcal{F}}_{ij}) - \sum_{AF} J_{ij} \gamma_{ij} (\tilde{\mathcal{C}}_{ij}^\dagger + \tilde{\mathcal{C}}_{ij}), \\ \bar{T} &= \frac{1}{2} \sum_F J_{ij} \kappa_{ij} (\mathbf{r}_i - \mathbf{r}_j)(\mathbf{r}_i - \mathbf{r}_j) (\mathcal{D}_{ij}^\dagger + \mathcal{D}_{ij} - 2\kappa_{ij}) \\ &\quad - \frac{1}{2} \sum_{AF} J_{ij} \gamma_{ij} (\mathbf{r}_i - \mathbf{r}_j)(\mathbf{r}_i - \mathbf{r}_j) (\mathcal{B}_{ij}^\dagger + \mathcal{B}_{ij} - 2\gamma_{ij}). \end{aligned}$$

From this point on, we set $\mathbf{q} = q(\cos \phi, \sin \phi)$. Of the two terms for ρ_s in (3.3.6), T is evaluated more easily:

$$\begin{aligned} \bar{T} &= -\frac{1}{N} \langle 0 | \bar{T} | 0 \rangle \\ &= \frac{1}{N} \sum_{AF} J_{ij} \gamma_{ij}^2 (\mathbf{r}_i - \mathbf{r}_j)(\mathbf{r}_i - \mathbf{r}_j) - \frac{1}{N} \sum_F J_{ij} \kappa_{ij}^2 (\mathbf{r}_i - \mathbf{r}_j)(\mathbf{r}_i - \mathbf{r}_j). \end{aligned}$$

For the two orderings considered in the last section, this expression boils down to

$$T^{\text{neel}} = J_1 \gamma^2 - 2J_2 \kappa^2, \quad (3.5.1)$$

$$T^{\text{coll}} = 2J_2 \gamma_2^2 + J_1 \left(\gamma_1^2 \sin^2 \phi - \kappa^2 \cos^2 \phi \right). \quad (3.5.2)$$

These simple equations hold for all system sizes N .

The derivation of \bar{J} requires somewhat more effort. First the matrix element $\langle 0|\bar{J}|a\rangle$ has to be calculated. As $|a\rangle$ is an excitation of \mathcal{H}_{MF} , it has to fulfill the relation

$$|a\rangle = \alpha_1^\dagger \dots \alpha_i^\dagger \beta_1^\dagger \dots \beta_j^\dagger |0\rangle.$$

Of these the only relevant ones are

$$|a\rangle = \alpha_{\mathbf{p}_1}^\dagger \beta_{\mathbf{p}_2}^\dagger |0\rangle,$$

as can be established by applying the Bogoliubov transformations (3.4.9) to \bar{C}_{ij} and \bar{F}_{ij} . The matrix element itself is a combination of $\langle 0|\bar{F}_{ij}|a\rangle$ and $\langle 0|\bar{C}_{ij}|a\rangle$. By means of simple algebra, we obtain

$$\sum_{\mathbf{p}} \langle 0|\bar{F}_{ij}|a\rangle = -2\delta_{\mathbf{p}_1, \mathbf{p}_2} \mathbf{r}_\delta \sinh 2\theta_{\mathbf{p}_1} \sin(\mathbf{p}_1 \cdot \mathbf{r}_\delta),$$

$$\sum_{\mathbf{p}} \langle 0|\bar{C}_{ij}|a\rangle = -2\delta_{\mathbf{p}_1, \mathbf{p}_2} \mathbf{r}_\delta \cosh 2\theta_{\mathbf{p}_1} \sin(\mathbf{p}_1 \cdot \mathbf{r}_\delta).$$

The $\mathbf{p}_1 = \mathbf{p}_2 = \mathbf{p}$, thus $E_a = E_0 + \omega_{\mathbf{p}_1} + \omega_{\mathbf{p}_2} = E_0 + 2\omega_{\mathbf{p}}$. Inserting all these expressions in the equation for J , (3.3.7), will give the explicit formula for J . The Hamiltonian in that expression is \mathcal{H}_{MF} . For the two types of ordering J is:

$$\begin{aligned} J^{\text{neel}} &= -\frac{1}{N} \sum_{\mathbf{p}} \frac{\sin^2 p_y}{\omega_{\mathbf{p}}^3} (J_1 \gamma (h_{\mathbf{p}} + \lambda) - 2J_2 \kappa \Delta_{\mathbf{p}} \cos p_x)^2 \\ J^{\text{coll}} &= -\frac{1}{N} \sum_{\mathbf{p}} \frac{1}{\omega_{\mathbf{p}}^3} \left(\cos \phi \sin p_x [J_1 \bar{\kappa} \bar{\Delta}_{\mathbf{p}} - 2J_2 \gamma_2 (\bar{h}_{\mathbf{p}} + \bar{\lambda}) \cos p_y] \right. \\ &\quad \left. - \sin \phi \sin p_y [J_1 \gamma_1 (\bar{h}_{\mathbf{p}} + \bar{\lambda}) + 2J_2 \gamma_2 (\bar{h}_{\mathbf{p}} + \bar{\lambda}) \cos p_x] \right)^2. \end{aligned} \quad (3.5.3)$$

In the introduction of the SBMF we already defined the $\mathbf{p} = 0$ term of the summations separately. The condensate is defined in expression (3.4.15) for the Néel order and (3.4.22) for the collinear order. Here we also have to be careful with these terms. For the infinitely large lattice these equations can be simplified by replacing summations by integrals, i.e.:

$$\frac{1}{N} \sum_{\mathbf{p}} \dots \rightarrow \frac{1}{(2\pi)^2} \int d\mathbf{p} \dots,$$

but all divergent terms have to be taken separately, e.g.

$$1 = \frac{1}{N} \sum_{\mathbf{p}} \frac{h_{\mathbf{p}} + \lambda}{2\omega_{\mathbf{p}}} \rightarrow 1 = m_s + \frac{1}{(2\pi)^2} \int d\mathbf{p} \frac{h_{\mathbf{p}} + \lambda}{2\omega_{\mathbf{p}}},$$

where m_s is defined in equation (3.4.15). Partial integration over \mathbf{p} yields:

$$\begin{aligned} J^{\text{neel}} &= J_1 \gamma (m_s - \gamma) - 2J_2 \kappa (m_s - \kappa), \\ J^{\text{coll}} &= 2J_2 \gamma_2 (\bar{m}_s - \gamma_2) \\ &\quad + J_1 \left(\gamma_1 (\bar{m}_s - \gamma_1) \sin^2 \phi - \bar{\kappa} (\bar{m}_s - \bar{\kappa}) \cos^2 \phi \right). \end{aligned}$$

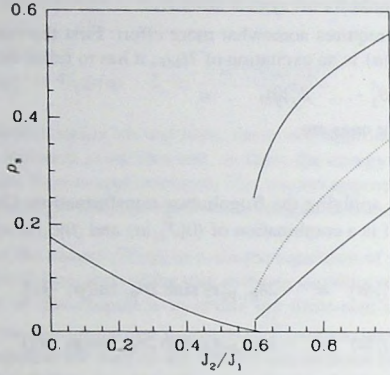


Figure 3-2. The spin stiffness ρ_s in units of J_1 as function of the ratio J_2/J_1 (solid lines). For the collinear ordering the spin stiffness in the direction of the ferromagnetic order (lower solid curve) and in the direction of the antiferromagnetic order (upper solid curve) are drawn. The dotted line is the result found by Ivanov and Ivanov [26] for the collinear ordering.

These expressions for J only hold for infinite system size N , in contrast with the expressions for T in (3.5.1) and (3.5.2).

The spin stiffness is given by $\rho_s = T + J$, thus for $N \rightarrow \infty$

$$\rho_s^{\text{neel}} = m_s(J_1\gamma - 2J_2\kappa), \quad (3.5.4)$$

$$\bar{\rho}_s^{\text{coll}} = \bar{m}_s \begin{pmatrix} 2J_2\gamma_2 - J_1\bar{\kappa} & 0 \\ 0 & 2J_2\gamma_2 + J_1\gamma_1 \end{pmatrix}. \quad (3.5.5)$$

In figure 3-2 the numerical results of these formula are presented. The phase transition is first order and no intermediate phase exists. This is in contrast with statements in the literature [16, 58], that suggest an intermediate phase of dimer or plaquette order. Einarsson and Schulz [16] studied the spin stiffness on small clusters and extrapolated those results to the two-dimensional geometry. In their results the spin stiffness vanishes in the region $0.4 \lesssim J_2/J_1 \lesssim 0.6$.

Ivanov and Ivanov [26] have applied a different method to obtain ρ_s . They consider the correlation function $\xi = \langle \vec{S}_i \cdot \vec{S}_j \rangle$. Comparison of this correlation function ξ with the non-linear sigma model where $\xi \sim \exp(2\pi\rho_s/T)$ (here T stands for the temperature), yields

$$\rho_s^{\text{neel}} = m_s(J_1\gamma - 2J_2\kappa),$$

$$\rho_s^{\text{coll}} = \bar{m}_s \sqrt{(2J_2\gamma_2 - J_1\bar{\kappa})(2J_2\gamma_2 + J_1\gamma_1)}.$$

Our expression for the collinear ordering is different from theirs. This is not very surprising as they do not take anisotropy explicitly into account. Their result is the geometric mean of the two components in (3.5.5).

This section was started with a discussion on the route to be taken; whether first to twist or apply mean field. It was stated there that both would lead to the correct answer. This can now easily be seen. As $\langle \tilde{\mathcal{F}}_{ij} \rangle = \langle \tilde{\mathcal{C}}_{ij} \rangle = 0$ there is indeed no difference.

3.6 Isotropic Scaling

Often it is impossible to obtain the values of observables in a system of infinite size ($N \rightarrow \infty$). One approach to overcome this obstacle is to derive the values for various system sizes and afterwards extrapolate to the infinite size. This is for instance done with data from quantum Monte Carlo calculations and exact diagonalisation methods. It is necessary to know the size dependence of the observables to obtain a good approximate for their limiting values.

Recently some controversy has arisen about the size dependence of ρ_s [17]. It was suggested that the lack of proper scaling behaviour on small systems for intermediate range of frustration $0.4 \lesssim J_2/J_1 \lesssim 0.6$ is an indication of the absence of long-range magnetic order. It is therefore worthwhile to take a closer look at the scaling behaviour of the various quantities. This is not a hard task as all formulas in the last section have an explicit size dependence. We will show that this lack of scaling behaviour does not only appear for intermediate range of frustration, but is a general feature of small systems.

We will focus on the Néel ordering as an example. We want to know the scaling behaviour of the condensate m_s , and the two terms J and T that make up ρ_s ($\rho_s = T + J$). The latter two will turn out to have different scaling behaviour. The following discussion is entirely based on the fact that the dispersion relation $\omega_{\mathbf{k}}$ is a periodic function that is smooth and positive everywhere except at 0 and (π, π) where we see a linear behaviour; e.g. $\omega_{\mathbf{k}} = c|\mathbf{k}|$ for $|\mathbf{k}| \ll 1$, the spin wave velocity.

First the condensate m_s is considered. It is defined by $m_s(N) = (h_0 + \lambda)/(N\omega_0)$ or

$$\frac{m_s(N)}{2} = 1 - \frac{1}{N} \sum_{\mathbf{p} \neq 0} \frac{h_{\mathbf{p}} + \lambda_N}{2\omega_{\mathbf{p}}}. \quad (3.6.1)$$

In the limit $N \rightarrow \infty$ the parameters (κ_N , γ_N , λ_N) will obtain their limiting value (κ , γ , λ) and the summation can be replaced by an integration. Both changes will give rise to corrections. We carefully investigate the size of these corrections below.

It is known that $\lim_{N \rightarrow \infty} m_s(N) = m_s > 0$. This can also be expressed as $\lim_{N \rightarrow \infty} (h_0 + \lambda)/(N\omega_0) = m_s$ or inverting this relation into one for $\omega_{\mathbf{p}}$ at $|\mathbf{p}| \ll 1$

$$\omega_{\mathbf{p}} = \sqrt{\frac{K_0}{N^2} + c^2 p^2}. \quad (3.6.2)$$

The two constants in this formula are given by

$$K_0 = N^2 \left[(4J_2\kappa_N + \lambda_N)^2 - (4J_1\gamma_N)^2 \right] = \left(\frac{4J_2\kappa_N + \lambda_N}{m_s(N)} \right)^2, \quad (3.6.3)$$

$$c^2 = \frac{1}{2} \left[\lambda_N^2 - (4J_2\kappa_N)^2 \right] + O\left(\frac{1}{N^2}\right).$$

The suggestive notation c^2 anticipates that this is the spin wave velocity since an antiferromagnet has a linear dispersion relation $\omega_{\mathbf{p}} = c|\mathbf{p}|$ for low energy. For finite system size N the smallest \mathbf{q} -vector in the summation (3.6.1) has length $|\mathbf{p}| = \frac{2\pi}{L}$ ($L^2 = N$). This means that the \mathbf{q} -independent term, K_0/N^2 , is small compared to the \mathbf{q} -dependent term and gives rise to corrections of at least the order $O(1/N^2)$ in the summation. We replace κ_N , γ_N and λ_N by their limiting values κ , γ and λ and thereby neglect these corrections of order $O(1/N^2)$. As the term $\mathbf{p} = 0$ is excluded the summation still is finite.

The other effect, replacement of the summation by the integration, can be treated quantitatively due to a lemma by Neuberger and Ziman [32]. They consider a function $f(\mathbf{p})$ that is periodic on the Brillouin zone. If this function $f(\mathbf{p})$ satisfies $\frac{f(\mathbf{p})}{|\mathbf{p}|} \rightarrow 1$ as $|\mathbf{p}| \rightarrow 0$ and $f(\mathbf{p})$ is non-zero and smooth in the rest of the Brillouin zone, then

$$\frac{1}{N} \sum_{\mathbf{p} \neq 0} \frac{1}{f(\mathbf{p})} - \frac{1}{(2\pi)^2} \int d\mathbf{p} \frac{1}{f(\mathbf{p})} = \frac{\alpha(L^2/W^2)}{\sqrt{N}}$$

We respect their notation by taking the argument L^2/W^2 . The numerical value $\alpha(1) = 0.6208$ was computed in [32].

In our situation the limit $|\mathbf{p}| \rightarrow 0$ is given by

$$\lim_{\mathbf{p} \rightarrow 0} \frac{1}{|\mathbf{p}|} \frac{2\omega_{\mathbf{p}}}{h_{\mathbf{p}} + \lambda} \sqrt{2} \sqrt{\frac{\lambda - 4J_2\kappa}{\lambda + 4J_2\kappa}}.$$

The quoted lemma therefore leads to

$$m_s(N) - m_s = \frac{0.6208}{\sqrt{N}} \sqrt{2} \sqrt{\frac{\lambda + 4J_2\kappa}{\lambda - 4J_2\kappa}}.$$

This result is in excellent agreement with the numerical values we get when the equations (3.4.12-3.4.14) are solved and the obtained κ_N , γ_N and λ_N are inserted in (3.6.1). This is depicted in figure 3-3. For values of $J_2 > 0.62$ we know from figure 3-2 that the phase becomes unstable and it is no surprise that the data does not longer fit the scaling relation.

The derivation of the scaling behaviour of J proceeds in the same manner as above. The starting point is (3.5.3). The result is

$$J_N - J = \frac{0.6208}{\sqrt{N}} \frac{\sqrt{\lambda^2 - (4J_2\kappa)^2}}{4\sqrt{2}} = \frac{0.6208}{\sqrt{N}} \frac{c}{4}.$$

Again we find excellent agreement with the numerical results in figure 3-4 upto $J_2 = 0.62$, where the Néel phase becomes unstable.

To obtain the scaling behaviour of T a more involved reasoning is required. As is seen in (3.5.1) it depends both on κ_N and γ_N . They are part of the set $(\kappa_N, \gamma_N, \lambda_N)$ of solutions to (3.4.12-3.4.14). As these are mutually dependent they have to be solved simultaneously.

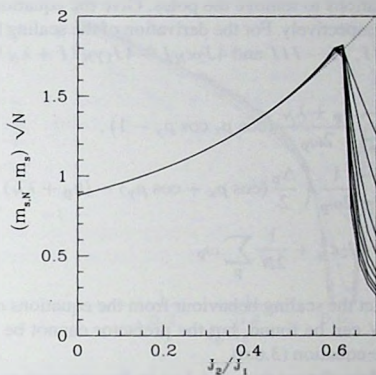


Figure 3-3. The numerical scaling behaviour of m_s (solid lines) for sizes $N = 10^2, 20^2, \dots, 90^2$ (bottom-up) compared with the theoretical curve (dotted line). At $J_2/J_1 = 0.62$ the ground state becomes unstable and the discussion on the scaling behaviour is no longer applicable.

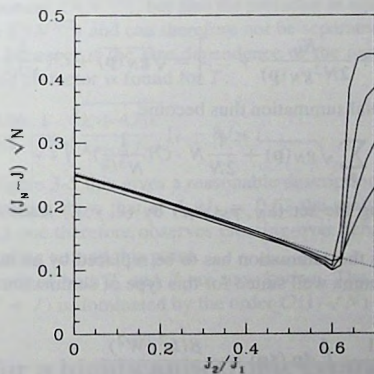


Figure 3-4. The numerical scaling behaviour of J (solid lines) for sizes $N = 10^2, 20^2, 40^2, 100^2$ (bottom-up) compared with the theoretical curve (dotted line).

In the formulation of (3.4.12-3.4.14) the divergent ' $\mathbf{p} = 0$ '-terms are still included. We will rearrange these equations to remove the poles. Give the equations (3.4.12-3.4.14) the numbers I, II and III respectively. For the derivation of the scaling behaviour we will use the combinations I - III, II - III and $4J_2\kappa_N I - 4J_1\gamma_N II + \lambda_N III$, or (using (3.4.6), (3.4.7) and (3.4.10))

$$\kappa_N = 1 + \frac{1}{N} \sum_{\mathbf{p}} \frac{h_{\mathbf{p}} + \lambda_N}{2\omega_{\mathbf{p}}} (\cos p_x \cos p_y - 1), \quad (3.6.4)$$

$$\gamma_N = 1 + \frac{1}{N} \sum_{\mathbf{p}} \frac{1}{2\omega_{\mathbf{p}}} \left(\frac{\Delta_{\mathbf{p}}}{2} (\cos p_x + \cos p_y) - (h_{\mathbf{p}} + \lambda_N) \right), \quad (3.6.5)$$

$$\lambda_N = 4J_1\gamma_N^2 - 4J_2\kappa_N^2 + \frac{1}{2N} \sum_{\mathbf{p}} \omega_{\mathbf{p}}. \quad (3.6.6)$$

It is not possible to extract the scaling behaviour from the equations completely in analytic form: the exponent of N can be found, but the prefactor cannot be derived. As an example we consider the equation (3.6.6).

First we want to replace the set $(\kappa_N, \gamma_N, \lambda_N)$ in the summation over $\omega_{\mathbf{p}}$ by $(\kappa, \gamma, \lambda)$. From (3.6.2) we know that $\omega_{\mathbf{p}}$ has the general form

$$\omega_{\mathbf{p}} = \sqrt{\frac{K_0}{N^2} + g_N(\mathbf{p})}.$$

where $g_N(\mathbf{p}) \approx c^2|\mathbf{p}|^2$ if $\frac{2\pi}{L} \leq |\mathbf{p}| \ll 1$. On all lattice points except the origin $g_N(\mathbf{p}) \gg K_0/N^2$. We have $\omega_0 = \mathcal{O}(1/N)$ or $1/2N\omega_0 = \mathcal{O}(1/N^2)$. For $\mathbf{p} \neq 0$ we can expand $\omega_{\mathbf{p}}$ in K_0/N^2 :

$$\omega_{\mathbf{p}} = \sqrt{g_N(\mathbf{p})} \left[1 + \frac{K_0}{2N^2 g_N(\mathbf{p})} + \dots \right] = \sqrt{g_N(\mathbf{p})} + \mathcal{O}\left(\frac{1}{N^{3/2}}\right).$$

The corrections in the total summation thus become

$$\frac{1}{2N} \sum_{\mathbf{p}} \omega_{\mathbf{p}} = \frac{1}{2N} \sum_{\mathbf{p}} \sqrt{g_N(\mathbf{p})} + \frac{1}{2N} N \cdot \mathcal{O}\left(\frac{1}{N^{3/2}}\right).$$

This means that replacing the set $(\kappa_N, \gamma_N, \lambda_N)$ by $(\kappa, \gamma, \lambda)$ leads to errors of the order $\mathcal{O}(1/N^{3/2})$.

As in previous cases the summation has to be replaced by an integral. Neuberger and Ziman [32] provide a lemma well suited for this type of summation. It reads: consider the same $f(\mathbf{p})$ as before,

$$\frac{1}{N} \sum_{\mathbf{p} \neq 0} f(\mathbf{p}) - \frac{1}{(2\pi)^2} \int d\mathbf{p} f(\mathbf{p}) = -\frac{\beta(L^2/W^2)}{N^{3/2}} \quad (3.6.7)$$

The numerical value $\beta(1) = -0.7186$ was computed in [32]. Application of this lemma again leads to corrections of the order $\mathcal{O}(1/N^{3/2})$. In a similar manner the other equations for κ and γ can be treated.

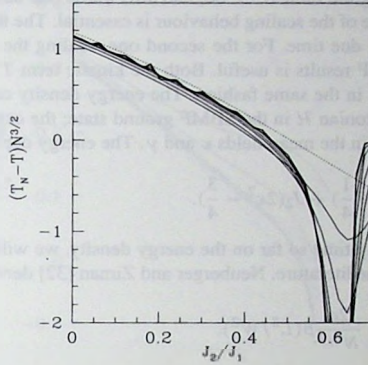


Figure 3-5. The numerical scaling behaviour of T for square systems of size $N = 10^2, 20^2, \dots, 90^2$. The $N^{3/2}$ -scale is derived from analytical arguments in the text. The dotted line gives the expected behaviour if the size dependence of κ , γ and λ inside the summations (3.6.4-3.6.6) is neglected.

We now have two sources of finite-size corrections. On one hand the dependence of κ , γ and λ on the systems size. We know the exponent of this correction, $\mathcal{O}(N^{3/2})$, but not the prefactor. On the other hand we have the correction arising from the summations. There we not only know the exponent, $\mathcal{O}(N^{3/2})$, but also the prefactor in equation (3.6.7). Since both size dependencies are $\mathcal{O}(N^{3/2})$ and can therefore not be separated, it is not easy to obtain the overall prefactor. However if the size dependence of the parameters ($\kappa_N, \gamma_N, \lambda_N$) is neglected the following prefactor is found for T :

$$T_N - T = \frac{0.7186}{N^{3/2}} \frac{1}{\sqrt{2}} \sqrt{\frac{\lambda + 4J_2\kappa}{\lambda - 4J_2\kappa}} [\lambda - 8J_2\kappa]. \quad (3.6.8)$$

As can be seen in figure 3-5 this gives a reasonable description for not too large J_2/J_1 . The numerical calculations show that at $J_2/J_1 = 0.62$ the scaling behaviour is of order $\mathcal{O}(1/N)$. In figure 3-5 one therefore observes crossing-over behaviour from $\mathcal{O}(1/N^{3/2})$ -scaling to $\mathcal{O}(1/N)$ -scaling around this point.

The size dependence of both T and J are now known. The scaling behaviour of the spin stiffness $\rho_s (= T + J)$ is dominated by the order $\mathcal{O}(1/\sqrt{N})$ -behaviour of J .

3.7 Scaling for a highly anisotropic geometry

The DMRG method that we will employ in the next chapter, allows us to study systems of fairly large length L while the width W has to remain small. This fact can be seen as an invitation to apply a two-step scaling procedure; first the length dependence is removed from

the observables by taking the limit $L \rightarrow \infty$, and afterwards one takes the limit $W \rightarrow \infty$. For both steps knowledge of the scaling behaviour is essential. The first step is fairly trivial and will be discussed in due time. For the second one, scaling the width W away, some guidance from the SBMF results is useful. Both the kinetic term T and the energy density E_0/N can be treated in the same fashion. The energy density can be simply obtained by evaluating the Hamiltonian \mathcal{H} in the SBMF ground state; the expectation values of the operators can be written in the mean fields κ and γ . The energy density is given by

$$\frac{E_0}{N} = -2J_1(2\gamma^2 - \frac{1}{4}) + J_2(2\kappa^2 - \frac{3}{4}).$$

As we have not spent any time so far on the energy density, we will start with the scaling behaviour observed in the literature. Neuberger and Ziman [32] derive

$$\frac{E_0}{N} - \lim_{N \rightarrow \infty} \frac{E_0}{N} = \frac{2c}{N^{3/2}} \beta(L^2/W^2).$$

The function β is the same as defined in (3.6.7). We thus seek the behaviour of β as $L \rightarrow \infty$. Neuberger and Ziman's approach [32] can be extended to this situation. Still, the algebraic manipulations are quite tedious [36] and using

$$\zeta(3) = \sum_{n=1}^{\infty} \frac{1}{n^3} = 1.2021,$$

they lead to

$$\lim_{L \rightarrow \infty} \frac{\beta(L^2/W^2)}{(LW)^{3/2}} = -\frac{1.2021}{2\pi W^3}.$$

As expected all length dependence drops out and only a finite width dependence remains. When we neglect the dependence of the parameters κ , γ and λ on the system size as before in (3.6.8), the expressions for the energy density E_0/N and the kinetic term T are

$$\frac{E_0}{N} - \lim_{N \rightarrow \infty} \frac{E_0}{N} = -\frac{1.2021}{\pi W^3} c. \quad (3.7.1)$$

$$T_N - T = \frac{1.2021}{2\sqrt{2}\pi W^3} \sqrt{\frac{\lambda + 4J_2\kappa}{\lambda - 4J_2\kappa}} [\lambda - 8J_2\kappa]. \quad (3.7.2)$$

In figure 3-6 we have numerically checked the second of these predictions. Just like in the isotropic case, the power is correct and the prefactor is reasonable.

Unfortunately a similar limit $L \rightarrow \infty$ can not be taken in the scaling expression for the current-current correlation J . The reason can be found in the underlying assumptions; we supposed that the dispersion relation is linear and the correction due to the fact the $\omega_{\mathbf{k}}$ has a gap Δ , as presented in (3.6.2) has been neglected. For a highly anisotropic system, $L \rightarrow \infty$, this assumption is not allowed. We can illustrate this by an example: the summation over

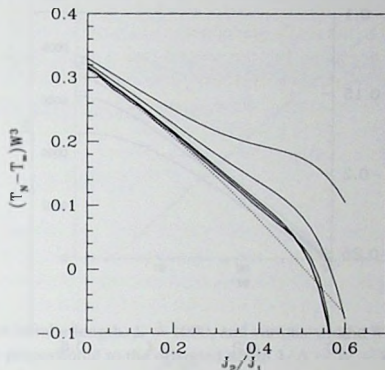


Figure 3.7. The scaling of a system of 'almost' infinite length $L = 4000$ and finite width $W = 6, 8, 10, 12, 14, 20$ (top-down). The dotted line is the theoretical curve given in equation (3.7.2).

reciprocal lattice in the long direction of the system can be replaced by an integral and the outcome diverges;

$$\frac{1}{LW} \sum_{k_x, k_y} \frac{1}{|\mathbf{k}|} = \frac{1}{W} \sum_{k_y} \frac{1}{2\pi} \int dk_x \frac{1}{\sqrt{k_x^2 + k_y^2}} \rightarrow \infty,$$

whereas the infinite size expression stays bounded;

$$\frac{1}{(2\pi)^2} \int d\mathbf{k} \frac{1}{|\mathbf{k}|} = \text{finite}.$$

The analytical expression we therefore should derive, involves the gap Δ . Above we mentioned that it is not possible to obtain the prefactor of the scaling behaviour of γ , κ and λ . The gap Δ is directly expressed in these three quantities and its explicit size dependence therefore becomes just as elusive. However, we can resort to numerical means. In figure 3-7 we establish that the current-current correlation shows a $1/W$ scaling behaviour.

To conclude, the width W has taken over the position of the square root of the system size, \sqrt{N} , in all scaling relations when the highly anisotropic limit of $L \rightarrow \infty$ is taken. ($\sqrt{N} = \sqrt{LW}$) This is naturally not surprising as the smallest dimension of the system is W which should set the length scale.

In the next chapter a brief discussion will be given of the behaviour of the energy gap Δ . This is the energy difference between the ground state singlet and the first excitation triplet. For an infinite large system with spin waves this gap obviously will be zero whereas for other types of order it might remain finite. For reasons to be outlined later, we will consider the member of this triplet with $S^z = 1$. In the SBMF approximation the gap Δ is given by

$$\Delta = 2\omega_0.$$

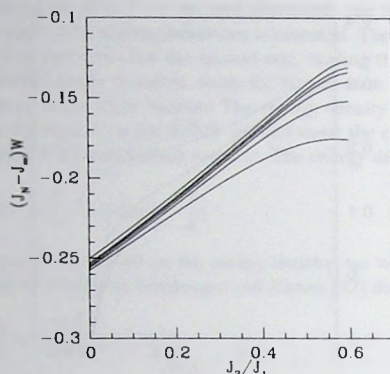


Figure 3-7. The scaling of a system of 'almost' infinite length $L = 4000$ and finite width $W = 6, 8, 10, 12, 14, 20$ (bottom-up).

The factor 2 can easily be understood if we rewrite the operator S^z in the excitation operators α_k and β_k :

$$\begin{aligned} S^z &= \sum_j S_j^z = \frac{1}{2} \sum_j (a_j^\dagger a_j - b_j^\dagger b_j) \\ &= \frac{1}{2} \sum_k (a_k^\dagger a_k - b_k^\dagger b_k) = \frac{1}{2} \sum_k (\alpha_k^\dagger \alpha_k - \beta_k^\dagger \beta_k). \end{aligned}$$

The ground state contains no excitations so $S^z|0\rangle = 0$. The $S^z = 1$ -space can be reached by creating *two* excitations; $S^z \alpha_0^\dagger \alpha_0^\dagger |0\rangle = 1 \cdot \alpha_0^\dagger \alpha_0^\dagger |0\rangle$. This is not surprising in the view of the fact that the number of bosons should be conserved on a site. Applying only one creation operator creates an excitation that does not satisfy this condition. When two creation operators are applied to the ground state, their combination contains terms that do satisfy this condition, for example, it contains terms of the form $a_j^\dagger b_j$.

From (3.6.2) and (3.6.3) we know that the gap $\Delta = 2\omega_0 = 2\sqrt{K_0}/N$ has a very subtle size dependence as κ , λ and γ have an $\mathcal{O}(1/N^{3/2})$ dependence but K_0/N^2 has an $\mathcal{O}(1/N^2)$ dependence. Adding to this the high anisotropy, we can only establish the finite-size corrections numerically. The best fit with a simple function is a size dependence $\Delta \sim 1/(W - W_0)$ as can be seen in figure 3-8. This is in line with the idea that the gap Δ can be considered proportional to the inverse of the correlation length. The smallest length scale in the system is W leading to a $1/W$ behaviour.

Unfortunately, the scaling of the gap does not follow the route that previous scaling relations have followed. The scaling behaviour of E_0/N , T and J in the highly anisotropic limit can be summarised as replacing the system size N in the formulae for the isotropic

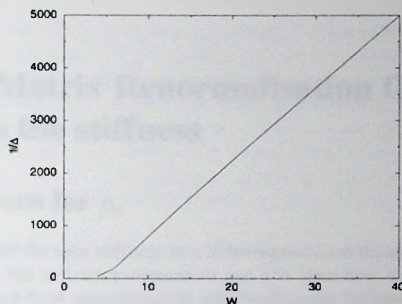


Figure 3.8. For almost infinite length, $L = 1000$, and various widths W we observe that the inverse of the gap Δ is linear proportional to the offsetted width $1/\Delta \sim W - W_0$.

geometry by W^2 . For the gap Δ that would lead to a $1/W^2$ dependence whereas we actually find a $1/(W - W_0)$ dependence.

3.8 Conclusions

In this chapter we have employed the SBMF approximation to get the approximate phase diagram of the frustrated Heisenberg model. We found two phases, Néel and collinear. The energies of both ground states suggest a first order phase transition at $J_2/J_1 \approx 0.595$. There is no evidence for an intermediate phase. SBMF approximations in line with either dimer-like order always yield higher ground state energies. As mentioned before there are several articles in the literature where an intermediate phase is suggested [16, 58].

The second half of the chapter was spent on finite-size scaling. The scaling behaviour of various quantities (ρ_s , J , ...) was derived for both square, $L = W$, and a highly anisotropic geometry, $L \gg W$. These scaling relations will be used in the next chapter to extrapolate the numerical data to infinite system size.

1000
800
600
400
200
0

0

Figure 1. The ground state energy E_0 as a function of the coupling ratio J_2/J_1 for the frustrated Heisenberg model on a square lattice. The data points are shown for $L=16, 24, 32, 48, 64, 96, 128, 192, 256, 384, 512, 768, 1024$. The solid line represents the extrapolation to the thermodynamic limit.

Table 1. The ground state energy E_0 and the spin stiffness ρ_s for the frustrated Heisenberg model on a square lattice. The data points are shown for $L=16, 24, 32, 48, 64, 96, 128, 192, 256, 384, 512, 768, 1024$. The solid line represents the extrapolation to the thermodynamic limit.

3.3. Conclusions

In this chapter we have studied the ground state energy and the spin stiffness of the frustrated Heisenberg model on a square lattice. We have shown that the ground state energy and the spin stiffness are both functions of the coupling ratio J_2/J_1 . The ground state energy is a decreasing function of J_2/J_1 , while the spin stiffness is an increasing function. The data points are shown for $L=16, 24, 32, 48, 64, 96, 128, 192, 256, 384, 512, 768, 1024$. The solid line represents the extrapolation to the thermodynamic limit.

It is interesting to note that the ground state energy and the spin stiffness are both functions of the coupling ratio J_2/J_1 . This is a consequence of the fact that the ground state energy and the spin stiffness are both determined by the same underlying physics.

The ground state energy and the spin stiffness are both functions of the coupling ratio J_2/J_1 . This is a consequence of the fact that the ground state energy and the spin stiffness are both determined by the same underlying physics.

4 Density Matrix Renormalisation Group approach to the stiffness

4.1 Expressions for ρ_s

In chapter 3 we studied the spin stiffness in a Schwinger-boson mean-field approximation. In that case the order has a distinct orientation and it is clear how to twist it. If we do not resort to a similar mean-field approximation and consider the frustrated Heisenberg model on a finite-size lattice, the orientation of the ground state is not as well defined. This model has a continuous symmetry; homogeneous rotations in spin space leave the Hamiltonian invariant. We also know that in a finite system the ground state is unique. It therefore has to be rotationally invariant. Only in an infinitely large system spontaneous symmetry breaking can occur and we can associate a direction with the order of the ground state. The only other way to break the symmetry is by enforcing an orientation. This is for instance the case in a mean-field approximation.

The orientation of the order is thus homogeneously distributed over the sphere; every orientation in spin space is just as likely. The twist we apply has a plane associated with it. Previously we twisted in the $x - y$ plane. The fraction of the ground state oriented along the z -axis will not be affected by this twist. Leaving out that fraction, we only twist $2/3$ of the order parameter. To compensate for that we follow Einarsson and Schulz [16] and introduce

$$T_{sym} = \frac{3}{2}T, \quad J_{sym} = \frac{3}{2}J,$$

with T and J given in (3.3.6). The spin stiffness is given by

$$\rho_s = T_{sym} + J_{sym}. \quad (4.1.1)$$

A further complication lies in the numerical nature of our approach. Unfortunately the ground state we calculate, will not be entirely rotational symmetric. The reason for this touches on the very nature of spontaneous symmetry breaking. As the Hamiltonian is rotational invariant, it only takes a small field to orient the ground state. Basis states in line with this field will prevail. In standard mean-field approximations we use this by introducing external fields to fix the orientation. Here we go a step further and directly meddle with the basis. By definition we start our DMRG calculation with an asymmetric and poor basis. At each step the ground state wave function will be symmetry broken in the same orientation as the basis. The following basis truncation will again be asymmetric. Even if we were to start off with a symmetric basis, numerical errors would break the symmetry eventually. It is very difficult to maintain a global symmetry by means of iterative local basis updates.

To repair this partial symmetry breaking, we would have to incorporate the rotational symmetry exactly in the procedure. The DMRG method allows for certain symmetries to be conserved as was extensively discussed in chapter 2. A good example is S^z , which we also conserve in the present calculations. This is possible because to every basis state we can assign a quantum number s^z . The S^z for the entire system is then the sum of the s^z of the basis states on the individual parts. It would be nice if also the total spin S could be conserved, but we will argue that this is not feasible. The ground state $|\psi_0\rangle$ lies in the $S = 0$ space. The conditions for this restriction can be easily derived:

$$\begin{aligned} S^2|\psi_0\rangle = 0 &\rightarrow \sum_{\alpha=x,y,z} S^\alpha{}^2|\psi_0\rangle = 0 \\ &\rightarrow \langle\psi_0|(S^\alpha)^2|\psi_0\rangle = |S^\alpha|\psi_0\rangle|^2 = 0 \\ &\rightarrow S^\alpha|\psi_0\rangle = 0. \end{aligned}$$

These conditions are rephrased to reflect that we work in the basis that conserves S^z .

$$S^z|\psi_0\rangle = S^+|\psi_0\rangle = S^-|\psi_0\rangle = 0 \quad (4.1.2)$$

A direct consequence of fulfilling (4.1.2) is a rotationally invariant ground state, as the global rotations in spin space over an angle r are given by $\exp(irS^\alpha)$.

Our approximation $|\phi_0\rangle$ already satisfies the first condition of (4.1.2), $S^z|\phi_0\rangle = 0$, in a standard implementation of the DMRG. Conservation of the second and third condition would require for each basis state in an individual part A of the system $|i\rangle_A$ the image $S_A^\pm|i\rangle_A$. This would scale up the number of basis states tremendously and the calculation would become prohibitively large. We will therefore neglect this symmetry and evaluate ground state wave functions that are only approximately rotational invariant.

On the other hand, there is no reason why the symmetry should be *completely* broken; for narrow systems, the DMRG is accurate enough to compensate for this symmetry breaking tendency.

In general the final ground state will be somewhere in between a symmetry broken state and a rotational invariant state. The expressions for the kinetic term T and the current-current correlation J can be symmetrised to overcome this orientational problem:

$$\begin{aligned} T_{all} &= J_1 \sum_{\langle ij \rangle} (\hat{q} \cdot (\vec{r}_i - \vec{r}_j))^2 \vec{S}_i \cdot \vec{S}_j + J_2 \sum_{\langle ij \rangle} (\hat{q} \cdot (\vec{r}_i - \vec{r}_j))^2 \vec{S}_i \cdot \vec{S}_j, \\ J_{all} &= i J_1 \sum_{\langle ij \rangle} (\hat{q} \cdot (\vec{r}_i - \vec{r}_j)) \vec{S}_i \times \vec{S}_j + i J_2 \sum_{\langle ij \rangle} (\hat{q} \cdot (\vec{r}_i - \vec{r}_j)) \vec{S}_i \times \vec{S}_j, \end{aligned}$$

and define

$$T_{all} = -\frac{1}{N} \langle \phi_0 | T_{all} | \phi_0 \rangle, \quad J_{all}^\alpha = \frac{1}{N} \langle \phi_0 | J_{all}^\alpha \frac{1}{E_0 - \mathcal{H}} J_{all}^\alpha | \phi_0 \rangle,$$

then the stiffness ρ_s is given by

$$\rho_s = T_{all} + \frac{1}{2} \sum_{\alpha=x,y,z} J_{all}^\alpha. \quad (4.1.3)$$

Three current-current correlation J_{alt}^α have to be calculated for (4.1.3) whereas only one J_{sym} for expression (4.1.1). In the next section we will see that this is substantial more involved and we prefer to use formula (4.1.1) whenever the accuracy permits us to. In practice this means that for narrow systems we use the symmetric form. For wider systems the general form is necessary.

4.2 Calculating wave functions

The expressions for the stiffness ρ_s in (4.1.1) and (4.1.3), have to be implemented numerically. The first ingredient is the ground state. A standard implementation of the DMRG results in a good estimate $|\phi_0\rangle$ of the ground state. The kinetic term T can be obtained by a simple measurement on this wave function $|\phi_0\rangle$. However the current-current correlation J needs a more elaborate approach.

An inversion has to be performed for J . We will prove that we can invert $E_0 - \mathcal{H}$ within the subspace spanned by the basis states for the various parts. To derive this we first take a step back and inspect the method to calculate the ground state. At each iteration of the DMRG the state $|\phi_0\rangle$ in the subspace that has a minimal energy $E_0 = \langle \phi_0 | \mathcal{H} | \phi_0 \rangle / \langle \phi_0 | \phi_0 \rangle$, is selected. This energy E_0 is always larger than the true ground state energy and we thus have a variational principle. At every next iteration we can improve upon our estimate by simply minimising E_0 further starting with the -truncated- outcome of the previous iteration. This variational principle is crucial for the method as it enables to distinguish the best approximation to the ground state from other configurations in the basis.

We can design a similar variational principle for the inversion. Define $g(x)$,

$$g(x) = \frac{1}{2} \langle x | \mathcal{H} - E_0 | x \rangle + \langle x | \phi_j \rangle, \quad (4.2.1)$$

where $|\phi_j\rangle = j|\phi_0\rangle$ and E_0 is the best estimate of the ground state energy known at that point in the procedure¹. This function has a global minimum at

$$|x\rangle = |\phi_1\rangle = \frac{1}{E_0 - \mathcal{H}} |\phi_j\rangle, \quad (4.2.2)$$

as the quadratic term, $\frac{1}{2} \langle x | \mathcal{H} - E_0 | x \rangle$, is positive definite. In the realm of linear algebra $|\phi_1\rangle$ is called the correction vector. This function provides us with a variational principle similar to the one we had before. Moreover the minimum of the function within a specific subspace is also given by (4.2.2) where $|\phi_1\rangle$, $|\phi_j\rangle$ and \mathcal{H} are now restricted to that subspace. The inversion within the subspace is thus the best approximation we can make for the global minimum.

At every step the subspace changes and we can get closer to the real inverse $|\phi_1\rangle$. If $|\phi_j\rangle$ is known with high accuracy, $1/(E_0 - \mathcal{H})|\phi_j\rangle$ can be obtained with similar accuracy. A nice by-product is that

$$g(\phi_1) = \frac{1}{2} \langle \phi_0 | j \frac{1}{E_0 - \mathcal{H}} j | \phi_0 \rangle; \quad (4.2.3)$$

¹Unfortunately this is not always the latest calculated energy; it tends to fluctuate. This was already discussed at the end of section 2.4.

Apart from the prefactor this is essentially the expression for J .

The basis has to be tuned to present these wave functions $\{|\phi_0\rangle, |\phi_j\rangle, |\phi_i\rangle\}$ optimally. The reason for including the first wave function, $|\phi_0\rangle$, may be evident. The other two are necessary, since we need expression (4.2.3) accurately. If the basis does not properly represent $|\phi_i\rangle$ or $|\phi_j\rangle$, $g(\phi_i) = \frac{1}{2}\langle\phi_j|\phi_i\rangle$ is incorrect. To adjust the basis to these wave functions we have to incorporate them in the density matrix. Let us briefly outline the reasoning behind that. Define the truncation error P by

$$P = \left| |\phi_0\rangle - |\tilde{\phi}_0\rangle \right|^2 + \left| |\phi_j\rangle - |\tilde{\phi}_j\rangle \right|^2 + \left| |\phi_i\rangle - |\tilde{\phi}_i\rangle \right|^2.$$

The tilde denotes the projection of the wave function on the truncated basis. The truncation error P has to be minimal. A few linear algebra manipulations leads to the density matrix

$$\rho_{ii'} = \rho_{ii'}^0 + \rho_{ii'}^j + \rho_{ii'}^i. \quad (4.2.4)$$

The density matrix is thus the sum of the individual density matrices. As ρ is the most important states correspond to the eigenvectors of this density matrix ρ with the largest eigenvalues. The different density matrices could have different weights, but the effect on the accuracy of the spin stiffness is unknown. We set them therefore to be equal.

The remaining issue of the last section has now also been answered; expression (4.1.3) for ρ_s is more elaborate than (4.1.1) as three instead of one inversions have to be performed. Moreover all these extra wave functions (four in total; two extra currents and two extra inverses) have to be included in the density matrix along the lines of equation (4.2.4). Naturally the basis will then be less suited for each individual wave function and an overall loss of accuracy will follow.

4.3 Geometry

The shape of the systems we study is dictated by limitations of the DMRG. Their width is fairly restricted (maximally 8 sites wide) and periodicity along the length of the system is not feasible. Earlier we explained that the spin stiffness can only be measured with the expressions we derived if the axis along which we twist, denoted by \hat{q} , is periodic. We used two different arguments for this, that are both valid in their own right; first, the perturbation theory for an open system will not give the desired state and energy. Secondly, a similarity with superfluidity exists; a superfluid cannot flow freely when there is an impenetrable wall in its way.

The system thus has to be periodic in the -narrow- width direction and open in the length direction; the shape of a cylinder.

The model itself puts some extra constraints on the wrapping of the lattice around the cylinder. In order to frustrate neither the Néel nor the collinear ordering, the periodicity of 2 lattice sites has to be satisfied.

The two lattices depicted in figure 4-1 fulfill both requirements. The width W of the lattice is the number of sites one passes going round the cylinder. The length on the other hand is the maximum number of sites one encounters while scanning along the long direction.

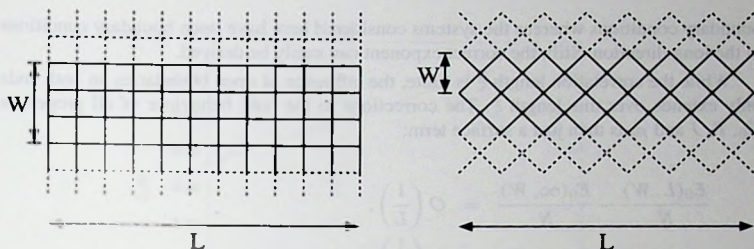


Figure 4.1: The square and the tilted square lattice of width W and length L . In the square lattice the periodicity is along the vertical lattice-axis. In the tilted lattice the periodicity is along the (vertical) diagonal of the lattice. Periodic images of the nearest neighbour bounds are depicted by dashed lines

When the next-nearest-neighbour coupling becomes dominant, these lattices both fall apart in two sublattices. For the square lattice, these sublattices have an effective width of $W/2$, whereas the tilted lattice breaks up in sublattices of width W . Knowing that the accuracy of the DMRG rapidly decreases with increasing width of the system, we expect results of a strongly decreasing accuracy for the tilted lattices with increasing frustration J_2 .

The direction $\hat{\mathbf{q}}$ in which the stiffness is measured is different for the square and for the tilted square lattice. The square lattice allows a measurement along the axis corresponding to the width direction of the cylinder. On the tilted lattice the direction to be taken is the diagonal of the lattice. In short:

$$\text{Square lattice : } \hat{\mathbf{q}} = \begin{pmatrix} 0 \\ 1 \end{pmatrix}, \quad \text{Tilted square lattice : } \hat{\mathbf{q}} = \frac{1}{\sqrt{2}} \begin{pmatrix} 1 \\ 1 \end{pmatrix}.$$

4.4 Scaling

The DMRG accuracy rapidly decreases with increasing system width W . It becomes therefore necessary to apply finite-size scaling theory to obtain quantities of the two-dimensional system. Here we implement a two step scaling where we can use the discussion on anisotropic scaling in the previous chapter and the scaling analysis of the two-dimensional ITF in sections 1.5.1 and 1.5.2.

The first step exploits the strength of the DMRG; for a fixed width W it is numerically not difficult to vary the length L substantially. By doing so, we can extract the dependence of various quantities on this length L and remove it. The remaining fraction corresponds to a system of length $L = \infty$. To obtain this one-dimensional scaling behaviour we can not employ the SBMF approximation of the previous chapter. That was based on periodic

boundary conditions whereas the systems considered here have open boundary conditions in the long direction. Still, the correct exponent can easily be derived.

While the correlation length ξ is finite, the influence of open boundaries on both ends only extends over this length ξ . The corrections to the bulk behaviour of all properties E_0 , T , J and ρ_s is then just a surface term;

$$\frac{E_0(L, W)}{N} - \frac{E_0(\infty, W)}{N} = \mathcal{O}\left(\frac{1}{L}\right),$$

$$T(L, W) - T(\infty, W) = \mathcal{O}\left(\frac{1}{L}\right),$$

$$J(L, W) - J(\infty, W) = \mathcal{O}\left(\frac{1}{L}\right),$$

$$\rho_s(L, W) - \rho_s(\infty, W) = \mathcal{O}\left(\frac{1}{L}\right).$$

For the second step, scaling in the width direction, we fall back on the expressions derived in the previous chapter. As the length has become infinite, $L \rightarrow \infty$, it is no longer relevant whether the corresponding boundary is open or periodic. We can refer to the results for the periodic case derive before; expressions (3.7.1) and (3.7.2) contain the $\mathcal{O}(1/W^3)$ scaling behaviour for the energy density E_0/N and the kinetic term T respectively. With the help of (3.7.1) we can also extract the spin wave velocity c . Moreover figure 3-7 demonstrates the $\mathcal{O}(1/W)$ scaling behaviour that SBMF yields for the current-current correlation J .

4.5 Results

Reliable finite-size scaling requires a substantial number of data points. We have considered various system sizes to make -at least- the first step in the scaling procedure, $L \rightarrow \infty$, indisputable. For the square geometry (see figure 4-1 widths $W = 4, 6, 8$ were considered and for the tilted geometry widths $W = 2, 4$ were studied. In all graphs we set $J_1 = 1$.

We have used both DMRG variants, the original one proposed by White [51] and our implementation [15]. For this model we confirm the statements made in chapter 2; the variant of White is much more flexible. On the other hand, our variant needs 30% fewer states for a similar accuracy in the calculation. Furthermore the ground state is more symmetric as the translational symmetry is strictly conserved. A relative small extra gain can be made by reusing bases; whenever we start a new calculation that differs from the last one in the size of the frustration J_2 , the bases for the various parts for the preceding value of J_2 can be used. This reduces the number of sweeps needed to about three.

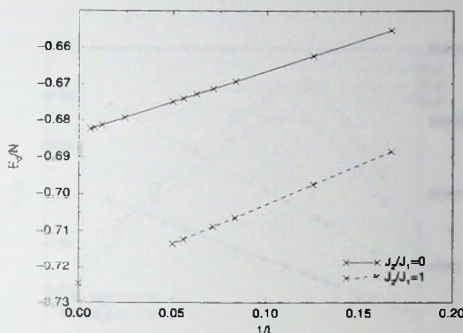


Figure 4-2. The energy density E_0/N as function of the inverse length for width $W = 4$ on the square lattice.

4.5.1 Scaling to $L = \infty$

The width W of the system is fixed and for various lengths L the properties E_0/N , T , J and ρ_s are calculated. Usually we set $L = 2W, 3W, 4W, 5W$. In figures 4-2, 4-3 and 4-4 we have depicted this for square lattices with $W = 4$ and two values for J_2 . Many more lengths L are considered here as it is computationally fairly easy to achieve enough accuracy for system sizes up to $L = 160$. The scaling behaviour of $\mathcal{O}(1/L)$ is clearly confirmed by the graphs. In the figures is the extrapolated values for $1/L = 0$ are also depicted. The resulting energy density E_0/N and stiffness ρ_s of the infinitely long system are collected for various J_2 in figures 4-5 and 4-6. Figures 4-7 and 4-8 contain the equivalent results for the tilted lattice.

4.5.2 Scaling to $W = \infty$

In the final, two-dimensional system, the orientation of the lattice, square or tilted, does no longer matter. The values of all quantities are equal for both orientations at system size $L \times W = \infty \times \infty$. However, the prefactors for the finite-size corrections do not have to be the same. We fit the scaling for both orientations with the same offset, but with different gradients. In figures 4-9, 4-10 and 4-11 this is done for $J_2 = 0$. The resulting extrapolations are also plotted in the figures. In all these figure we have multiplied the width W of the tilted lattices by a factor of 2 so that both the tilted and the square lattices fall within the same range of $1/W^3$ and $1/W$. All data can then easily be plotted in the same graph.

In figures 4-12 and 4-13 we plot the energy density E_0/N and spin stiffness ρ_s for a

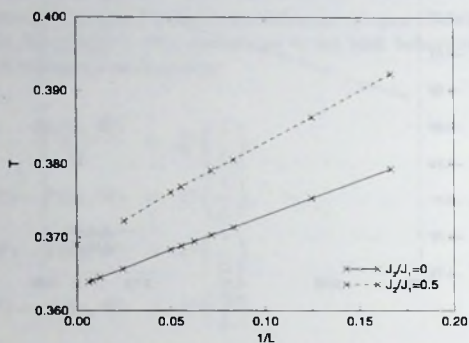


Figure 4-3. The kinetic term T as function of the inverse length for width $W = 4$ on the square lattice.

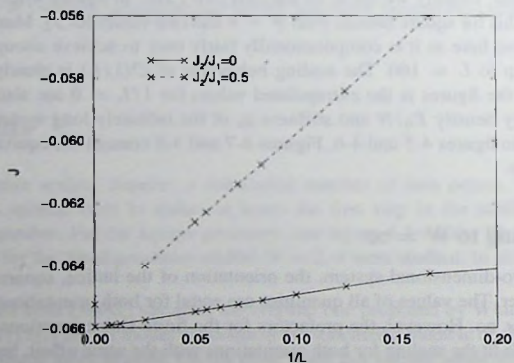


Figure 4-4. The current-current correlation J as function of the inverse length for width $W = 4$ on the square lattice.

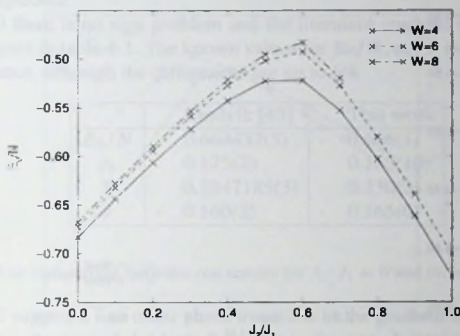


Figure 4.5. The extrapolated energy density E_0/N for widths $W = 4, 6, 8$ on the square lattice. For $W = 8$ ratios $J_2/J_1 \geq 0.8$ were not considered.

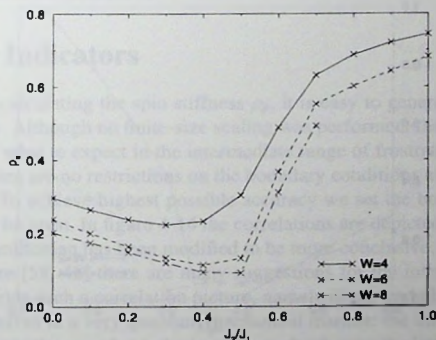


Figure 4.6. The extrapolated spin stiffness ρ_s for widths $W = 4, 6, 8$ on the square lattice.

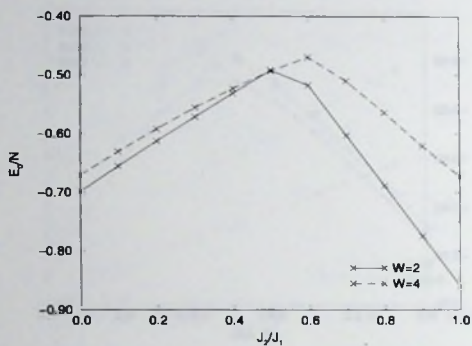


Figure 4-7. The extrapolated energy E_0/N for widths $W = 2, 4$ on the tilted square lattice.

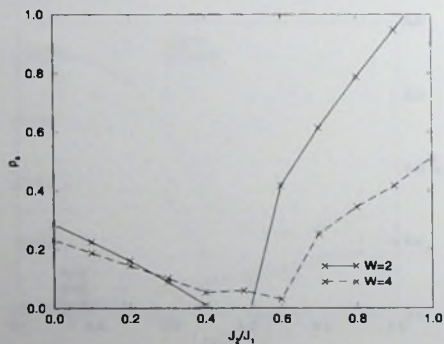


Figure 4-8. The extrapolated spin stiffness ρ_s for widths $W = 2, 4$ on the tilted square lattice.

two-dimensional system. The error bars in these graphs are based on fitting the data-points for (∞, W) to the assumed scaling relations; the errors in the data after the first scaling, $L \rightarrow \infty$ are neglected.

For $J_2 = 0$ there is no sign problem and the literature contains excellent results with which we compare in table 4-1. The known values for E_0/N , ρ_s , T and J do not contradict with our estimates, although the differences are up to 6%.

| | Sandvik [43] | This work |
|----------|---------------|------------|
| E_0/N | - 0.669437(5) | - 0.666(1) |
| ρ_s | 0.175(2) | 0.165(10) |
| T | 0.3347185(3) | 0.330(2) |
| J | - 0.160(2) | - 0.165(6) |

Table 4-1: The comparison between our results for $J_2/J_1 = 0$ and those by Sandvik [43].

Figure 4-12 suggest a first order phase transition as the gradient of energy curve seems to change drastically around $J_2/J_1 \approx 0.6$. This is the same behaviour as observed in the SBMF approximation, figure 3-2.

The error bars of the stiffness ρ_s , figure 4-13, increase dramatically while sweeping past $J_2/J_1 = \frac{1}{2}$. The reason for this is that the kinetic term T and the current-current correlations J for the tilted lattices and the square lattices no longer seem to have the same limit in the two-dimensional case. We still enforce this and as a consequence the error bars increase dramatically. Einarsson and Schulz [16] suggest a region $0.4 \lesssim J_2/J_1 \lesssim 0.6$ where the spin stiffness vanishes, $\rho_s = 0$. This is not in contradiction with our results although we also can not confirm it.

4.6 Other Indicators

In the process of calculating the spin stiffness ρ_s , it is easy to generate the spin-spin correlations $(\vec{S}_i \cdot \vec{S}_j)$. Although no finite-size scaling was performed, the correlations already given a clear hint what to expect in the intermediate range of frustration. For these correlation functions there are no restrictions on the boundary conditions as was the case for the spin stiffness ρ_s . To achieve highest possible accuracy we set the boundary conditions in both directions to be open. In figure 4-14 the correlations are depicted for $J_2/J_1 = 0.5$. To be honest, the Hamiltonian has been modified to be more conclusive. Let us explain this.

In the literature [58, 41] there are many suggestions for the intermediate phase. Two of these would yields such a correlation picture, namely dimer and plaquette phases. They distinguish themselves in a very quantum mechanical manner: the dimer phase consists of nearest neighbour singlets nicely stacked next to each other on the lattice and all aligned in the same direction. The ground state in the plaquette phase basically is a direct product of two vertical singlets plus two horizontal singlets on *each* plaquette.

Figure 4-14 could correspond to a superposition of two discrete orientations of the ground state; one oriented in the vertical direction and one in the horizontal direction.

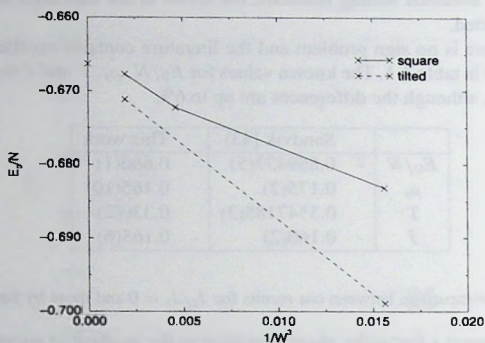


Figure 4-9. The extrapolated energy density E_0/N for square lattices $W = 4, 6, 8$ and tilted lattices $W = 2, 4$. $J_2 = 0$. The widths of the tilted lattices is multiplied by a factor of 2 to get both lines for the square and tilted lattices within the same range. The cross \times on the axis denotes the extrapolated value.

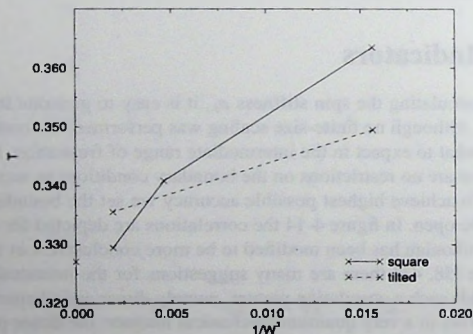


Figure 4-10. The kinetic term T extrapolated. $J_2 = 0$. The cross \times on the axis denotes the extrapolated value.

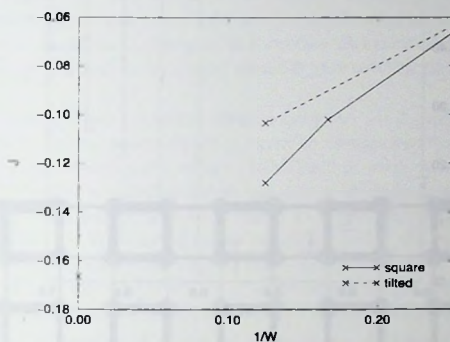


Figure 4-11. The current-current correlation J extrapolated. $J_2 = 0$. The cross \times on the axis denotes the extrapolated value.

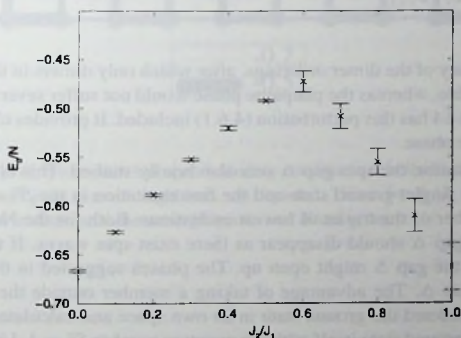


Figure 4-12. The energy density E_0/N for a two-dimensional system. This curve is the collection of extrapolations done as in 4-9. The error bars are based on fitting the data to the scaling relations.

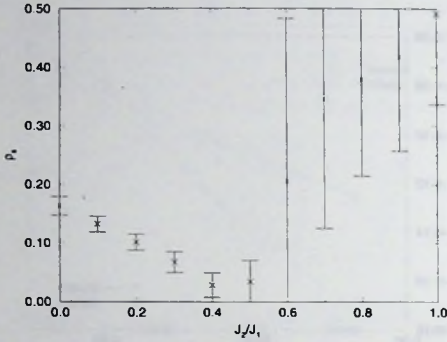


Figure 4-13. The spin stiffness ρ_s of a two-dimensional system. Every point is the sum of the kinetic term T and the current-current correlation J obtained by extrapolation as in 4-10 and 4-11.

Inserting a small perturbation in the Hamiltonian,

$$\delta\mathcal{H} = \frac{J_1}{10} \sum_i \tilde{S}_i \cdot \tilde{S}_{i+\hat{x}}, \quad (4.6.1)$$

will lift the degeneracy of the dimer orderings, after which only dimers in the length direction will remain visible, whereas the plaquette phase would not suffer severely from it. The system depicted in 4-14 has this perturbation (4.6.1) included. It provides clear evidence in favour of a plaquette phase.

As a further indicator, the spin gap Δ was also briefly studied. This is the energy difference between the singlet ground state and the first excitation in the $S^z = 1$ space. This excitation is a member of the triplet of lowest excitations. Both for the Néel and the collinear ordering the gap Δ should disappear as there exist spin waves. If there is a phase between these two, the gap Δ might open up. The phases suggested in the literature actually all imply a gap Δ . The advantage of taking a member outside the $S^z = 0$ space is that it can be considered the ground state in its own space and calculated in exactly the same fashion as the ground state itself with the quantum number $S^z = 1$. Unfortunately the energies of both the ground state and the excitation grow as N whereas the gap remains of order J_1 ; $\Delta \sim J_1$. Only for $W = 4, 6$ we could obtain enough accuracy to scale away the length (an $\mathcal{O}(1/L)$ correction). With only these two points a scaling analysis in the width direction is impossible for the simple reason that no optimal fitting can be done (which needs at least three points).

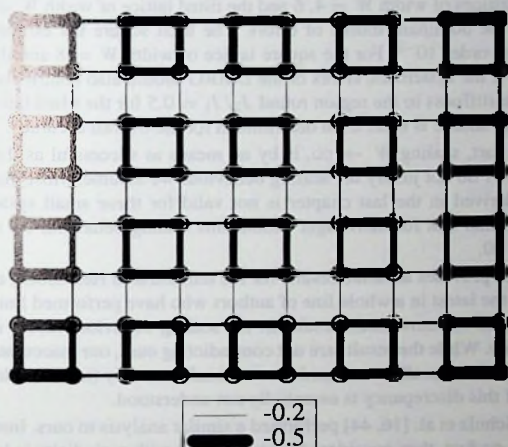


Figure 4-14. For 10×8 system that has open boundary conditions in both directions, the correlations $\langle \tilde{S}_i \cdot \tilde{S}_j \rangle$ where i and j are nearest neighbours, are depicted. This is for $J_2/J_1 = 0.5$. A perturbation (4.6.1) is included to distinguish between plaquette and dimer order.

4.7 Discussion

The scaling analysis of the spin stiffness ρ_s we performed, does not give accurate results. It neither supports nor contradicts the existence of an intermediate phase. The two successive steps of the scaling analysis have very different degree of success and we will discuss them separately;

The first step, scaling $L \rightarrow \infty$, gives reliable values for the properties of an infinitely long cylinder. There are two sources of errors in the properties of this cylinder: corrections to scaling and systematic error in the DMRG due to a insufficient number of states kept. For the square lattices of width $W = 4, 6$ and the tilted lattice of width $W = 2$, the scaling corrections are the dominant source of errors. The least square fits estimate the relative error to be of the order 10^{-3} . For the square lattice of width $W = 8$ and the tilted lattice for width $W = 4$, the systematic errors of the DMRG should also contribute. The peculiar behaviour of the stiffness in the region round $J_2/J_1 = 0.5$ for the tilted lattice, figure 4-3, indicates that this source is there even determinant for the overall accuracy.

The second part, scaling $W \rightarrow \infty$, is by no means as successful as the first. Figures 4-9, 4-10 and 4-11 do not justify the scaling behaviour we assume. Most likely the scaling behaviour we derived in the last chapter is not valid for these small system widths W . There we also found that for Schwinger bosons this scaling behaviour set in at the linear dimension $L = 10$.

The literature provides accurate results for the unfrustrated Heisenberg model, $J_2 = 0$. Sandvik [43] is the latest in a whole line of authors who have performed finite-size scaling on square, periodic systems. Their results fit the scaling behaviour nicely and the results are of high quality. While the results are not contradicting ours, our inaccurate fit is in sharp contrast with theirs. Naturally we consider an unusual geometry (infinitely long cylinders), but the origin of this discrepancy is essentially not understood.

Einarsson, Schulz et al. [16, 44] performed a similar analysis to ours. Instead of scaling the length $L \rightarrow \infty$ first, they considered square lattices with periodicity in both directions. From sizes 4×4 , $2\sqrt{5} \times 2\sqrt{5}$, $4\sqrt{2} \times 4\sqrt{2}$ and 6×6 they inferred the properties of the 2D case. They observe reasonable scaling behaviour in line with the unfrustrated case. That their systems are much smaller than ours, makes the contrast with our findings even more striking.

The stiffness thus does not give a definite answer and we switch our attention to the correlation functions. If there exists an intermediate phase, the correlations in the ground state clearly hint at a plaquette phase. Zhitomirsky and Ueda [58] suggested before that indeed the plaquette phase is favourable to a dimer one. Still, careful study of the dependence of the correlation functions give rise to a few other suspicions: the plaquette correlations arise far sooner than the stiffness becomes negligible. Perhaps a super solid phase exists? Moreover similar behaviour is observed coming from the collinear order, although there dimer (and not plaquette) correlations are appearing. This even makes rooms for two intermediate phases. The abrupt change of the energy in figure 4-12 suggested that between two of these phases a first order phase transition exists. If that is the case, it is most likely that it will occur between a plaquette phase and a dimer phase (possibly both with long range

magnetic order).

In the next chapter we will study the correlations further to get insight in possible intermediate phases.

Monte Carlo

5.1 Introduction

In this chapter we will learn that the DMRG can achieve phenomenological accuracy for reduced density matrix but has systematic deviations once the system gets wider. Section 5.2.1 presents a discussion on how the truncation and postcancellation theory affects the fidelity of the results. The changes based on the analysis of matrix renormalization is a small accuracy improvement. The use of off-diagonal matrix elements in the physical space together with their corresponding singular values improves the accuracy. If we still want to extract ground state information by using the singular values as measurements in the renormalized space, we can do so.

In this section we introduce it with the Later Truncated Matrix Carlo (LTMC), GPMC, it is based on the idea of projecting on the ground state. Define the operator $G = 1 - P$ with P as the projector on the ground state. The ground state $|\psi_0\rangle$ can be found starting with a trial $|\psi\rangle$ and letting

$$|\psi\rangle \rightarrow G|\psi\rangle / \sqrt{\langle\psi|G|\psi\rangle} \quad \text{as } G \rightarrow 0, \quad \text{approach} \quad (5.1.1)$$

When G is small enough, it is sufficient that the singular values of G will be determined and by this property, the full Hilbert space is very large (2^L), making it impossible to apply these matrix operations in detail. We want to produce a representation consisting of $2M$ matrix multiplications. With some error ϵ , M can be found from the bound on the error ϵ as $2M \geq 2^L \epsilon$. $2M = 2M_1 + 2M_2$ means we divide the M as $M_1 + M_2$. An iteration is available from $\langle\psi|G|\psi\rangle$ between the individual projections G as the previous equation, can be read as a renormalization process.

$$\langle\psi|G|\psi\rangle = \sum_i \langle\psi|G_i|\psi\rangle \left[\prod_{j=1}^N \langle\psi|G_j|\psi\rangle \right] \quad (5.1.2)$$

A path Truncated Density Matrix method that it only considers in the ground state and if $\langle\psi|G|\psi\rangle \approx 0$ for all successive eigenvalues, only specific paths through phase space can be selected. The general advantage of a Monte Carlo simulation, and the GPMC, is particular in that accurate projections can still be obtained when only a few of these paths M are systematically selected by important singular values [2]. As the system size L is very large ($2^L \gg 1$), even the most extensive LTMC simulation has its dimensional reduction relative few paths. In practice we always generate GPMC paths.

We will apply the LTMC on the Extended Heisenberg Model and two-band systems. Here we use K can differ as used in the construction of two-band systems in the Hubbard as only nearest-neighbor hopping interactions. The construction of the two-band system

5 Combination of DMRG and Fixed-Node Monte Carlo

5.1 Introduction

In chapter 2 and 4 it became clear that the DMRG can achieve phenomenal accuracy for relatively narrow strips, but the accuracy deteriorates once the strips get wider. Section 2.6.1 provided a connection between this behaviour and perturbation theory. Although this relation only yields an upper bound on the number of states needed for a certain accuracy, it is clear that the number of off-diagonal matrix elements in the Hamiltonian together with their sizes determine the accuracy. If we still want to extract ground state information for wider systems, changes or amendments in the method have to be made.

In this chapter we combine it with the Green Function Monte Carlo (GFMC). GFMC is based on the action of projecting out the ground state. Define the operator $\mathcal{G} = 1 - \varepsilon \mathcal{H}$ with $\varepsilon \ll 1$ [1, 25]. The ground state $|\psi_0\rangle$ can be found starting with a state $|\phi\rangle$ and letting it relax,

$$|\psi_0\rangle \sim \mathcal{G}^n |\phi\rangle, \quad n\varepsilon \gg 1, \quad \varepsilon \ll 1. \quad (5.1.1)$$

When ε is small enough, not the largest but the smallest eigenvector will be projected out by this projection. The Hilbert space is very large $\mathcal{O}(2^N)$, making it impossible to apply these matrix operations in detail. We want to perform a representative sampling of these matrix multiplications. With configurations R , built from individual up and down spins $\sigma = \uparrow, \downarrow$, $|R\rangle = |\sigma_1 \dots \sigma_N\rangle$, we can construct paths $\vec{R} = R_0, \dots, R_n$. Insertion of complete basis sets $\sum_R |R\rangle \langle R|$ between the individual projectors \mathcal{G} in the previous equation, can be read as a summation over paths;

$$|\psi_0\rangle \sim \sum_{\vec{R}} |R_n\rangle \left[\prod_{i=1}^n \langle R_i | \mathcal{G} | R_{i-1} \rangle \right] \langle R_0 | \phi \rangle. \quad (5.1.2)$$

A path \vec{R} derives its name from the fact that it only contributes to the ground state $|\psi_0\rangle$ if $\langle R_i | \mathcal{G} | R_{i-1} \rangle \neq 0$ for all successive configurations; only specific paths through phase space can be followed. The general assumption of a Monte Carlo simulation and the GFMC in particular is that accurate properties can still be obtained when only a few of these paths \vec{R} are semi-randomly selected to represent equation (5.1.2). As the Hilbert space is very large, $\mathcal{O}(2^N)$, even the most extensive GFMC simulations can be considered to contain only relative few paths. In practice we always generate 6000 paths.

We will apply the GFMC to the frustrated Heisenberg Hamiltonian. Successive configurations R_{i-1} and R_i can differ at most in the orientation of two, nearby spins as the Hamiltonian only contains local spin-pair interactions. The transition strength $\langle R_i | \mathcal{G} | R_{i-1} \rangle$

is set by the Hamiltonian so that locally a good equilibrium is reached. As a consequence the local correlation functions are of good quality. The GFMC uses the off-diagonal matrix elements of the Hamiltonian in an essential way to systematically probe the Hilbert space. Both these aspects, high quality of local correlation functions and the intrinsic use of off-diagonal matrix elements, touch on weaknesses of the DMRG; first, as mentioned before the off-diagonal matrix elements severely limit the accuracy of the DMRG. Second, the correlation functions are biased through the sequence in which the sites of the lattice are incorporated in the basis. When the sites of a column are added successively to the basis, the correlations between the columns are underestimated.

The GFMC allows for a systematic bias towards specific paths \bar{R} without influencing the expectation values. This is done by means of a guiding wave function $\langle R|\phi_G\rangle$. It becomes a measure of importance for a configuration R and thereby of a path. This guiding state $|\phi_G\rangle$ embodies both the greatest strength of the method and its main weakness: if a large amount of information on the ground state $|\psi_0\rangle$ is incorporated in the guiding state $|\phi_G\rangle$, the results will improve drastically. On the other hand, without a proper guiding wave function no reasonable results can be obtained.

Even more emphasis is put on a good guiding wave function when handling models with frustration or fermions. These are typical cases exhibiting the 'sign-problem'. A good guiding state $|\phi_G\rangle$ can maybe not solve this sign-problem, but it can suppress it to such an extent that it does not influence the extracted ground state properties.

With the strengths and limitations of both methods in mind, it seems a logical solution to combine them; DMRG can make an initial guess $|\phi_0\rangle$ to the ground state $|\psi_0\rangle$. Although this is a systematic approximation, the local correlation functions bear a clear signature of the method. They depend on the mapping from the two-dimensional system to a one-dimensional chain that is necessary to apply the DMRG (site version). The guess $|\phi_0\rangle$ can improve the GFMC in two ways. Most importantly, it can serve as a guiding state, $|\phi_G\rangle = |\phi_0\rangle$, to reduce the variance and suppress the sign-problem. This guiding state is also used to calculate so-called mixed estimators for observables. These mixed estimators also strongly improve with a better guiding state. The other aspect, where the DMRG state can help, is in the initial state, $|\phi\rangle = |\phi_0\rangle$, but no matter what the quality of this starting point is, eventually the ground state will be reached. Especially the quality of the local correlations will increase by this stochastic process. Without a DMRG state $|\phi_0\rangle$, the GFMC would require another guiding state. In practice these are relatively simple and consequently poor approximations to the ground state, that are involved and complex to construct.

In this chapter we make the connection between DMRG and GFMC by using the DMRG ground state as a guiding state, $|\phi_G\rangle = |\phi_0\rangle$. First we explain the principles of GFMC. Afterwards the sign-problem is discussed and a possible cure is described: Fixed-Node Monte Carlo (FNMC) and the extension to stochastic reconfiguration. With all that in place we make the connection. In fact the only thing we need to extract from the DMRG state $|\phi_0\rangle$ is its value for specific configurations R , $\langle R|\phi_0\rangle$. An algorithm will be introduced to obtain this value for an arbitrary configuration. Naturally no table with an entry for each possible configuration can be built as it would have a size of $\mathcal{O}(2^N)$ just like the number

of configurations. An extra section is spent on curing a common problem of the GFMC by switching from discrete imaginary time intervals, $1 - \varepsilon\mathcal{H}$, to a continuum, $\exp(-\tau\mathcal{H})$. This makes the method also more elegant. Finally, after all these explanatory and introductory sections, the computations are presented and the results are discussed.

5.2 Green Function Monte Carlo

GFMC has been widely used for at least two decades now [25, 11, 48, 40]. In mathematics it finds an equivalent in the Markov chain [25] and in a broader physical perspective it strongly reminds of diffusion.

The method will be explained along the lines of the frustrated Heisenberg model, where for the moment we simply ignore the sign-problem. Following sections will be dedicated to resolving this complication. The frustrated Heisenberg Hamiltonian is a collection of spin-pair interactions

$$\vec{S}_i \cdot \vec{S}_j = \frac{1}{2} (S_i^- + S_j^- S_j^+ + S_i^z S_j^z).$$

The last term will not alter any of the spins $\sigma_1, \dots, \sigma_N$ in a state $|R\rangle$ when applied to it, the first two terms will allow the exchange of an up- and a down-spin. This limits the number of states $|R'\rangle$ that are connected to $|R\rangle$ strongly; either they are identical or in the case that $\sigma_i \neq \sigma_j$, they have spins i and j exchanged, $\sigma_i' = \sigma_j$ and $\sigma_j' = \sigma_i$. Applying the Hamiltonian to a configuration reminds of diffusion as it allows the up-spins to hop from one site to the other.

As mentioned in the introduction we want to project out the ground state $|\psi_0\rangle$ starting from a —not yet identified— $|\phi\rangle$ by successive applications of $\mathcal{G} = 1 - \varepsilon\mathcal{H}$, equation (5.1.1). The wave function $\langle R|\psi_0\rangle$ cannot be obtained completely because of the size of the Hilbert space. For most physical systems it is even arguable whether that is desirable. The physical properties are most important and GFMC focuses on the determination of these.

There are two categories of observables \mathcal{X} , conserved ones ($[\mathcal{X}, \mathcal{H}] = 0$) and non-conserved ones ($[\mathcal{X}, \mathcal{H}] \neq 0$). The conserved observables \mathcal{X} including the Hamiltonian itself, can be measured in a fairly simple manner. The guiding state $|\phi_G\rangle$ will be used to construct a mixed estimate with exactly the same expectation value as the required measurement.

$$\langle \mathcal{X} \rangle_{\text{mixed}} = \frac{\langle \phi_G | \mathcal{X} \mathcal{G}^n | \phi \rangle}{\langle \phi_G | \mathcal{G}^n | \phi \rangle} = \frac{\langle \phi_G | \mathcal{G}^{n/2} \mathcal{X} \mathcal{G}^{n/2} | \phi \rangle}{\langle \phi_G | \mathcal{G}^n | \phi \rangle} = \langle \psi_0 | \mathcal{X} | \psi_0 \rangle. \quad (5.2.1)$$

It is essential that the observable \mathcal{X} commutes with the Hamiltonian \mathcal{H} as after the commutations we use $|\psi_0\rangle \sim \mathcal{G}^{n/2} |\phi_G\rangle \sim \mathcal{G}^{n/2} |\phi\rangle$ for $N \gg 1$.

The previous relation, (5.2.1), does not hold if the observable \mathcal{X} is not conserved, $[\mathcal{X}, \mathcal{H}] \neq 0$. We will show how the mixed estimate differs from the required one, and

by a simple extension reduce this difference. The guiding state can always be considered to contain a component along the ground state and a component orthogonal to it,

$$|\phi_G\rangle = |\psi_0\rangle + \delta|\psi_1\rangle, \quad \langle\psi_0|\psi_0\rangle = \langle\psi_1|\psi_1\rangle = 1, \quad \langle\psi_1|\psi_0\rangle = 0.$$

A good guiding state should have a small perpendicular component, $\delta \ll 1$. When the commutations in (5.2.1) are not allowed, the mixed estimate reads

$$\langle\mathcal{X}\rangle_{\text{mixed}} = \langle\psi_0|\mathcal{X}|\psi_0\rangle + \delta\langle\psi_1|\mathcal{X}|\psi_0\rangle.$$

Relating this to the expectation value of the guiding state, $\langle\phi_G|\mathcal{X}|\phi_G\rangle$, can reduce the corrections to order $\mathcal{O}(\delta^2)$;

$$\begin{aligned} \langle\mathcal{X}\rangle_{\text{improved}} &\equiv 2 \frac{\langle\phi_G|\mathcal{X}\mathcal{G}^n|\phi\rangle}{\langle\phi_G|\mathcal{G}^n|\phi\rangle} - \frac{\langle\phi_G|\mathcal{X}|\phi_G\rangle}{\langle\phi_G|\phi_G\rangle} \\ &= \langle\psi_0|\mathcal{X}|\psi_0\rangle + \delta^2 \left(\langle\psi_0|\mathcal{X}|\psi_0\rangle - \langle\psi_1|\mathcal{X}|\psi_1\rangle \right) + \mathcal{O}(\delta^3) \\ &= \langle\psi_0|\mathcal{X}|\psi_0\rangle + \mathcal{O}(\delta^2). \end{aligned} \quad (5.2.2)$$

To remove this $\mathcal{O}(\delta^2)$ term completely forward walking schemes [8] are necessary, but it is at present unclear whether this can be combined with stochastic reconfiguration as there the weights are frequently changed. For our purposes only mixed and improved mixed estimates, $\langle\mathcal{X}\rangle_{\text{mixed}}$ and $\langle\mathcal{X}\rangle_{\text{improved}}$, are required.

Next is the description of the stochastic nature of the method. In the introduction, paths \bar{R} through phase space were defined, equation (5.1.2). A selection from all possible paths \bar{R} has to be made stochastically. If the path \bar{R} is selected with a probability $P(\bar{R})$ and assigned a weight $M(\bar{R})$, the following expectation value has to hold:

$$\langle\phi_G|\mathcal{X}\mathcal{G}^n|\phi\rangle = \left\langle X(R_n)M(\bar{R}) \right\rangle = \sum_{\bar{R}} X(R_n)M(\bar{R})P(\bar{R}), \quad (5.2.3)$$

for all \mathcal{X} including $\mathcal{X} \equiv 1$. We use here the local expectation value

$$X(R) = \frac{\langle\phi_G|\mathcal{X}|R\rangle}{\langle\phi_G|R\rangle}.$$

The mixed estimate can then be obtained by choosing a large number of paths $\{\bar{R}^\alpha\}$ and calculating

$$\langle\mathcal{X}\rangle_{\text{mixed}} = \frac{\sum_{\alpha} X(R_n^\alpha)M(\bar{R}^\alpha)}{\sum_{\alpha} M(\bar{R}^\alpha)}.$$

In practice the configurations R_i in a path \bar{R} are selected successively. The most important advantage of this is that a specific configuration R_{i-1} connects only to relatively few configurations R_i . Above it is explained that R_i and R_{i-1} can differ at most in the orientation of two spins for $\langle R_i|\mathcal{G}|R_{i-1}\rangle \neq 0$.

The starting configuration, R_0 , is chosen according to probability distribution $P_0(R_0)$. Each configuration R_i afterwards is chosen with probability $P(R_i \leftarrow R_{i-1})$ giving an overall probability of

$$P(\vec{R}) = \prod_{i=1}^n P(R_i \leftarrow R_{i-1}) P_0(R_0),$$

directly in line with the theory of Markov chains. The probabilities $P_0(R)$ and $P(R \leftarrow R')$ have to be normalised without any negative elements;

$$\sum_R P_0(R) = \sum_R P(R \leftarrow R') = 1, \quad P_0(R), P(R \leftarrow R') \geq 0.$$

In a similar fashion the weight is also successively constructed from a starting weight $m_0(R_0)$ and following weight factors $m(R_i)$ combined with 'signs' $s(R_i, R_{i-1})$ [46] and the weight of the path is finally rescaled with a factor $m_{\text{fin}}(R_n)$;

$$M(\vec{R}) = m_0(R_0) \left[\prod_{i=1}^n s(R_i, R_{i-1}) m(R_i) \right] m_{\text{fin}}(R_n).$$

A first approach would be to let the Green function \mathcal{G} decide; choosing starting positions according to their quantum mechanical probability, $|\langle \phi | R \rangle|^2$ ($\langle \phi | \phi \rangle = 1$), and expressing no favour for any specific path afterwards:

$$\begin{aligned} P_0(R_0) &= |\langle \phi | R_0 \rangle|^2, & m_0(R_0) &= \frac{1}{\langle \phi | R_0 \rangle}, \\ P(R_i \leftarrow R_{i-1}) &= \frac{|\langle R_i | \mathcal{G} | R_{i-1} \rangle|}{\sum_R |\langle R | \mathcal{G} | R_{i-1} \rangle|}, & m(R_{i-1}) &= \sum_R |\langle R | \mathcal{G} | R_{i-1} \rangle|, \\ & & s(R_i, R_{i-1}) &= \frac{\langle R_i | \mathcal{G} | R_{i-1} \rangle}{|\langle R_i | \mathcal{G} | R_{i-1} \rangle|}, \\ & & m_{\text{fin}}(R_n) &= \langle \phi | R_n \rangle. \end{aligned} \quad (5.2.4)$$

The equations above also explain why $s(R_i, R_{i-1})$ can be named a sign. These combinations satisfy the condition (5.2.3) as can easily be verified using

$$s(R_i, R_{i-1}) m(R_{i-1}) P(R_i \leftarrow R_{i-1}) = \langle R_i | \mathcal{G} | R_{i-1} \rangle.$$

In the implementation it is only necessary to store the latest configuration R_i and the weight up to that moment. Given the form of the Hamiltonian where up-spins make a random walk through the system, the name walker become suitable for this latest configuration. The walkers are thus combined with the weights to yield the expectation value (5.2.3).

In practice too many irrelevant paths are selected with these unbiased settings. Far better statistics can be achieved using a guiding wave function $\langle R | \phi_G \rangle$. Indeed this is the same wave function as was used to complete the mixed estimates (5.2.1). This wave function helps us to distinguish important configurations from less important ones and thereby

guides the walkers into the relevant parts of the Hilbert space. The easiest way to incorporate the guiding state $|\phi_G\rangle$ in our calculation is by defining an operator $\bar{\mathcal{X}}$ associated to \mathcal{X} by [46]

$$\bar{\mathcal{X}} \equiv \sum_{R,R'} |R\rangle \frac{\langle \phi_G | R \rangle}{1} \langle R | \mathcal{X} | R' \rangle \frac{1}{\langle \phi_G | R' \rangle} \langle R' |.$$

As this is a similarity transformation, the projector $\bar{\mathcal{G}}$ basically remains the same as \mathcal{G} . The set of equations (5.2.4) can still be used for the stochastic process replacing \mathcal{G} by $\bar{\mathcal{G}}$. Only the final and initial weights have to be altered,

$$m_{\text{fin}}(R) = 1 \quad \text{and} \quad m_0(R) = \frac{\langle \phi_G | R \rangle}{\langle \phi | R \rangle}.$$

If we choose the guiding wave function as starting position, $|\phi\rangle = |\phi_G\rangle$, even the initial weight can be dropped, $m_0(R) = 1$. The transition probabilities $P(R_i \leftarrow R_{i-1})$ are now biased towards the most relevant configurations. This only reduces the variance of the expectation values are unaltered.

The algorithm thus far prescribes that after n projections a —mixed— measurement is made, new walkers are created and the projections restarts. In practice it is far more efficient to continue using the same walkers; the existing set is distributed according to $\langle \phi_G | R \rangle \langle R | \psi_0 \rangle$ while the initial set is distributed according to $\langle R | \phi_G \rangle$. Relatively few projections have to be performed to do further measurements that are both independent of the last ones and representative for the ground state.

In this process of successive projections the relative weights of the walkers will spread exponentially. It becomes unwise to continue the path of certain walkers with negligible weight whereas walkers with large weight deserve extra attention. Still one does not want to influence the expectation values.

The technique to perform this task is called branching. Just like the stochastic process that replaced the projecting, the two requirements here are that the expectation values are to remain unaltered and the variance is minimised.

The easiest approach to choose N new walkers out of a set of N old ones is to draw them from a probability distribution

$$P_\alpha = \frac{|M_\alpha|}{\sum_{\alpha'} |M_{\alpha'}|}.$$

In case the walker α is selected, the weight of the new walker is set to

$$\frac{M_\alpha}{|M_\alpha|} \frac{\sum_{\alpha'} |M_{\alpha'}|}{N}. \quad (5.2.5)$$

If one does not want to use correction factors [25], the weights can even be set to unity ($M_\alpha \rightarrow 1$). Despite its elegance the variance of this method is relatively large; it can happen that N times the same walker is selected.

It is possible to reduce the variance of this branching process substantially without changing the expectation value. Here we introduce a small extension of the method introduced by Calandra and Sorella [8] to reduce the variance of the branching process. The essential difference with straight selection of N walkers, is that the scope of the stochastic process is limited as much as possible. It contains two distinct steps.

The first step is not stochastic in nature. Rescale the weights

$$\tilde{M}_\alpha = N \frac{M_\alpha}{\sum_{\alpha'} |M_{\alpha'}|}.$$

This weight \tilde{M}_α is truncated to an integer, $\text{int}(\tilde{M}_\alpha)$. For every α there are $|\text{int}(\tilde{M}_\alpha)|$ new walkers created, each with the configuration of walker α and with the weight defined in (5.2.5). Once this is done for all old walkers, a set of N_0 new walkers is formed. The integer number N_0 is always smaller than N . On simple grounds one expects $N_0 \approx \frac{1}{2}N$.

For the rescaling of the weight, $\hat{M}_\alpha = \tilde{M}_\alpha - \text{int}(\tilde{M}_\alpha)$, the second, stochastic step is performed. We assign a probability P_α to each old walker,

$$P_\alpha = \frac{\hat{M}_\alpha}{\sum_{\alpha'} |\hat{M}_{\alpha'}|}.$$

The probabilities are put next to each other on the interval $[0, 1]$. In each consecutive interval of length $1/(N - N_0)$ ($[0, 1/(N - N_0)]$, $[1/(N - N_0), 2/(N - N_0)]$, ...) one walker is selected by choosing a random number ξ in that interval and establishing to which probability interval P_α this number ξ belongs. In this fashion the remaining $N - N_0$ walkers are selected giving a total of N new walkers.

This stochastic part is similar to the method of selecting N times one walker out of a set of N old walkers which we described before. The essential difference lies in the fact that here one walker is selected *per interval*. The latter method may be less elegant than the original proposal, but it reduces the variance of the branching drastically.

5.3 Fixed-Node Monte Carlo

Unfortunately, the last section does not tell the entire story. The GFMC is severely hampered by the so-called 'sign-problem' in models that contain frustration or fermions. The frustrated Heisenberg model belongs to this class and with it we will exemplify the notion of a sign-problem.

Figure 5-1 depicts the relevant situation. The Hamiltonian contains interactions between $|1\rangle$, $|2\rangle$ and $|3\rangle$. We know that the matrix element connecting $|1\rangle$ with $|2\rangle$ is given by:

$$\langle 2 | \mathcal{G} | 1 \rangle = -\varepsilon \langle 2 | \mathcal{H} | 1 \rangle = -\varepsilon \frac{J_1}{2}.$$

In this move the weight M will pick up a minus sign from $s_{(2),(1)}$. The same holds for the move $|2\rangle \rightarrow |3\rangle$. The move from $|3\rangle$ back to $|1\rangle$ will also induce a minus

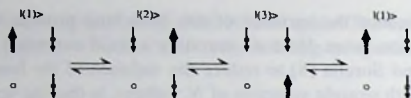


Figure 5-1. The possible exchanges that a up-spin can make with neighbouring down-spins. $|1\rangle \rightleftharpoons |2\rangle$ and $|2\rangle \rightleftharpoons |3\rangle$ result from nearest neighbour interactions and $|1\rangle \rightleftharpoons |3\rangle$ arises through the next nearest neighbour interaction. This figure is minimalistic in that only a fraction of the lattice is drawn and only the exchanging spins are depicted.

sign as $-\varepsilon\langle 1|\mathcal{H}|3\rangle = -\varepsilon\frac{J_2}{2}$. When returned to the original configuration the weight of the walker has thus reversed sign. The sign that a walker picks up following this loop $|1\rangle \rightarrow |2\rangle \rightarrow |3\rangle \rightarrow |1\rangle$ cannot be removed by basis transformations or gauging wave functions.

The foundation of GFMC is that if more and more paths in phase space are incorporated, the overall weight $\sum_{\alpha} M_{\alpha}$ increases and the average $\sum_{\alpha} X_{\alpha} M_{\alpha} / \sum_{\alpha} M_{\alpha}$ improves. Here this line of reasoning does not hold; an extra path can suppress the previous weights. Given the fact that the underlying stochastic process is a Markov chain it is easy to show that the average sign, $\sum_{\alpha} M_{\alpha} / \sum_{\alpha} |M_{\alpha}|$, will decrease exponentially in the number n of projections made. Likewise the signal $\sum_{\alpha} X_{\alpha} M_{\alpha} / \sum_{\alpha} M_{\alpha}$ will become very small with respect to the noise. One can only hope that before the noises overshadows the measurements, the ground state value has already been reached. Under normal conditions, this is rare, but as will be explained in the next sections, one can steer the calculation towards such a situation.

To complete the argument on the sign-problem, two further assessments have to be made. First, in the unfrustrated case, $J_2 = 0$, such a loop as described above, does not exist. A basis rotation, $S = \exp(i2\pi \sum_{x,y} (x+y) S_{x,y}^z)$ removes the signs all together from the projector as

$$\begin{aligned} SG S^{\dagger} &= 1 - SH S^{\dagger} = 1 - \varepsilon J_1 \sum_{(i,j)} S \tilde{S}_i \tilde{S}_j S^{\dagger} \\ &= 1 + \varepsilon J_1 \sum_{i,j} \left[\frac{1}{2} (S_i^{\dagger} S_j^{-} + S_i^{-} S_j^{\dagger}) - S_i^z S_j^z \right]. \end{aligned}$$

From this equation, it is clear that the prefactors of the non-diagonal terms are no longer negative. Once ε is small enough this also holds for the diagonal terms. It is an example of the fairly general approach of a basis transformation to remove the signs from the projector \mathcal{G} . GFMC has indeed helped to establish high quality results for the unfrustrated Heisenberg model [40].

Marshall [29] has proven that after this rotation the exact ground state $|\tilde{\psi}_0\rangle = S|\psi_0\rangle$ of the system is free of signs, $\langle R|\tilde{\psi}_0\rangle \geq 0$. Coming up to our second assessment, this proof can be extended to the region of small J_2 [39]: for $J_2 > 0$ we just argued that a sign-problem existed, thus there can even be a sign-problem when the exact ground state is sign-less!

One of the first successful attempts to overcome this problem originated in the realm of quantum models with continuous degrees of freedom [11]. Later it was extended by van Ant and van Leeuwen [1], van Bemmél et al. [4] and ten Haaf et al. [21] to lattice models. These methods are called Fixed-Node Monte Carlo (FNMC) as both in the continuous version and in the lattice version the Hamiltonian is altered by removing the negative projector matrix elements,

$$\langle R'|\tilde{G}|R\rangle < 0 \text{ or } \langle R'|\tilde{H}|R\rangle > 0 \text{ for } |R'\rangle \neq |R\rangle.$$

The sign of the ~~out coming~~ wave function $\langle R|\mathcal{G}^n|\phi\rangle$ is fixed and the weights M_α are positive definite. In the ~~continuum~~ version this is all there is to it, but in the lattice version the projector \tilde{G} would be altered so strongly that no clear connection to the original system remains. An extra potential has to be introduced to compensate for the restriction of the hops. In the ~~description of~~ the fixed-node method we follow Sorella [46] who made a small extension with ~~respect to~~ the proposal by van Bemmél et al. [4].

Define a ~~fixed-node~~ Hamiltonian \mathcal{H}^{fn} according to the following rules: if $|R'\rangle \neq |R\rangle$, then

$$\begin{aligned} \langle R'|\tilde{\mathcal{H}}^{\text{fn}}|R\rangle &= \langle R'|\tilde{\mathcal{H}}|R\rangle \text{ if } \langle R'|\tilde{\mathcal{H}}|R\rangle \leq 0, \\ &= -\gamma \langle R'|\tilde{\mathcal{H}}|R\rangle \text{ if } \langle R'|\tilde{\mathcal{H}}|R\rangle > 0. \end{aligned}$$

The diagonal element is offset by a sign flip potential,

$$\begin{aligned} \langle R|\tilde{\mathcal{V}}^{\text{sf}}|R\rangle &= \sum_{\langle R'|\tilde{\mathcal{H}}|R\rangle > 0} \langle R'|\tilde{\mathcal{H}}|R\rangle, \\ \langle R|\tilde{\mathcal{H}}^{\text{fn}}|R\rangle &= \langle R|\tilde{\mathcal{H}}|R\rangle + (1 + \gamma)\langle R|\tilde{\mathcal{V}}^{\text{sf}}|R\rangle. \end{aligned}$$

For $\gamma = -1$ the original Hamiltonian is completely recovered including the sign-problem but once $\gamma > 0$ the projector $\tilde{G}^{\text{fn}} = 1 - \varepsilon \tilde{\mathcal{H}}^{\text{fn}}$ contains no signs any longer. Van Bemmél et al. [4] considered the case $\gamma = 0$. Note that the bar over the sign-flip term, $\tilde{\mathcal{V}}^{\text{sf}}$, is only cosmetic, as it only appears in the diagonal terms. On the contrary we cannot remove the bar over \mathcal{H} in the definition of $\tilde{\mathcal{V}}^{\text{sf}}$ as here the non-diagonal matrix elements are considered.

It can be proven that this method is variational [21, 46], i. e.

$$\langle \phi|\mathcal{H}^{\text{fn}}|\phi\rangle - \langle \phi|\mathcal{H}|\phi\rangle = (1 + \gamma)\Delta(\phi, \phi_G) \geq 0 \text{ for all } |\phi\rangle,$$

with $\Delta(\phi, \phi_G)$ a well-defined, positive function independent of γ . The most important property for this difference $\Delta(\phi, \phi_G)$ is that it vanishes at $|\phi\rangle = |\phi_G\rangle$. A direct consequence is that if the ideal guiding wave would be used, $|\phi_G\rangle = |\psi_0\rangle$, the sign-less FNMC would yield the ground state properties exactly (even without the improved mixed estimator).

Within the framework of FNMC we might state that we start with the best possible approximation $|\phi_G\rangle$ that can be made prior to the simulation, and let the (fixed-node) Hamiltonian improve on that.

This approach can be tested on small systems as there we know both the ground state wave function $|\psi_0\rangle$ and its energy $E_0|\psi_0\rangle = \mathcal{H}|\psi_0\rangle$. Experimentally we have found for the frustrated Heisenberg model at $J_2/J_1 = 0.5$ that a reasonable guiding wave with an energy

$$E_G = \frac{\langle \phi_G | \mathcal{H} | \phi_G \rangle}{\langle \phi_G | \phi_G \rangle},$$

will give rise to an outcome of the FNMC simulation with an error ΔE in the energy that is approximately half of the original error, $\Delta E \approx \frac{1}{2}(E_G - E_0)$. More often than not this will not do. Only when a gap in the energy spectrum exist and the FNMC yields an energy below that of the first excitations, it is clear that the state has to resemble the true ground state of the system. In the next section an extension to the FNMC is introduced to get substantially closer to the ground state.

5.4 Stochastic Reconfiguration

Sorella [46] introduced a method that potentially resolves the limitations of the FNMC. He named it Green Function Monte Carlo with Stochastic Reconfiguration (GFMC SR). The new ingredient is the reconfiguration. The stochastic part refers to branching as defined before. It can be interpreted as a sophisticated method to find repeatedly a suitable starting point for a straight GFMC with sign-problem.

It was mentioned before that the sign-problem does not need to be a great obstacle if only a good starting wave function $|\phi\rangle$ could be chosen. The ground state would then be reached before the noise component in the weights becomes dominant. In this section, three possible extensions are described, starting with a simple combination of FNMC and GFMC and finishing with the GFMC SR.

The simplest solution would be to target the ground state of the fixed-node Hamiltonian \mathcal{H}^{fn} first through a FNMC and once that has converged, switch to the projector $\bar{\mathcal{G}}$. Ten Haaf and van Leeuwen [22] have performed this routine, with $\gamma = 0$ for $\bar{\mathcal{G}}^{\text{fn}}$, naming it the power method. A large drawback is that after each measurement the routine has to be restarted; new starting configurations have to be generated, distributed according to the $|\langle \phi_G | R \rangle|^2$.

It is actually fairly straightforward to avoid the restart. A FNMC can be set up with $\gamma > 0$. To each walker two weights are assigned, M_α^{fn} and M_α . The fixed-node weight M_α^{fn} is updated as prescribed before using the projector $\bar{\mathcal{G}}^{\text{fn}}$. The other, normal weight M_α is updated as to reflect the normal projector $\bar{\mathcal{G}}$:

$$m(R) = m^{\text{fn}}(R) \text{ but } s(R', R) = \frac{\langle R' | \bar{\mathcal{G}} | R \rangle}{\langle R' | \bar{\mathcal{G}}^{\text{fn}} | R \rangle} \Leftrightarrow s^{\text{fn}}(R', R) = 1.$$

The weights M_α correspond to the projection with $\bar{\mathcal{G}}$ and will suffer from the sign-problem. After n projections, when the average sign $\sum_\alpha M_\alpha / \sum_\alpha |M_\alpha|$ is not too small, measurements are made and a new, sign-less starting point is taken by assigning

$$M_\alpha^{\text{new}} = M_\alpha^{\text{fn}}. \quad (5.4.1)$$

Still it remains unclear whether the weights M_α have converged enough at the time of measurement and more sophistication is necessary.

There is information in the walkers that both schemes above do not use. In resetting the weights, equation (5.4.1), a lot of information on the ground state is lost. All kinds of correlation functions just obtained in the measurements are not used to improve the starting point. GFMC SR, introduced by Sorella [46], provides a systematic method to incorporate this information in the new starting weights.

If we have a set of observables X^i with expectation values

$$X^i = \frac{\sum_\alpha X^i(R_n^\alpha) M_\alpha}{\sum_\alpha M_\alpha},$$

the new weights M_α^{new} should reflect these,

$$\frac{\sum_\alpha X^i(R_n^\alpha) M_\alpha^{\text{new}}}{\sum_\alpha M_\alpha^{\text{new}}} = \frac{\sum_\alpha X^i(R_n^\alpha) M_\alpha}{\sum_\alpha M_\alpha}. \quad (5.4.2)$$

Moreover the average $\sum_\alpha M_\alpha^{\text{new}} / \sum_\alpha |M_\alpha^{\text{new}}|$, should have increased substantially. The solution to this problem is not unique, but a good handle can be found in the fixed-node weights M_α^{fn} . Start with the expression

$$M_\alpha^{\text{new}} = M_\alpha^{\text{fn}} \left(1 + \sum_i \beta_i (X^i(R_n^\alpha) - X_{\text{fn}}^i) \right),$$

with the average

$$X_{\text{fn}}^i = \frac{\sum_\alpha X^i(R_n^\alpha) M_\alpha^{\text{fn}}}{\sum_\alpha M_\alpha^{\text{fn}}},$$

completely in line with previous definitions. The prefactors β_i are tuned to satisfy equation (5.4.2) [46].

This will yield a starting point with exactly the same properties as observed in the last measurements. In a longer calculation one can even consider adjusting the weight M_α^{new} to reflect the expectation values X^i averaged over several measurements.

With two weights per walker, branching has to be somewhat different than before. The branching is performed on basis of the normal weights M_α and afterwards the fixed-node weight M_α^{fn} is adjusted, $M_\alpha^{\text{fn}} = |M_\alpha|$. Usually the branching is performed just after the reconfiguration.

5.5 A guiding wave function from the DMRG

In the previous sections we have seen that a good guiding wave function is of tremendous importance for all variants of the GFMC (straight GFMC, FNMC and GFMC SR). Historically this has been the bottleneck of the GFMC [20]; before a calculations could be

performed, a large amount of research time had to be dedicated to the design of a guiding wave function that would be both similar to the ground state $|\psi_0\rangle$ and easy to handle in the GFMC. This latter property means that the inner product between a configuration $(\sigma_1, \dots, \sigma_N)$ and the guiding wave function $|\phi_G\rangle$, $\langle \sigma_1 \dots \sigma_N | \phi_G \rangle$, can rapidly be calculated.

A natural candidate for this guiding wave function is the wave function $\langle R | \phi_0 \rangle$ resulting from a DMRG calculation. This will also overcome the bottleneck, as the DMRG is based on a systematic approximation scheme applicable to many different systems. Still, we have seen in the previous chapter, that especially for larger width $W \geq 8$ the state $|\phi_0\rangle$ is quite distinct from the true ground state. The DMRG state $|\phi_0\rangle$ in general systematically underestimates the correlations along the length of the system for relatively wide systems.

It is the distance between the DMRG state $|\phi_0\rangle$ and the true ground state $|\psi_0\rangle$ that the GFMC has to bridge. The obstacles we face implementing the DMRG state $|\phi_0\rangle$ as a guiding wave function $\langle R | \phi_G \rangle = \langle R | \phi_0 \rangle$ are of a technical nature. The remainder of this section will therefore be conceptual straightforward but full of details.

We want to know the value of the wave function $\langle R | \phi_0 \rangle$, but both memory usage and computational effort are an issue. For a single walker the configurations that are of interest are the configuration R of the walker itself and those nearby configurations R' connected by the Hamiltonian, $\langle R' | \mathcal{H} | R \rangle \neq 0$. As these can only differ in the orientation of at most two spins, an efficient algorithm can find these values $\langle R' | \phi_0 \rangle$ relatively fast once the value $\langle R | \phi_0 \rangle$ is known. We will first show how to obtain $\langle R | \phi_0 \rangle$ and afterwards indicate how to use the intermediate results of this last calculation to obtain $\langle R' | \phi_0 \rangle$ rapidly.

A DMRG calculation provides a state $|\phi_0\rangle$ on bases of both the left and the right part of the system. It moreover gives the necessary transformations to construct these sets. Once we have the DMRG state $|\phi_0\rangle$, the representation can be tailored to suit our purposes. In appendix B the technical details are described. The most important modification is to switch to the density matrix basis $|\alpha\rangle_l$ for the left l sites and $|\tilde{\alpha}\rangle_l$ for the right $N - l$ sites. The properties of our representation can be summarised as follows:

- For every partition $1 \leq l < N$ we can represent exactly the same state $|\phi_0\rangle$ as

$$|\phi_0\rangle = \sum_{\alpha} \sqrt{\lambda_{\alpha}^l} |\alpha\rangle_l |\tilde{\alpha}\rangle_l.$$

This provides us with N tables of each m values for $\sqrt{\lambda_{\alpha}^l}$. It can be seen as an extension of equation (2.2.5). There we have only stated that given a partition l such a representation can be made. Here we add that for all partitions the identical state can be represented in this form.

- All basis transformations $A_{\alpha\sigma\alpha'}^l$ for the left and $B_{\alpha\sigma\alpha'}^l$ for the right part are known,

$$|\alpha\rangle_l = \sum_{\sigma\alpha'} A_{\alpha\sigma\alpha'}^l |\sigma\rangle |\alpha'\rangle_{l-1},$$

$$|\tilde{\alpha}\rangle_l = \sum_{\sigma\alpha'} B_{\alpha\sigma\alpha'}^l |\sigma\rangle |\tilde{\alpha}'\rangle_{l+1}.$$

The state $|\sigma\rangle$ contains the spin on site l or $l+1$ respectively. This will yield N matrices A and B of size $2m^2$ each. The estimate of the size is clearly too large as we neglect the fact the both A and B is very sparse.

The wave function $\langle R|\phi_0\rangle$ can now be evaluate at the configuration $\langle\sigma_1 \dots \sigma_N|\phi_0\rangle$ by induction. A reduction to inner products $\langle\sigma_1 \dots \sigma_l|\alpha\rangle_l$ and $\langle\sigma_{l+1} \dots \sigma_N|\bar{\alpha}\rangle_l$ is made via

$$\langle\sigma_1 \dots \sigma_N|\phi_0\rangle = \sum_{\alpha} \sqrt{\lambda_{\alpha}} \langle\sigma_1 \dots \sigma_l|\alpha\rangle_l \langle\sigma_{l+1} \dots \sigma_N|\bar{\alpha}\rangle_l.$$

Each of these two inner products can be derived inductively; e.g.

$$\langle\sigma_1 \dots \sigma_l|\alpha\rangle_l = \sum_{\alpha'} A_{\alpha\sigma_l\alpha'}^l \langle\sigma_1 \dots \sigma_{l-1}|\alpha'\rangle_{l-1}. \quad (5.5.1)$$

To optimise the algorithm for the inner products $\langle R'|\phi_0\rangle$, the intermediate results, $\langle\sigma_1 \dots \sigma_l|\alpha\rangle_l$ and $\langle\sigma_{l+1} \dots \sigma_N|\bar{\alpha}\rangle_l$ for all α and l , are stored in tables. We can use these to readily calculate the inner product of a nearby state $|\sigma'_0 \dots \sigma'_N\rangle = (S_{l_2}^+ S_{l_1}^- + S_{l_2}^- S_{l_1}^+) |\sigma_1 \dots \sigma_N\rangle$ with the state $|\phi_0\rangle$ ($l_2 > l_1$). This new configuration is almost identical to the old one apart from the exchange of the spins on sites l_2 and l_1 ;

$$|\sigma'_0 \dots \sigma'_N\rangle = |\sigma_1 \dots \sigma_{l_2} \dots \sigma_{l_1} \dots \sigma_N\rangle.$$

To calculate the inner product, the system can be split up;

$$\langle\sigma'_0 \dots \sigma'_N|\phi_0\rangle = \sum_{\alpha} \sqrt{\lambda_{\alpha}} \langle\sigma_1 \dots \sigma_{l_2} \dots \sigma_{l_1}|\alpha\rangle_{l_2} \langle\sigma_{l_2+1} \dots \sigma_N|\bar{\alpha}\rangle_{l_2}.$$

The second part of this expression, $\langle\sigma_{l_2+1} \dots \sigma_N|\bar{\alpha}\rangle_{l_2}$, can be found in the tables. The first part can rapidly be built starting from the known, listed inner product $\langle\sigma_1 \dots \sigma_{l_1-1}|\alpha\rangle_{l_1-1}$ and iteratively extending this inner product to location l_2 using (5.5.1).

Further substantial reductions can be made. The most important one is to reuse most of the intermediate results for both $\langle R|\phi_0\rangle$ and $\{\langle R'|\phi_0\rangle\}$ when a walker moves from configuration R to a neighbour R' . Once a walker has propagated far enough for the next measurement or reconfiguration and the next walker will be addressed, all tables are removed. This is unavoidable as the memory usage has to be limited.

A typical system is of size $L \times L = N$ with open boundary conditions in both directions. The calculation of the inner products costs about $2m^2 N$ operations for the partial inner products of the configuration R itself and $N(\sqrt{N}m^2 + 4m^2)/2$ for all others. Here we have again neglected that A and B are very sparse. Still the calculation duration will scale as $N^{3/2}m^2$. If the tables are reused, an extra reduction factor of 4 is achieved.

There is one strong restriction in the wave function of the DMRG; when considering a part of size l the density matrix will select states that lies in specific S^z classes. All other classes, ranging from $S^z = +l/2$ to $S^z = -l/2$ will not appear in the wave function. For the Monte Carlo simulation to relax properly to the ground state, configurations $|R\rangle$, that are not contained in the guiding wave function, have to be assigned a fixed and small value β ;

$$\langle R|\phi_0\rangle = 0 \Rightarrow \langle R|\phi_0\rangle = \beta.$$

5.6 Continuum imaginary time limit

The guiding wave function is not perfect and this can lead to unnecessary large fluctuations in weights of the paths. If a walker visits a configurations $|R\rangle$ with a low 'probability' $|\langle\phi_G|R\rangle| \ll 1$, which neighbours a fairly likely configuration $|R'\rangle$,

$$\langle R'|\mathcal{H}|R\rangle \neq 0 \text{ and } |\langle\phi_G|R'\rangle| \gg |\langle\phi_G|R\rangle|,$$

the local estimate of the energy $E(R)$ gets an excessively large value,

$$E(R) = \frac{\langle\phi_G|\mathcal{H}|R\rangle}{\langle\phi_G|R\rangle}, \quad |E(R)| \gg 1.$$

Only for a perfect guiding wave function we could make the replacement $\langle\phi_G|\mathcal{H}|R\rangle = E(R)\langle\phi_G|R\rangle$ and this problem would disappear. It will have consequences for the weight factor $w(R)$ as the projector \mathcal{G} contains the Hamiltonian \mathcal{H} :

$$m(R) = \frac{\langle\phi_G|\mathcal{G}|R\rangle}{\langle\phi_G|R\rangle} = 1 - \varepsilon E(R).$$

Naturally the walker will almost certainly leave this configuration $|R\rangle$ for $|R'\rangle$ the next projection, but the harm has then already been done. To compensate for this situation, one would like to send $\varepsilon \rightarrow 0$. Without modifications this limit leads to the necessity of infinity many projections n .

Trivedi and Ceperley [48] developed an elegant route out of this trouble. Remember that for $\varepsilon \ll 1$

$$(1 - \varepsilon \mathcal{H})^n = e^{-\varepsilon n \mathcal{H}}. \quad (5.6.1)$$

A continuous time variant can be formulated where only the imaginary time $\tau = \varepsilon n$ is a relevant parameter. Let us describe it for a sign free Hamiltonian, like the fixed-node Hamiltonian \mathcal{H}^{fn} .

If we start in a configuration $|R\rangle$, the probability to remain in it for Δn steps is given by

$$P(R \leftarrow R)^{\Delta n} = \left(\frac{\langle R|\bar{\mathcal{G}}|R\rangle}{\sum_{R'} \langle R'|\bar{\mathcal{G}}|R\rangle} \right)^{\Delta n}.$$

Both the numerator and the denominator of the expression can be simplified using (5.6.1);

$$\begin{aligned} \langle R|\bar{\mathcal{G}}|R\rangle &= \exp(-\varepsilon \langle R|\mathcal{H}|R\rangle), \\ \sum_{R'} \langle R'|\bar{\mathcal{G}}|R\rangle &= 1 - \varepsilon \frac{\langle\phi_G|\mathcal{H}|R\rangle}{\langle\phi_G|R\rangle} = \exp(-\varepsilon E(R)). \end{aligned}$$

Thus the probability is given by

$$P(R \leftarrow R)^{\Delta n} = \exp(-\Delta n \varepsilon (\langle R|\mathcal{H}|R\rangle - E(R))).$$

A random number ξ is chosen to set this time,

$$\Delta\tau \equiv \Delta n\varepsilon = \frac{\ln(\xi)}{E(R) - \langle R|\mathcal{H}|R \rangle}.$$

During this time $\Delta\tau$ the weight is multiplied by a factor

$$m(R)^{\Delta n} = \left(\sum_{R'} \langle R'|\tilde{\mathcal{G}}|R \rangle \right)^{\Delta n} = \exp(-\Delta\tau E(R)).$$

After this time $\Delta\tau$ a jump to another configuration $|R'\rangle \neq |R\rangle$ has to be made according to the transition probabilities

$$P(R \rightarrow R') = \frac{\langle R'|\tilde{\mathcal{G}}|R \rangle}{\sum_{R'' \neq R} \langle R''|\tilde{\mathcal{G}}|R \rangle} = \frac{\langle R'|\mathcal{H}|R \rangle}{\sum_{R'' \neq R} \langle R''|\mathcal{H}|R \rangle}.$$

In this new configuration the walker remains for another time interval. Once the total imaginary time τ has passed, a measurement, reconfiguration or branch can be made.

The GFMSR does not differ much from the above prescription. The fixed-node weight follows it exactly. The normal weight picks up an extra factor during the stay of the walker at a specific configuration,

$$\begin{aligned} \left[s(R, R) m(R) \right]^{\Delta n} &= \frac{\exp(-\Delta\tau \langle R|\mathcal{H}|R \rangle)}{\exp(-\Delta\tau \langle R|\mathcal{H}|R \rangle + (1+\gamma)\nu^{\text{sf}}|R \rangle)} \exp(-\Delta\tau E(R)) \\ &= \exp(\Delta\tau (-E(R) + (1+\gamma)\langle R|\nu^{\text{sf}}|R \rangle)). \end{aligned}$$

In the hops the factor $s(R, R) = \langle R'|\mathcal{H}|R \rangle / \langle R'|\mathcal{H}|R \rangle = 1$ or $-1/\gamma$ is picked up in the weights.

This approach replaces the discrete imaginary time with a continuum and resolves the complication of extreme weight factors $m(R)$.

5.7 Implementation issues

In the previous chapter, the spin stiffness ρ_s was studied. It is possible to obtain the same stiffness in a GFMC simulation by a trivial extension of the method by Pollock and Ceperley [37], but it is as yet not clear whether the same approach can be combined with the GFMC SR. Instead we will focus on the correlation functions for various frustrations J_2 ranging from $J_2 = 0$ to $J_2 = 1.0$ in steps of 0.1.

The geometry of the systems are set to 10×10 with open boundary conditions in both directions since the correlation functions do not require periodic boundary conditions as the spin stiffness did. There are three clear advantages of these open boundary conditions: first, if a dimer or plaquette phase were to appear, the location of the dimers or plaquette will be locked by the boundary conditions; the four corners will always contain such an object and the rest of the system can then easily be filled in. The second advantage is that DMRG obtains the highest accuracy in open systems. Finally, the set of inner products

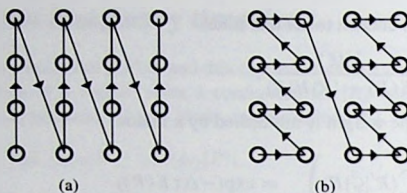


Figure 5-2. The sequence in which the DMRG includes the sites in the left part of the system. (a) represents the ordinary order. (straight) (b) represents a sequence that is more in line with the appearance of plaquettes and all members of a plaquette are added to the basis successively (meandering).

$\langle R' | \phi_0 \rangle$ can be calculated much faster as no neighbouring states exist with one of the first spins exchanged with one of the last spins. For all other neighbours the tables with inner products $\langle \sigma_1 \dots \sigma_l | \alpha \rangle$ can extensively be used.

The DMRG states are built in two distinct sequences as depicted in figure 5-2. Both are based on adding one site at the time to the basis with $m = 75$ basis states. The usual approach, figure 5-2(a), is to add column after column, which we name the straight sequence. For a plaquette order the meandering sequence of figure 5-2(b) is preferable. The individual sites of a plaquette are then added sequentially allowing strong correlations between them. The energy E_{DMRG} is systematically lower for the meandering sequence than for the straight sequence, see table 5-1 (Full explanation of this table will follow in the next section). Therefore we use the meandering sequence to build the guiding wave function. With increasing frustration, dimer correlations appear in the straight sequence and plaquette correlations appear in the meandering sequence.

The mixed estimates incorporated in the reconfiguration are the nearest- and next-nearest-neighbour correlation functions,

$$\langle \tilde{S}_i \cdot \tilde{S}_{i+\hat{x}} \rangle_{\text{mixed}}, \langle \tilde{S}_i \cdot \tilde{S}_{i+\hat{y}} \rangle_{\text{mixed}}, \langle \tilde{S}_i \cdot \tilde{S}_{i+\hat{x}+\hat{y}} \rangle_{\text{mixed}}, \langle \tilde{S}_i \cdot \tilde{S}_{i+\hat{x}-\hat{y}} \rangle_{\text{mixed}}.$$

The guiding states effectively share two symmetries with the system geometry: reflections in the lines $y = 5\frac{1}{2}$ and $x = 5\frac{1}{2}$. These symmetries are included in the mixed estimates reducing their number by approximately a factor of four. No further geometrical symmetries are included. The reflection through the diagonal of the system is excluded as the guiding states do not share this symmetry. Moreover a dimerised state distinguishes itself from a plaquette state by the lack of this symmetry.

After each reconfiguration a branch is performed. We use 6000 walkers en set $\gamma = 0.5$. Table 5-1 lists the imaginary time intervals τ between reconfigurations. The times τ are set to let the average sign $\sum_{\alpha} M_{\alpha} / \sum_{\alpha} |M_{\alpha}|$ decrease from 1 to about 0.8. At the starting of a calculation the average sign tends to drop to a very small value. At the start of the computation the configurations are fairly arbitrary in during the first time intervals τ they will change frequently. As a consequence the average sign at the end of one of the

initial intervals will be almost zero and it will only gradually increase to 0.8 over about 50 measurements. During this 'thermalisation period' none of the calculated mixed estimators can be used for the final expectation values. These are thus removed when the final averages are calculated.

At $J_2 = 0$ there exists a transformation that will remove the sign-problem altogether. Although we do not perform this transformation, still the problem becomes almost signless. The length of the interval τ is set such that successive measurements are independent.

Correction factors introduced by Hetherington [25, 46] are not implemented. A typical simulation with a guiding wave function built with $m = 75$ states, takes about 300 hours on a Intel pentium 300 MHz machine.

5.8 Results

Figures 5-3 and 5-4 together with table 5-1 contain the results. Let us first describe the table.

For all values of J_2 that we compared, the GFMCSR with a guiding state that was built by forward walking through the system, resulted in a lower final ground state energy E_0 . The guiding state itself also has a lower energy than the one obtained from a straight sequence. (For $J_2 = 0.7, 0.8$ this statement does not hold, but there the values are close.) This is a clear indication that these GFMCSR calculations are biased by the guiding state. Future research must determine whether this dependence can be removed.

The dimerisations (x-dim and y-dim) indicate whether the translational symmetry is broken in one of the two directions;

$$\begin{aligned} \text{x-dim} &= \frac{2}{W(L-2)} \sum_{x=1}^{L/2-1} \sum_{y=1}^W \langle \tilde{S}_{2x,y} \cdot \tilde{S}_{2x+1,y} \rangle - \frac{2}{WL} \sum_{x=1}^{L/2} \sum_{y=1}^W \langle \tilde{S}_{2x-1,y} \cdot \tilde{S}_{2x,y} \rangle, \\ \text{y-dim} &= \frac{2}{(W-2)L} \sum_{x=1}^L \sum_{y=1}^{W/2-1} \langle \tilde{S}_{x,2y} \cdot \tilde{S}_{x,2y+1} \rangle - \frac{2}{WL} \sum_{x=1}^L \sum_{y=1}^{W/2} \langle \tilde{S}_{x,2y-1} \cdot \tilde{S}_{x,2y} \rangle. \end{aligned}$$

The expectation values $\langle \tilde{S} \cdot \tilde{S} \rangle$ are approximated by the improved mixed estimator.

The abrupt change of these dimerisation indicators from $J_2 = 0.6$ to $J_2 = 0.7$ already suggest a first order phase transition at that point. This is in agreement with the results of the SBMF theory and the numerical results in the last chapter, figure 4-12.

The figures 5-3 and 5-4 give a more qualitative insight in this behaviour. The average correlation strength between nearest neighbours is negative for each of these systems, $\frac{1}{(L-1)(W-1)} \sum_{(ij)} \langle \tilde{S}_i \cdot \tilde{S}_j \rangle < 0$. Depicted are the individual correlation strengths relative to the average. The solid lines indicate correlations that are more negative and thus stronger than the average. The dotted lines show which correlations are less negative than the average. They can even be positive. In all cases the correlations indicated with the solid lines are also the largest in absolute terms. To approximate these correlation functions the improved estimator is used. Especially in figure 5-3 the ladder structure of the guiding state still persists in the final result. Forward walking schemes can reduce this tendency of the

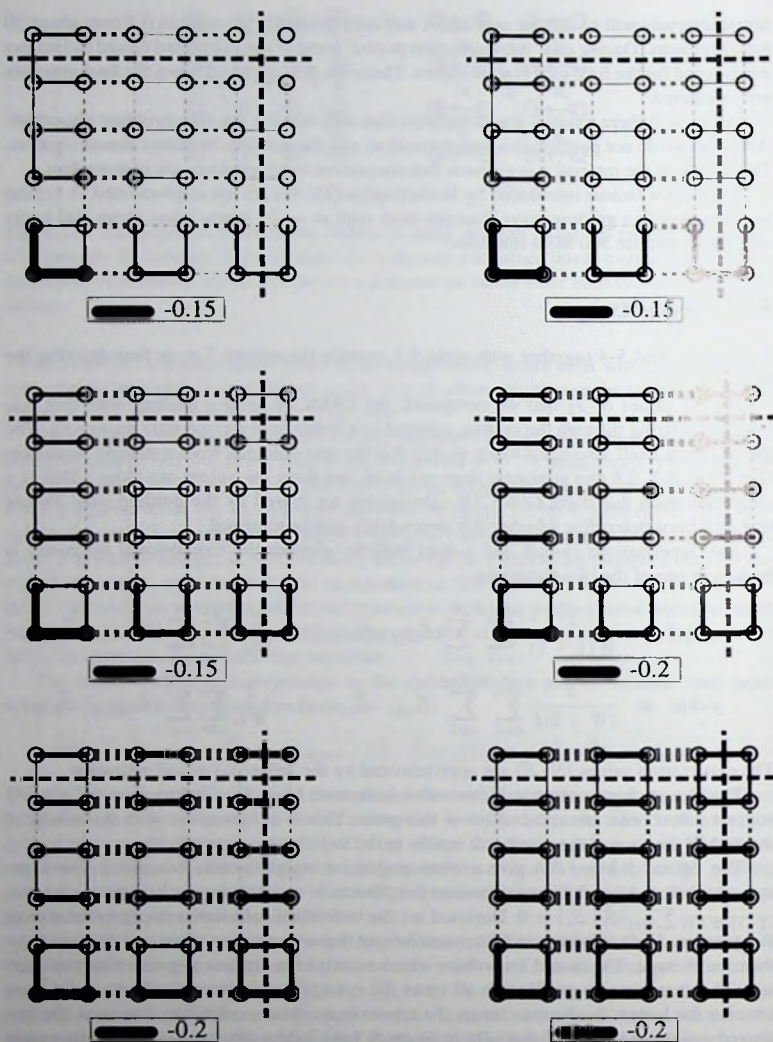


Figure 5-3. The relative correlation strengths on 10×10 lattice. All other nearest neighbour correlations can be obtained by reflection these picture in the two dashed lines. The DMRG guiding state follows the meandering sequence of figure 5-2(b). More explanation is given in the text. Reading from top left to bottom right, the values for J_2 are $J_2 = 0, \dots, 0.5$ in steps of 0.1.

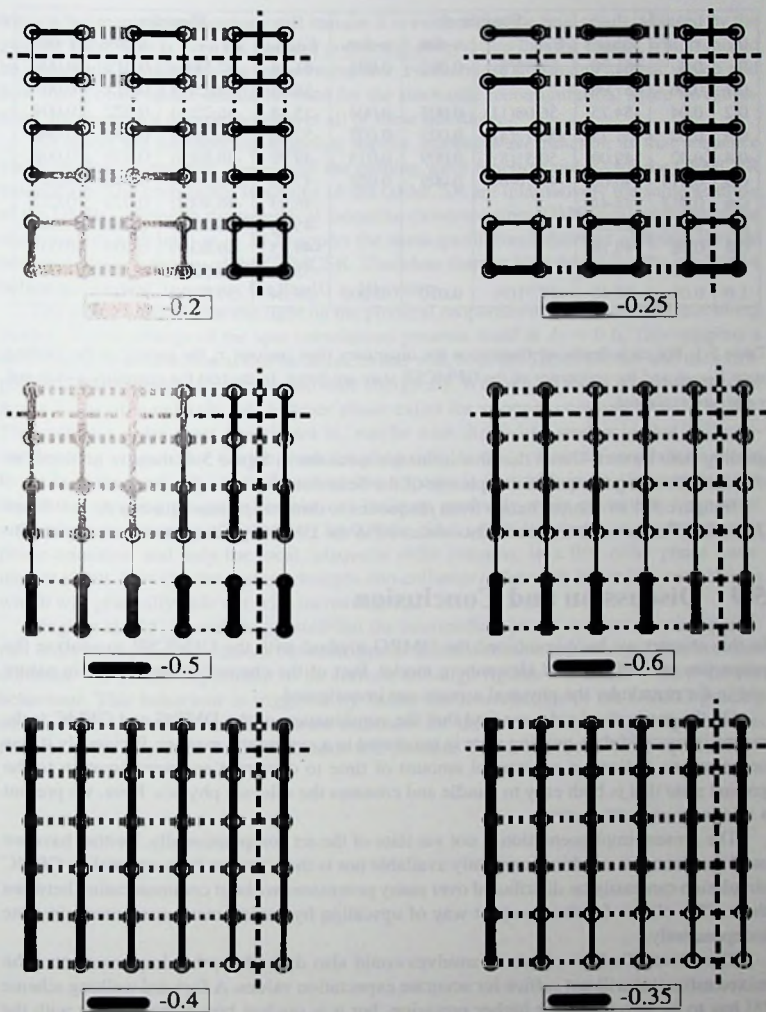


Figure 5-4. The continuation of figure 5-3; the relative correlation strengths on 10×10 lattice. $J_2 = 0.5, \dots, 1.0$ in steps of 0.1.

| J_2 | τ | Straight | | | | Meander | | | |
|-------|--------|-------------------|------------|--------|--------|-------------------|-----------|--------|--------|
| | | E_{DMRG} | E_0 | x-dim. | y-dim. | E_{DMRG} | E_0 | x-dim. | y-dim. |
| 0 | 0.3 | -61.30 | -62.33(8) | 0.002 | 0.001 | -61.84 | -62.54(4) | 0.012 | 0.002 |
| 0.1 | 0.06 | -57.96 | | | | -58.53 | -59.25(2) | 0.017 | 0.003 |
| 0.2 | 0.04 | -54.75 | -56.08(11) | 0.003 | 0.004 | -55.48 | -56.22(4) | 0.022 | 0.004 |
| 0.3 | 0.02 | -51.75 | -53.17(4) | 0.005 | 0.007 | -52.50 | -53.38(3) | 0.034 | 0.006 |
| 0.4 | 0.02 | -49.00 | -50.51(8) | 0.009 | 0.015 | -49.92 | -50.60(5) | 0.035 | 0.004 |
| 0.5 | 0.014 | -46.68 | -47.76(6) | 0.009 | 0.058 | -47.78 | -48.34(4) | 0.063 | 0.021 |
| 0.6 | 0.015 | -45.41 | | | | -46.03 | -46.40(3) | 0.073 | 0.022 |
| 0.7 | 0.015 | -45.67 | | | | -45.60 | -46.00(2) | 0.011 | 0.020 |
| 0.8 | 0.02 | -49.16 | | | | -49.13 | -49.60(9) | 0.009 | 0.001 |
| 0.9 | 0.02 | -53.61 | | | | -53.70 | -54.52(2) | 0.007 | -0.006 |
| 1.0 | 0.02 | -58.46 | -59.71(9) | 0.010 | -0.006 | -58.64 | -59.80(8) | 0.007 | -0.005 |

Table 5-1. For each degree of frustration the imaginary time interval τ , the energy of the guiding state E_{DMRG} and the properties of the GFMCSR state are listed. In the text the quantities x-dim and y-dim are explained.

guiding state further. Given that this influence weakens in figure 5-4, there is no need for this extension to get a qualitative picture of the behaviour.

In figure 5-4 an abrupt change from plaquettes to dimers appears between $J_2 = 0.6$ and $J_2 = 0.7$. The same alteration is also observed in the DMRG guiding state (not depicted).

5.9 Discussion and Conclusion

In this chapter we have combined the DMRG method with the GFMCSR to analyse the properties of the frustrated Heisenberg model. Part of the chapter is methodical in nature and in the remainder the physical aspects are investigated.

On the methodical side, we find that the combination of the DMRG and GFMC techniques is successful. A guiding state is generated in a systematic manner. Previously it was necessary to dedicate a substantial amount of time to construct an approximation to the ground state that is both easy to handle and contains the relevant physics. Here, we present a relatively easy alternative.

The present implementation is not yet state of the art computationally. Neither have we used the strongest machines currently available nor is the software fully optimal. A GFMC simulation can easily be distributed over many processors without communication between them. This allows for the cheapest way of upscaling by having many computers simulate independently.

The Monte Carlo methods themselves could also do with further improvements. The mixed estimator will not suffice for accurate expectation values. A forward walking scheme [8] has to be developed for higher precision, but it is unclear how to combine it with the stochastic reconfiguration that alters the weights frequently. We mention that FNMC does not yield high enough accuracy and an extension is necessary; the GFMCSR is such an ex-

tension but many complications still remain: it is evident that the final result is biased by the guiding state. This is even the case for conserved observables like the energy, which should be accurately sampled by the mixed estimator. Furthermore it remains unclear which and how many observables should be used for the stochastic reconfiguration. More investigations are necessary in order to answer all of these questions.

We select the meandering sequence for the guiding wave function as that sequence yields the lowest energies E_{DMRG} for the guiding wave function and E_0 for the GFMCSR calculation. The correlation functions of the GFMCSR are qualitatively the same as those of the DMRG, although the numerical values lie closer together. DMRG calculations of the same system with upto $m = 512$ support the same qualitative behaviour although they do not reach the low energy of the GFMCSR. Therefore there is little doubt that the qualitative behaviour we find, is correct for the 10×10 system.

The simulations shed some light on the physical properties of the frustrated Heisenberg model. A clear change of the spin correlations presents itself at $J_2 \approx 0.6$. This suggests a first order phase transition at that location, in line with both the SBMF picture and the extrapolated DMRG results for the ground state energy E_0 . With regard to the spin stiffness (see figure 4-13), it is unlikely that a dimer phase exists for stronger coupling then $J_2 \approx 0.6$. The collinear order must already set in, maybe with dimer-like tendencies but still conserving long-range order. On the weak coupling side, $J_2 \ll 1$, plaquette correlations seems to set in quite soon. The overall picture that appears is that with increasing next-nearest neighbour coupling plaquette correlations build up gradually while preserving long-range antiferromagnetic order. At about $J_2 \approx 0.4$ the Néel order disappears in a second order phase transition and only the local, plaquette order remains. In a first order phase transition at about $J_2 \approx 0.6$ the system changes into collinear order with dimer-like correlations which will gradually fade out with increasing J_2 .

Singh et al. [45] recently suggested that the intermediate phase consists of columnar dimer order where the correlations between dimers inside a column are stronger than between columns. We do not expect that to be correct, although figures 5-3 and 5-4 show similar behaviour. This behaviour is triggered by ladder-like correlations in the DMRG guiding states. We expect that a more accurate estimator for these correlations will suppress this feature, as the improved mixed estimator still contains errors of order $\mathcal{O}(\delta^2)$, eq. (5.2.2).

Appendices

A SBMF Approximation for $\mathcal{U}^\dagger(\mathbf{q})\mathcal{H}\mathcal{U}(\mathbf{q})$.

In this appendix the derivation of the Schwinger boson mean-field Hamiltonian for the 'twisted' case, $\mathbf{q} \neq 0$ is performed. In itself this is mostly a repetition of the untwisted case combined with a number of small details. In the process the first and second derivative with respect to \mathbf{q} are also obtained. These are used in section 3.5 to calculate ρ_s .

The Schwinger boson notation is completely equivalent with the spin representation, therefore $\mathcal{H}(\mathbf{q})$ defined in (3.3.4) can be expressed as

$$\mathcal{H}(\mathbf{q}) = \sum_{ij} J_{ij} \left(\mathcal{D}_{ij}^\dagger(\mathbf{q}) \mathcal{D}_{ij}(\mathbf{q}) - \frac{3}{2} \right) - \frac{1}{2} \sum_{AF} J_{ij} \left(\mathcal{B}_{ij}^\dagger(\mathbf{q}) \mathcal{B}_{ij}(\mathbf{q}) - \frac{1}{2} \right).$$

This time we have to distinguish between ferro F and anti ferromagnetic bonds AF explicitly as they are not in general simple nearest and next-nearest-neighbours, where the $\mathcal{D}_{ij}(\mathbf{q})$ and $\mathcal{B}_{ij}(\mathbf{q})$ are given by

$$\begin{aligned} \mathcal{D}_{ij}(\mathbf{q}) &= \mathcal{U}(\mathbf{q}) \mathcal{D}_{ij} \mathcal{U}^\dagger(\mathbf{q}) = a_i a_j^\dagger e^{\frac{i}{2} \mathbf{q} \cdot (\mathbf{r}_i - \mathbf{r}_j)} + b_i b_j^\dagger e^{-\frac{i}{2} \mathbf{q} \cdot (\mathbf{r}_i - \mathbf{r}_j)}, \\ \mathcal{B}_{ij}(\mathbf{q}) &= \mathcal{U}(\mathbf{q}) \mathcal{B}_{ij} \mathcal{U}^\dagger(\mathbf{q}) = a_i b_j e^{\frac{i}{2} \mathbf{q} \cdot (\mathbf{r}_i - \mathbf{r}_j)} + b_i a_j e^{-\frac{i}{2} \mathbf{q} \cdot (\mathbf{r}_i - \mathbf{r}_j)}. \end{aligned} \quad (\text{A.1})$$

The unitary operator $\mathcal{U}(\mathbf{q})$ has been defined in (3.3.3). In section 3.3 a paragraph was dedicated to the correct treatment of the orientation of the ordering. These conditions correspond to the mean-fields here, which have to be taken translationally invariant. Without loss of generality we can take them real;

$$\begin{aligned} \kappa_{ij}(\mathbf{q}) &= \frac{1}{2} \langle \mathcal{D}_{ij}(\mathbf{q}) \rangle, \\ \gamma_{ij}(\mathbf{q}) &= \frac{1}{2} \langle \mathcal{B}_{ij}(\mathbf{q}) \rangle. \end{aligned} \quad (\text{A.2})$$

The mean-field Hamiltonian \mathcal{H}_{MF} now becomes

$$\begin{aligned} \mathcal{H}_{\text{MF}}(\mathbf{q}) &= \sum_F J_{ij} \kappa_{ij}(\mathbf{q}) \left(\mathcal{D}_{ij}^\dagger(\mathbf{q}) + \mathcal{D}_{ij}(\mathbf{q}) - 2\kappa_{ij}(\mathbf{q}) \right) \\ &\quad - \sum_{AF} J_{ij} \gamma_{ij}(\mathbf{q}) \left(\mathcal{B}_{ij}^\dagger(\mathbf{q}) + \mathcal{B}_{ij}(\mathbf{q}) - 2\gamma_{ij}(\mathbf{q}) \right) \\ &\quad + \lambda \sum_i (a_i^\dagger a_i + b_i^\dagger b_i - 1) - \sum_F J_{ij} \frac{3}{4} + \sum_{AF} J_{ij} \frac{1}{4} \end{aligned} \quad (\text{A.3})$$

This Hamiltonian is applicable both to the Néel and the collinear ordering. The spin stiffness has to be derived from the ground state energy of $\mathcal{H}_{\text{MF}}(\mathbf{q})$. This is very similar to the

situation we had in section 3.3; The expression (3.3.6) for ρ_s is recaptured with

$$\begin{aligned}\bar{j} &= \left. \frac{d}{dq} \mathcal{H}_{\text{MF}}(\mathbf{q}) \right|_{\mathbf{q}=0}, \\ \bar{i} &= - \left. \frac{d^2}{dq^2} \mathcal{H}_{\text{MF}}(\mathbf{q}) \right|_{\mathbf{q}=0},\end{aligned}\quad (\text{A.4})$$

and \mathcal{H} replaced by \mathcal{H}_{MF} ; The states $|a\rangle$ appearing in (3.3.7) no longer correspond to the excitations of the full Hamiltonian but to the excitations of the mean-field Hamiltonian \mathcal{H}_{MF} . In order to get explicit expressions for j and i , we will perform some algebra. We define $\tilde{\mathcal{F}}_{ij}$ and $\tilde{\mathcal{C}}_{ij}$ and use (A.1):

$$\begin{aligned}\tilde{\mathcal{F}}_{ij} &= \left. \frac{d}{dq} \mathcal{D}_{ij}(\mathbf{q}) \right|_{\mathbf{q}=0} = \frac{i}{2} (\mathbf{r}_i - \mathbf{r}_j) (a_i a_j^\dagger - b_i b_j^\dagger), \\ \tilde{\mathcal{C}}_{ij} &= \left. \frac{d}{dq} \mathcal{B}_{ij}(\mathbf{q}) \right|_{\mathbf{q}=0} = \frac{i}{2} (\mathbf{r}_i - \mathbf{r}_j) (a_i b_j - b_i a_j).\end{aligned}$$

The derivatives of neither the mean fields $\kappa_{ij}(\mathbf{q})$, $\gamma_{ij}(\mathbf{q})$ nor the Lagrange multiplier will appear in either J or T . It is easy to understand that the dependence on the Lagrange multiplier, λ , can be neglected. This Lagrange multiplier is tuned to make $\sum_i a_i^\dagger a_i + b_i^\dagger b_i - 1 = 0$, so the entire terms drops from the expectation value. The first two, $\kappa_{ij}(\mathbf{q})$ and $\gamma_{ij}(\mathbf{q})$ do not appear in J , as symmetry considerations yield

$$\begin{aligned}\left. \frac{d}{dq} \kappa_{ij}(\mathbf{q}) \right|_{\mathbf{q}=0} &= \frac{1}{2} \left(\left. \frac{d}{dq} \mathcal{D}_{ij}(\mathbf{q}) \right|_{\mathbf{q}=0} \right) = \frac{1}{2} \langle \tilde{\mathcal{F}}_{ij} \rangle = 0, \\ \left. \frac{d}{dq} \gamma_{ij}(\mathbf{q}) \right|_{\mathbf{q}=0} &= \frac{1}{2} \left(\left. \frac{d}{dq} \mathcal{B}_{ij}(\mathbf{q}) \right|_{\mathbf{q}=0} \right) = \frac{1}{2} \langle \tilde{\mathcal{C}}_{ij} \rangle = 0.\end{aligned}$$

Move over in the second derivative these mean field cancel out, e.g.

$$\begin{aligned}\frac{d^2}{dq^2} \left[\kappa_{ij}(\mathbf{q}) \left(\mathcal{D}_{ij}^\dagger(\mathbf{q}) + \mathcal{D}_{ij}(\mathbf{q}) - 2\kappa_{ij}(\mathbf{q}) \right) \right] = \\ \left[\frac{d^2}{dq^2} \kappa_{ij}(\mathbf{q}) \right] \left(\mathcal{D}_{ij}^\dagger(\mathbf{q}) + \mathcal{D}_{ij}(\mathbf{q}) - 4\kappa_{ij}(\mathbf{q}) \right) + \\ \kappa_{ij}(\mathbf{q}) \left(\frac{d^2}{dq^2} \left[\mathcal{D}_{ij}^\dagger(\mathbf{q}) + \mathcal{D}_{ij}(\mathbf{q}) \right] - 2\kappa_{ij}(\mathbf{q}) \right).\end{aligned}$$

The expectation value of the first part is zero by equation (A.2).

Inserting these quantities in (A.4) gives

$$\begin{aligned}\bar{j} &= \sum_F J_{ij} \kappa_{ij} (\tilde{\mathcal{F}}_{ij}^\dagger + \tilde{\mathcal{F}}_{ij}) - \sum_{AF} J_{ij} \gamma_{ij} (\tilde{\mathcal{C}}_{ij}^\dagger + \tilde{\mathcal{C}}_{ij}), \\ \bar{i} &= \frac{1}{2} \sum_F J_{ij} \kappa_{ij} (\mathbf{r}_i - \mathbf{r}_j) (\mathbf{r}_i - \mathbf{r}_j) (\mathcal{D}_{ij}^\dagger + \mathcal{D}_{ij} - 2\kappa_{ij}) \\ &\quad - \frac{1}{2} \sum_{AF} J_{ij} \gamma_{ij} (\mathbf{r}_i - \mathbf{r}_j) (\mathbf{r}_i - \mathbf{r}_j) (\mathcal{B}_{ij}^\dagger + \mathcal{B}_{ij} - 2\gamma_{ij}).\end{aligned}$$

These expressions for the current \bar{j} and kinetic term \bar{i} can be used to calculate ρ_s as is done in section 3.5.

B Transforming the DMRG state to the density matrix basis

In this appendix it will be shown how the same DMRG state $|\phi_0\rangle$ can be represented in a density matrix basis for all possible partitions of the system in a left and a right part. The left part contains the first l sites and the right part the remaining $N - l$ sites.

We define a basis $\{|i\rangle_l\}$ on the left part of the system containing the first l spins and let $\{|j\rangle_l\}$ be a basis on the remaining $N - l$ spins. The state $|\phi_0\rangle$ can be represented by

$$|\phi_0\rangle = \sum \phi_{ij}^{l_0} |i\rangle_{l_0} |j\rangle_{l_0}, \quad (\text{B.1})$$

for a certain l_0 . If we consider the final outcome of a DMRG calculation, the left part will contain all but one site, $l_0 = N - 1$. It is possible to represent the same wave function exactly for all different partitions $1 \leq l < N$. The technique is instructive and we will elaborate on it. Define the transformations $A_{i\sigma i'}^l$ and $B_{j\sigma j'}^l$ by

$$\begin{aligned} |i\rangle_l &= \sum_{\sigma i'} A_{i\sigma i'}^l |\sigma\rangle |i'\rangle_{l-1}, \\ |j\rangle_l &= \sum_{\sigma j'} B_{j\sigma j'}^l |\sigma\rangle |j'\rangle_{l+1}. \end{aligned}$$

With the help of these transformations we will construct the split-up for $l_0 + 1$. All other split-ups are then trivial iterations of the same procedure. Insert the transformation of $|j\rangle_{l_0}$ in equation (B.1);

$$\begin{aligned} |\phi_0\rangle &= \sum_{i,j} \phi_{ij}^{l_0} |i\rangle_{l_0} |j\rangle_{l_0} = \sum_{i,j,\sigma,j'} \phi_{ij}^{l_0} B_{j\sigma j'}^{l_0} |i\rangle_{l_0} |\sigma\rangle |j'\rangle_{l_0+1} \\ &= \sum_{j'} |\beta_{j'}\rangle_{l_0+1} |j'\rangle_{l_0+1}, \end{aligned}$$

where the definition $|\beta_{j'}\rangle = \sum_{i,j,\sigma} \phi_{ij}^{l_0} B_{j\sigma j'}^{l_0} |i\rangle_{l_0} |\sigma\rangle$ is used. Orthonormalisation of $|\beta_{j'}\rangle$ will yield a new basis $\{|i\rangle_{l_0+1}\}$ and a new transformation $A_{i\sigma i'}^{l_0+1}$. Moreover the prefactors of the wave function $\phi_{ij}^{l_0+1}$ can also readily be deduced. It has to be stressed that both the basis $\{|i\rangle_{l_0+1}\}$ and the transformation $A_{i\sigma i'}^{l_0+1}$ follow from this procedure. If we were to have an expression for the transformation $A_{i\sigma i'}^{l_0+1}$ already, it is replaced by this new one. The split-up is changed from l_0 to $l_0 + 1$ and indeed this approach can trivially be extended to yield for all partitions $1 \leq l < N$ the bases $\{|i\rangle_l\}$, $\{|j\rangle_l\}$ and the prefactors ϕ_{ij}^l .

The next ingredient of our recipe is to switch to the density matrix basis. The end of section (2.2) and specifically equation (2.2.5) explain that this can be done by simple basis rotations on the left and on the right basis yielding a representation $\{|\alpha\rangle_l\}$ for the left and $\{|\bar{\alpha}\rangle_l\}$ for the right part. These basis rotations give us furthermore:

- A simple representation of the wave function $|\phi_0\rangle = \sum_{\alpha} \sqrt{\lambda_{\alpha}^l} |\alpha\rangle_l |\bar{\alpha}\rangle_l$.

- Basis transformations $A^I_{\alpha\alpha'}$ and $B^I_{\alpha\alpha'}$.

This is the notation we will use when deriving the value of the wavefunction $\langle R|\phi_0\rangle$.

Bibliography

- [1] G. An, J. M. J. van Leeuwen, Phys. Rev. B **44**, 9410 (1991)
- [2] A. Auerbach, *Interacting Electrons and Quantum Magnetism*, Springer (1994)
- [3] Basic Linear Algebra Subprograms (BLAS), A preview can be found at <http://www.netlib.org/blas>
- [4] H. J. van Bommel, D. F. B. ten Haaf, W. van Saarloos, J. M. J. van Leeuwen, Gerdung An, Phys. Rev. Lett. **72**, 2442 (1994)
- [5] G. D. Gendazzoli, S. Evangelisti, G. Fano, F. Ortolani, L. Ziosi, J. Chem. Phys. **110**, 1177 (1999)
- [6] B. W. J. Blöte, M. Meeuwissen, to be published
- [7] R. J. Bursill, T. Xiang, G. A. Gehring, J. Phys. A **28**, 2109 (1994)
- [8] M. Calandra Buonauro, S. Sorella, Phys. Rev. B **57**, 11446 (1998)
- [9] J. Cardy *Scaling and Renormalization in Statistical Physics*, Cambridge University Press (1996)
- [10] E. Carlon, A. Drzewiński, Phys. Rev. Lett. **79**, 1591 (1997)
- [11] D. M. Ceperley, B. J. Alder Phys. Rev. Lett. **45**, 566 (1980), J. Chem. Phys. **81**, 5833 (1984), Science **231**, 555 (1986)
- [12] D. M. Ceperley, Rev. Mod. Phys. **67**, 279 (1995) equation (3.31)
- [13] B. K. Chakrabarti, A. Dutta, P. Sen. *Quantum Ising Phases and Transitions in Transverse Ising models*, Springer-Verlag (1996)
- [14] M. S. L. du Croo de Jongh, P. J. H. Denteneer, Phys. Rev. B **55**, 2713 (1997)
- [15] M. S. L. du Croo de Jongh, J. M. J. van Leeuwen, Phys. Rev. B **57**, 8494 (1998)
- [16] T. Einarsson, H. J. Schulz, Phys. Rev. B **51**, 6151 (1995)
- [17] A. E. Feiguin, G. J. Gazza, A. E. Trumper, H. A. Ceccatto Phys. Rev. B **52**, 15043 (1995)
- [18] M. E. Fisher, M. N. Barber, D. Jasnow, Phys. Rev. A **188**, 1111 (1973)
- [19] G. A. Gehring, R. J. Bursill, T. Xiang, Acta Phys. Poll. A **91**, 105 (1997) (cond-mat/9608127)

- [20] S. Goedecker, K. Maschke, Phys. Rev. B **44**, 10365 (1991)
- [21] D. F. B. ten Haaf, H. J. M. van Bommel, J. M. J. van Leeuwen, W. van Saarloos, D. M. Ceperley, Phys. Rev. B **51**, 13039 (1995)
- [22] D. F. B. ten Haaf, J. M. J. van Leeuwen, cond-mat/9510042
- [23] B. I. Halperin, P. C. Hohenberg, Phys. Rev. **188** 898 (1969)
- [24] J. L. van Hemmen, Z. Physik B-Cond. Mat. **38**, 271 (1980)
- [25] J. H. Hetherington, Phys. Rev. A **30**, 2713 (1984)
- [26] N. B. Ivanov, P. Ch. Ivanov Phys. Rev. B **46**, 8206 (1992)
- [27] J. M. J. van Leeuwen, M. S. L. du Croo de Jongh, P. J. H. Denton, J. Phys. A:Math. Gen. **29**, 41 (1996)
- [28] S. Liang, H. Pang, Phys. Rev. B **49**, 9214 (1994)
- [29] W. Marshall, Proc. R. Soc. London Ser. A **232**, 48 (1955)
- [30] N. D. Mermin, H. Wagner, Phys. Rev. Lett. **17**, 1133 (1966)
- [31] F. Mila, D. Poilblanc, C. Bruder Phys. Rev. B **43**, 7891 (1991)
- [32] H. Neuberger, T. Ziman, Phys. Rev. B **39**, 2608 (1989)
- [33] R. M. Noack, S. R. White, Phys. Rev. B **47** 9243 (1993)
- [34] R. M. Noack, S. R. White, D. J. Scalapino, Phys. Rev. Lett. **73**, 882 (1994)
- [35] S. Östlund, S. Rommer, Phys. Rev. Lett. **75**, 3537 (1995), S. Rommer, S. Östlund, Phys. Rev. B **49**, 9214 (1994).
- [36] A. van Otterlo, private comm.
- [37] E. L. Pollock, D. M. Ceperley, Phys. Rev. B **36**, 8343 (1987)
- [38] P. Pfeuty, Ann. Phys. **57** 79 (1970); E. Lieb, T. Schultz, D. Mattis, Ann. Phys. **16** 407 (1961)
- [39] J. Richter, N. B. Ivanov, K. Retzlaff, Europhys. Lett. **25**, 545 (1994)
- [40] K. J. Runge, Phys. Rev. B **45**, 7229 (1992) and Phys. Rev. B **45**, 12292 (1992)
- [41] S. Sachdev, *Quantum Phase Transitions*, section 12.3, to be published by Cambridge University Press
- [42] S. Sachdev, Phys. Rev. B **55**, 142 (1997)

- [43] A. W. Sandvik, Phys. Rev. B **56**, 11678 (1998)
- [44] H. J. Schulz, T. A. L. Ziman, D. Poilblanc, J. Phys. I **6**, 675 (1996)
- [45] R. R. P. Singh, Zheng Weihong, C. J. Hamer, J. Oitmaa, cond-mat/9904064
- [46] S. Sorella, Phys. Rev. Lett. **80**, 4558 (1998), S. Sorella, L. Capriotti, cond-mat/9902211
- [47] S. Taniguchi, T. Nishikawa, Y. Yasui, Y. Kobayashi, M. Sato, T. Nishioka, M. Kontani, K. Sano, J. Phys. Soc. Jpn **64**, 2758 (1995)
- [48] N. Trivedi, D. M. Ceperley, Phys. Rev. B **41**, 4552 (1990)
- [49] M. Vekic, S. R. White, Phys. Rev. Lett **71**, 4283 (1993)
- [50] C. Wei, R. Tao, Phys. Rev B **50**, 6840 (1994)
- [51] S. R. White, Phys. Rev. Lett. **69**, 2863 (1992); S. R. White, Phys. Rev. B **48**, 10345 (1993)
- [52] S. R. White, R. M. Noack, Phys. Rev. Lett. **68**, 3487 (1992)
- [53] S. R. White, D. A. Huse, Phys. Rev. Lett. **48**, 3844 (1993)
- [54] S. R. White, Phys. Rev. Lett. **77**, 3633 (1996)
- [55] S. R. White, D. J. Scalapino, Phys. Rev. Lett. **80**, 1272 (1998), Phys. Rev. Lett. **81**, 3227 (1998)
- [56] S. R. White, R. L. Martin, J. Chem. Phys. **110**, 4127 (1999)
- [57] T. Xiang, Phys. Rev. B **53**, 10445 (1996)
- [58] M. E. Zhitomirsky, K. Ueda, Phys. Rev. B **54**, 9107 (1996)

List of Publications

- High-field magnetoresistance oscillations in α -[bis(ethylenedithio)tetrathiafulvalene] $2\text{KHg}(\text{SCN})_4$: The effects of magnetic breakdown, exchange interactions, and Fermi-surface reordering, J. Caulfield, S. J. Blundell, M. S. L. du Croo de Jongh, P. T. J. Hendriks, J. Singleton, M. Doporto, F. L. Pratt, A. House, J. A. A. J. Perenboom, W. Hayes, M. Kurmoo, P. Day, Phys. Rev. B **51**, 8325 (1995)
- Spin stiffness in the Hubbard model, J. M. J. van Leeuwen, M. S. L. du Croo de Jongh, F. F. H. Denteneer, J. Phys. A: Math. Gen. **29**, 41 (1996)
- Spin stiffness in the frustrated Heisenberg antiferromagnet, M. S. L. du Croo de Jongh, F. F. H. Denteneer, Phys. Rev. B **55**, 2713 (1997)
- Critical behavior of the two-dimensional Ising model in a transverse field: A density-matrix renormalisation calculation, M. S. L. du Croo de Jongh, J. M. J. van Leeuwen, Phys. Rev. B **57**, 8494 (1998)
- Towards Understanding Quantum Coherent Dynamics of Molecules: A Simple Scenario for Ultrafast Photoisomerization, D. P. Aalberts, M. S. L. du Croo de Jongh, B. F. Gerke, W. van Saarloos, submitted to Phys. Rev. Lett.
- The Phase diagram of the two-dimensional frustrated Heisenberg model, M. S. L. du Croo de Jongh, J. M. J. van Leeuwen, W. van Saarloos, to be published.

List of Publications

1. The effect of temperature on the rate of reaction between hydrogen peroxide and ferrous sulphate. *Journal of Chemical Education*, 34, 1, 1957, 1-3.
2. The effect of temperature on the rate of reaction between hydrogen peroxide and ferrous sulphate. *Journal of Chemical Education*, 34, 1, 1957, 1-3.
3. The effect of temperature on the rate of reaction between hydrogen peroxide and ferrous sulphate. *Journal of Chemical Education*, 34, 1, 1957, 1-3.
4. The effect of temperature on the rate of reaction between hydrogen peroxide and ferrous sulphate. *Journal of Chemical Education*, 34, 1, 1957, 1-3.
5. The effect of temperature on the rate of reaction between hydrogen peroxide and ferrous sulphate. *Journal of Chemical Education*, 34, 1, 1957, 1-3.
6. The effect of temperature on the rate of reaction between hydrogen peroxide and ferrous sulphate. *Journal of Chemical Education*, 34, 1, 1957, 1-3.
7. The effect of temperature on the rate of reaction between hydrogen peroxide and ferrous sulphate. *Journal of Chemical Education*, 34, 1, 1957, 1-3.
8. The effect of temperature on the rate of reaction between hydrogen peroxide and ferrous sulphate. *Journal of Chemical Education*, 34, 1, 1957, 1-3.
9. The effect of temperature on the rate of reaction between hydrogen peroxide and ferrous sulphate. *Journal of Chemical Education*, 34, 1, 1957, 1-3.
10. The effect of temperature on the rate of reaction between hydrogen peroxide and ferrous sulphate. *Journal of Chemical Education*, 34, 1, 1957, 1-3.

Samenvatting

Dit proefschrift is gebouwd op drie zuilen:

- Numerieke berekeningen,
- Quantum fase overgangen,
- Quantum spin systemen.

Van deze drie is de eerste, numerieke berekeningen, waarschijnlijk het meest eenvoudig te doorgronden. Vaak spreekt men ook van numerieke simulatie om aan te geven dat men de werkelijkheid wil nabootsen. De dagelijkse weervoorspelling is waarschijnlijk het meest bekende voorbeeld van een numerieke simulatie. Het laat ook goed zien, dat deze berekeningen een kunst op zich zijn. Sinds de vorige eeuw weten we aan welke regels luchtdeeltjes voldoen. Deze regels, ook wel Navier-Stokes vergelijkingen genaamd, zijn elegant en eenvoudig, maar de enorme diversiteit aan weersomstandigheden geeft al aan dat het gedrag van de deeltjes hiermee niet doorzichtig is. Pas recentelijk kunnen we redelijke voorspellingen maken. Natuurlijk hebben de steeds snellere computers daaraan bijgedragen, maar computerkracht alleen is niet opgewassen tegen de complexiteit van dit probleem. We zullen de computer flink moeten helpen met ons fysisch inzicht. Zo kunnen we sneeuwval in het weer rond de evenaar uitsluiten. Indien dit soort vereenvoudigingen niet worden doorgevoerd, zal de computer veel te veel tijd kwijt zijn om tot bekende conclusies te komen.

Het is ook verstandig om het doel van numerieke berekeningen te analyseren. Het weerbericht heeft een voorspellend karakter. Er zijn evenwel meer redenen om simulaties uit te voeren. In de natuurkunde wordt vaak gepoogd de werkelijkheid te bevatten in een klein aantal regels en elementen. Aan de hand hiervan stelt men een model op. Nu is er vaak onduidelijkheid over de gelijkenis van zo'n model met de realiteit en een numerieke simulatie van het model kan daar uitkomst brengen. Men kan zich bijvoorbeeld afvragen of de kleur van het aardoppervlak van invloed is op het weer. In de praktijk blijkt dat zo te zijn, aangezien een donker oppervlak veel meer zonlicht absorbeert dan een licht oppervlak. De verwachting is dus al dat een donker oppervlak overdag sneller opwarmt. Is het noodzakelijk om nog meer kleuren te introduceren, of kunnen we rood en groen afdoen als half donker, half licht? Met een numerieke simulatie kan de invloed van die kleuren worden bepaald om vervolgens de nuancering wel of niet op te nemen in het model.

Verder staan numerieke simulaties ons toe allerlei metingen te doen die in de echte wereld niet mogelijk zijn. We kunnen bijvoorbeeld de tijd even vooruitspoelen om naar het weer van morgen te kijken, maar we kunnen ook de tijd eenvoudigweg stilzetten. In dit proefschrift koelen we ons model af naar het absolute nulpunt, $-273,15^\circ$ Celcius. Dit is experimenteel niet mogelijk. Toch kan dit extreme afkoelen enorm helpen om eigenschappen van de natuur te begrijpen.

Samenvattend zijn numerieke berekeningen nuttig vanwege twee redenen: Ten eerste, laten ze allerlei metingen toe die experimenteel niet mogelijk zijn en ten tweede kunnen ze een grote steun zijn bij het vinden van relevante natuurkundige regels. Ze hoeven evenwel niet eenvoudig te zijn. Om een goede berekening te doen, dient men inzicht te hebben in de fysische verschijnselen die men wil analyseren en verder moet men in staat zijn om de vertaalslag naar een computerprogramma te maken.

Ook de tweede zuil, quantum fase overgangen, kent een alledaagse analogie. De fase overgang van water naar ijs door een temperatuursverandering laat zien dat eigenschappen drastisch kunnen veranderen bij maar een kleine temperatuursvariatie. Deze overgang is niet de enige fase overgang in de natuur. Er zijn vele andere fase overgangen bekend. Opvallend is dat ze vaak niets met een temperatuursverandering te maken hebben; er zijn vele voorbeelden van overgangen onder invloed van bijvoorbeeld druk, dichtheid of elektrisch veld. Indien ijs wordt samengeperst, verandert het weer in water. De temperatuur is hierbij niet veranderd. Als tweede voorbeeld bekijken we de schermen van draagbare computers en horloges. Deze bevatten polymeren die normaliter ongeordend en transparant zijn. Zo gauw een elektrisch veld wordt aangezet, richten zij zich en worden ze niet-voorzichtig. Dit soort overgangen blijken vaak op vergelijkbare wijze te kunnen worden beschreven als temperatuurafhankelijke overgangen. Hoe verschillend ze op het eerste gezicht ook mogen zijn; een duidelijk universeel gedrag wordt waargenomen. De overeenkomsten zijn veel omvattender dan alleen de gelijke naam 'fase overgang' doet vermoeden. In dit proefschrift worden twee specifieke gevallen behandeld, die ieder als voorbeeld kunnen dienen voor gehele klassen van quantum fase overgangen.

In de eerste twee hoofdstukken bestuderen we een model waar een extern magneetveld de fase overgang bewerkstelligt. Het is zelf mogelijk te laten zien dat het magneetveld hier precies dezelfde functie heeft als de temperatuur in een gerelateerd model!

De andere fase overgang die in dit proefschrift besproken wordt is in de praktijk moeilijker te bewerkstelligen. Men moet hierbij denken aan de variabele samenstelling van een materiaal. Hier kan niet eenvoudig een vlammetje onder gehouden worden zoals bij ijs om een overgang te veroorzaken. Men moet vele preparaten, ieder met een net even andere samenstelling, de revue laten passeren om de fase overgang te kunnen bestuderen. Slechts één preparaat heeft precies de juiste samenstelling die hoort bij het punt van de fase overgang. Toch blijft de fase overgang ook duidelijk invloed uitoefenen op het gedrag van alle andere preparaten.

De derde zuil, quantum spin systemen, geeft aan dat we fysische modellen bekijken die uit spins zijn samengesteld. De individuele spins doen denken aan magneetjes met een noord- en een zuidpool. Daarnaast voldoen ze aan nog een aantal andere regels die diep in de wereld van de quantummechanica thuis horen. Bijvoorbeeld een spin kan in een toestand verkeren die niet duidelijk georiënteerd is. Pas als men gaat meten zal de spin een unieke oriëntatie uitkiezen. Deze spins zijn in ons geval keurig naast elkaar geplaatst op een vierkant rooster dat lijkt op een barbeque rooster; elk hokje herbergt één spin.

In het proces om fysische systemen zo eenvoudig mogelijk te beschrijven, worden vaak —pseudo— spins geïntroduceerd. De feitelijke deeltjes kunnen bijvoorbeeld elektronen zijn, maar alleen de regels die sterke gelijkenis hebben met de regels voor spins zijn re-

levant. Quantum spin systemen hebben dus vaak een voorbeeldfunctie zoals we al eerder tegenkwamen in de paragrafen over fase overgangen.

Nu de zuilen zijn geplaatst, kunnen we ons richten op het fronton. De eerste twee- en de laatste drie hoofdstukken vormen ieder een duidelijk geheel. Het doel van de eerste twee hoofdstukken is om een nieuwe numerieke methode te doorgronden. Deze methode heet Dichtheids Matrix Renormalisatie Groep (DMRG). In hoofdstuk drie en vier wordt deze methode vervolgens toegepast op het gefrustreerde Heisenberg model. Dit blijkt maar een matig succes op te leveren en in hoofdstuk vijf wordt de DMRG met Green Functie Monte Carlo simulaties (GFMC) gecombineerd om toch de eigenschappen van dit gefrustreerde model te kunnen analyseren. De belangrijkste resultaten van dit proefschrift zijn:

1. Een goed inzicht in de DMRG is verkregen en gerapporteerd.
2. Door de combinatie van DMRG en GFMC kunnen we GFMC makkelijker hanteren voor een brede klasse van problemen.
3. We hebben inzicht gekregen in de fase overgangen van het gefrustreerde Heisenberg model.

De eerste twee hoofdstukken zijn dus methodisch van opzet. De DMRG was al zeer succesvol voor spin ketens en wij willen haar toepassen op spin roosters. Daarvoor hebben we een zeer bekend model uitgekozen wat frequent wordt gebruikt als voorbeeld van een quantum fase overgang. Er is dan ook recentelijk veel numeriek werk aan verricht waaraan wij houvast hebben bij onze studie. Alleen kleine systeempjes met maximaal 32 rijen van 8 spins elk kunnen numeriek worden behandeld. Om toch inzicht te krijgen in grotere systemen wijden we de tweede helft van hoofdstuk één eraan, de specifieke effecten van de kleine afmetingen te bepalen. Die kunnen vervolgens worden verwijderd om de eigenschappen van een oneindig groot rooster te verkrijgen. Dit heet eindige-grootte schaling en wordt al geruime tijd toegepast op dit soort problemen. De resultaten die we op deze wijze verkrijgen, komen overeen met de literatuur.

Hoofdstuk twee bespreekt de DMRG methode en bekijkt wat de mogelijkheden en beperkingen zijn. Het ziet ernaar uit dat de DMRG alleen goede numerieke kwaliteit kan verkrijgen voor smalle roosters (strips). Eindige-grootte schaling blijft dus noodzakelijk om de eigenschappen van grotere roosters te kunnen bepalen. In hoofdstuk vijf zal evenwel een mogelijke uitweg worden gepresenteerd.

Hoofdstuk drie, vier en vijf richten zich op het gefrustreerde Heisenberg model. Ook dit model heeft een voorbeeld functie. Tevens is recentelijk gesuggereerd dat de chemische verbinding CaV_4O_9 er goed door beschreven zou worden. Indien het model geformuleerd wordt zonder de quantummechanische aspecten van spins, is het gedrag volkomen duidelijk. Deze extra quantummechanische regels geven aanleiding tot nieuwe verschijnselen die maar ten dele begrepen zijn. De functie van de temperatuur rond het vriespunt van water wordt hier bekleed door een frustratie maat J_2 . Het systeem is maximaal gefrustreerd rond $J_2 = 0.5$. Voor grotere waarde van J_2 neemt de frustratie weer af omdat de spins zich dan echt anders gaan organiseren. Bij weinig frustratie ($J_2 \approx 0$ en $J_2 \approx 1$) begrijpen we goed wat er gebeurt. In beide gebieden gedraagt het systeem zich eender als de klassieke

variant. Daartussen zit een onduidelijke gebied ($J_2 \approx 0.5$). Waarschijnlijk is daar zelfs een fase die geen klassieke evenknie heeft. Dit geeft aanleiding tot het veronderstellen van twee quantum fase overgangen. Tussen de onbekende fase en de beide zwak gefrustreerde fasen.

Om hier zicht op te verkrijgen gebruiken we in hoofdstuk vier de spin-stijfheid. Dit is een maat voor het gemak waarmee twee spins, ieder op een ander uiteinde van het systeem, in verschillende richtingen georiënteerd kunnen worden. Alle andere spins van het systeem zullen zich aanpassen aan deze beide spins. Indien spins weinig rekening met elkaar houden is het relatief makkelijk deze twee spins anders te oriënteren; de rest reageert toch niet. Het tegenovergestelde is het geval indien de spins wel degelijk rekening houden met elkaar. Deze indicator zou duidelijk andere waarden moeten aannemen voor de drie verschillende fasen. Aangezien wederom alleen kleine systeem numeriek behandeld kunnen worden, is eindige-grootte schaling noodzakelijk om de eigenschappen van veel grotere systeem te bepalen. De resultaten zijn redelijk te noemen ofschoon hieruit niet met zekerheid kan worden geconcludeerd dat deze tussen-fase echt bestaat.

We kunnen ook bekijken hoe sterk de individuele spins met elkaar rekening houden. Dit is gedaan in hoofdstuk vijf voor een systeem met 10 rijen van elk 10 spins. In figuur 4-14 op pagina 85 is mooi te zien dat de spins zich per viertal organiseren. (drie lijnen geven een sterk verband aan). Dit resultaat is niet alleen een duidelijke ondersteuning van het bestaan van de derde fase maar geeft tevens inzicht in de onderliggende ordening.

Hoofdstuk vijf heeft evenwel nog meer te bieden. In dat hoofdstuk introduceren we nog een andere numerieke methode, de Green Funktie Monte Carlo simulatie (GFMC). GFMC omvat systematisch gokwerk om de eigenschappen van een systeem te bepalen. Dit verklaart tevens het tweede gedeelte van de naam. Globaal komt het erop neer dat alle spins een oriëntatie krijgen opgelegd. De onderlinge relaties worden vervolgens vastgelegd en de relevantie van deze situatie wordt bepaald. Nadat vele situaties zijn bekeken, kunnen door combinatie van de relaties met de relevantie de eigenschappen van het systeem worden bepaald. DMRG kan hierbij enorm helpen op twee manieren.

Ten eerste kan DMRG bij voorbaat al inzicht geven in welke situaties het meest relevant zijn. De GFMC bekijkt vervolgens alleen deze. Dit bespaart buitengewoon veel werk en computertijd.

Het tweede aanknopingspunt is zeer quantummechanisch van aard. Het blijkt dat in modellen met concurrerende wisselwerking (frustratie) of met elektronen moeilijk een gemiddelde waarde is te bepalen door het zo geheten teken-probleem. Dit probleem kan verminderd worden door zo veel mogelijk informatie over het systeem in de berekening te verwerken. DMRG heeft erg veel informatie te bieden die in de GFMC methode kan wordt betrokken.

Deze combinatie van DMRG met GFMC kan succesvol worden genoemd. Het laatste woord is er nog niet over gesproken maar er zijn een heel aantal fysische problemen bekend waar zij uitkomst zou kunnen bieden. Deze problemen variëren van supergeleiding tot quantum hall effect.

Curriculum Vitae

Op 27 november 1970 ben ik geboren in Gorssel, een dorp in de buurt van Deventer. In 1989 haalde ik mijn gymnasium β diploma aan het Geert Groote College te Deventer. Daarna heb ik van 1989 tot en met 1995 natuurkunde en wiskunde gestudeerd aan de Universiteit Leiden. Tijdens mijn studententijd heb ik nog enkele jaren geroeid op wedstrijd- en recreatief niveau. In 1993 studeerde ik af in de wiskunde bij dr. J. Hulshof op een scriptie over *partiele differentiaalvergelijkingen*. Daarna verrichtte ik een jaar lang experimenteel onderzoek aan de Universiteit van Oxford. In 1995 studeerde ik af in de theoretische natuurkunde bij mijn latere promotor prof. dr. J. M. J. van Leeuwen. Dit maal omvatte de scriptie een *statistische benadering* voor het Hubbard model.

Na een kort verblijf bij een management adviesbureau in Berlijn begon ik in juni 1995 aan mijn promotie. Het onderzoek zoals beschreven in dit proefschrift concentreerde zich op *numerieke methoden* om fysische eigenschappen van quantum rooster modellen te bepalen. Hiervoor heb ik ook drie maanden prof. dr. S. R. White aan de Universiteit van California in Irvine bezocht. Uiteraard woonde ik diverse cursussen en zomerscholen in het buitenland bij.

Naast mijn onderzoekswerk, heb ik nog het werkcollege 'Electromagnetisme' begeleid. Verder heb ik in de zomer van 1996 drie maanden voor een bank in Londen gewerkt.

Stellingen

behorende bij het proefschrift

'Density Matrix Renormalisation Group Variants for Spin Systems'

1. De Dichtheidsmatrix Renormalisatie Groep kan in de huidige vorm alleen nauwkeurige resultaten leveren voor smalle strips.

Dit proefschrift, hoofdstuk 2.

2. De naam Dichtheidsmatrix Renormalisatie Groep is misleidend omdat deze methode sterk verschilt van de Reële Ruimte Renormalisatie Groep.

Dit proefschrift, hoofdstuk 2.

3. De conclusies die Einarsson en Schulz trekken over het fasediagram van het gefrustreerde Heisenberg model zijn gebaseerd op te kleine systemen en daarmee voorbarig.

Dit proefschrift, hoofdstuk 3, 4,

T. Einarsson, H. J. Schulz,

Phys. Rev. B 51, 6151(1995).

4. De Dichtheidsmatrix Renormalisatie Groep golf functie kan een Green Functie Monte Carlo simulatie begeleiden. Dit lost een oud probleem op.

Dit proefschrift, hoofdstuk 5.

5. De concurrentie tussen de π -orbitale stijfheid en sterische interacties verklaart eenvoudig het strekken van retinal. De stijfheid dwingt 11-cis retinal zijn vorm te behouden. Bij het invangen van een foton verzwakt deze stijfheid en krijgen de sterische interacties het overwicht, waardoor het molecuul razend snel strekt.

D. P. Aalberts, M. S. L. du Croo de Jongh, B. F. Gerke, W. van Saarloos,

Phys. Rev. Lett. ingestuurd.

6. Het grootste obstakel voor een quantumcomputer is de berekening uit te voeren voordat decoherentie intreedt. Deze belemmering is zo groot dat het twijfelachtig is of ooit een bruikbare quantumcomputer zal bestaan.

S. Haroche, J.-M. Raimond,

Physics Today, augustus 1996

7. De overeenkomst tussen licht en elektronen gaat niet veel verder dan dat beide te beschrijven zijn in een golf vergelijking.

College van COMOP onderzoekschool

8. De belangrijkste uitdaging voor de hedendaagse natuurkundigen is de grote hoeveelheid bestaande kennis toegankelijk te maken.
9. Bij handel is technische kennis van het product vaak een nadeel.
10. De prijs van een optie op aandelen wordt bepaald in twee stappen. Eerst wordt met behulp van een mathematisch model een prijs nauwkeurig berekend. Vervolgens wordt deze prijs aangepast aan de stemming in de markt.
11. Door een beter wervingsbeleid voor studenten kan de Leidse faculteit der wiskunde en natuurwetenschappen haar marktaandeel in Nederland en daarbuiten aanzienlijk vergroten.

Lucas du Croo de Jongh
1 september 1999